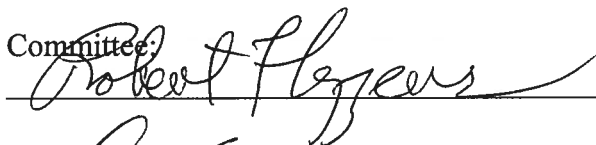


SYNTHESIS, CHARACTERIZATION, AND DISPERSION OF AMPHIPHILIC SELF-  
DECONTAMINATING POLYMER ADDITIVES

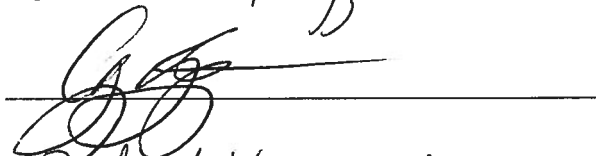
by

Jeffrey G. Lundin  
A Dissertation  
Submitted to the  
Graduate Faculty  
of  
George Mason University  
in Partial Fulfillment of  
The Requirements for the Degree  
of  
Doctor of Philosophy  
Chemistry and Biochemistry

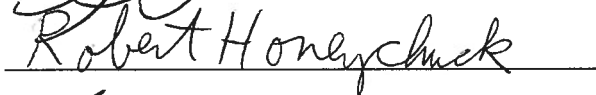
Committee:



Dr. Robert Cozzens, Dissertation Co-Director



Dr. Gerald Roberts Weatherspoon,  
Dissertation Co-Director



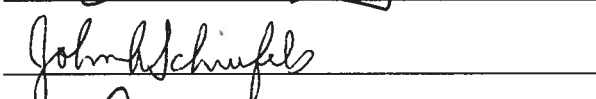
Dr. Robert Honeychuck, Committee Member



Dr. James Wynne, Committee Member



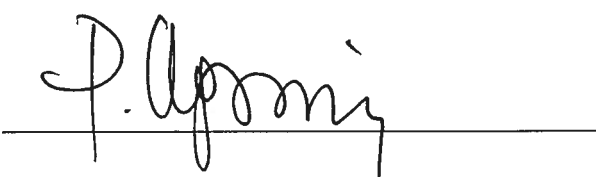
Dr. Brian Rasley, Committee Member



Dr. John Schreifels, Department  
Chairman



Dr. Donna M. Fox, Associate Dean,  
Office of Student Affairs & Special  
Programs, College of Science



Dr. Peggy Agouris, Dean, College  
of Science

Date: 11/21/14

Fall Semester 2014  
George Mason University  
Fairfax, VA

Synthesis, Characterization, and Dispersion of Amphiphilic Self-Decontaminating  
Polymer Additives

A Dissertation submitted in partial fulfillment of the requirements for the degree of  
Doctor of Philosophy at George Mason University

by

Jeffrey George Lundin  
Master of Science  
George Mason University, 2011

Co-Directors:  
Robert F. Cozzens, Professor  
Gerald L.R. Weatherspoon, Associate Professor  
Department of Chemistry and Biochemistry

Fall Semester 2014  
George Mason University  
Fairfax, VA

Copyright © 2014 by Jeffrey G. Lundin  
All Rights Reserved

## **DEDICATION**

This is dedicated to my loving wife, Marcia, for her unending encouragement and support.

## ACKNOWLEDGEMENTS

I would like to acknowledge Dr. Robert Cozzens for his invaluable guidance and contributions of his comprehensive knowledge throughout this project. Dr. Gerald Weatherspoon is greatly appreciated for his impressive attention to detail, helpful constructive criticism, and thought provoking comments, without which this project would most assuredly be incomplete. I would like to thank Dr. Robert Honeychuck for his expertise and insight. The invaluable contributions from the extensive academic knowledge of Dr. Brian Rasley are sincerely appreciated. I owe a significant debt of gratitude to Dr. James Wynne for the opportunity, resources, and immeasurable amount of advice that he has provided along this entire process.

I owe special thanks to Dr. Preston Fulmer for his contributions in the microbial realm and Dr. Pete Coneski for the broad knowledge of polymer chemistry that he shared. The synthetic expertise and analytical acumen of Mr. Spencer Giles were critical in the completion of this work. I would like to acknowledge Dr. James Yesinowski, whose breadth of knowledge of NMR invaluable aided this project. The diligent assistance of Mr. Dillon Gustafson during various experiments is greatly appreciated.

The financial contributions of the Defense Threat Reduction Agency and the Office of Naval Research must be acknowledged as they made this entire work possible. I thank the Office of Naval Research and the Naval Research Laboratory for use of their state-of-the-art facilities. I graciously acknowledge the Naval Research Laboratory Pathways program, which has afforded this unique opportunity to continue my graduate education while accruing valuable laboratory experience in the midst of exceptional scientists.

## TABLE OF CONTENTS

	Page
List of Tables .....	vii
List of Figures .....	viii
List of Abbreviations .....	xii
Abstract .....	xiv
1. Introduction.....	1
1.1. Terminology .....	1
1.2. Historical Use of CWA .....	2
1.3. CWAs of Interest.....	3
1.4. Vesicants .....	4
1.5. Nerve Agents.....	7
1.6. Decontamination Solutions .....	12
1.6.1. CWA Decontamination .....	15
1.7. Polymeric Coatings .....	17
1.7.1. Polyurethanes .....	19
1.7.2. MIL-PRF-85285 .....	21
1.7.3. Functionalized Polymers .....	21
1.7.4. Self-decontaminating Materials.....	24
1.7.5. Recent Research in Novel Reactive Systems .....	26
1.8. Heterogeneous Catalysis .....	27
1.8.1. Fullerene .....	28
1.8.2. Polyoxometalates.....	29
1.9. Surface Segregation.....	30
1.10. Electrospinning.....	31
2. Synthesis and Characterization of QAS encapsulated POMs.....	33
2.1. Overview .....	33
2.2. Prologue .....	33
2.3. Results and Discussion.....	36
2.3.1. Intramolecular ordering of QAS-POMs .....	36
2.3.2. Intermolecular ordering of QAS-POMs .....	48

2.4.	Summary .....	55
2.5.	Experimental Methods .....	56
3.	Distribution of QAS-POMs in Polyurethanes.....	60
3.1.	Overview .....	60
3.2.	Prologue .....	60
3.3.	Results and Discussion.....	63
3.3.1.	Distribution in Hydrothane.....	64
3.3.2.	QAS-POM Distribution in Tecoflex .....	77
3.3.3.	Antimicrobial Activity of Films Containing QAS-POMs.....	89
3.4.	Summary .....	91
3.5.	Experimental Methods .....	93
4.	Amphiphilic C <sub>60</sub> Fullerene – Distribution and Activity.....	98
4.1.	Overview .....	98
4.2.	Prologue .....	99
4.3.	Results and Discussion.....	102
4.3.1.	Additive-Polymer Compatibility .....	102
4.3.2.	Decontamination Challenges.....	112
4.4.	Summary .....	123
4.5.	Experimental Methods .....	124
5.	Incorporation of Amphiphilic Additives into Electrospun fibers .....	135
5.1.	Overview .....	135
5.2.	Prologue .....	135
5.3.	Results and Discussion.....	140
5.3.1.	Effect of QAS on Fiber Morphology and Fiber Diameter .....	140
5.3.2.	Bacterial Challenge .....	150
5.3.3.	Surface Concentration of QAS (XPS).....	153
5.4.	Summary .....	157
5.5.	Experimental Methods .....	158
6.	Conclusions.....	163
	Bibliography .....	166
	Biography.....	179

## LIST OF TABLES

Table	Page
<b>Table 1.1.</b> Physical properties of HD. ....	5
<b>Table 1.2.</b> Toxicities of nerve agents. ....	9
<b>Table 1.3.</b> Physical properties of GA, GB, and GD. ....	10
<b>Table 1.4.</b> Physical properties of VX. ....	12
<b>Table 2.1.</b> Estimated $T_1$ recovery times (ms) of protons for QAS and QAS-POM conjugates. ....	46
<b>Table 2.2.</b> Thermogravimetric data of QAS-POMs. ....	48
<b>Table 3.1.</b> TGA analysis of Tecoflex loaded with increasing concentration of $C_{16}EO_2$ - POM3. ....	81
<b>Table 4.1.</b> TGA data of Tecoflex films. ....	105
<b>Table 4.2.</b> Physical properties of HD compared with simulants. ....	130
<b>Table 5.1.</b> Average diameter of PC and Nylon fibers with increasing QAS concentrations. ....	142
<b>Table 5.2.</b> Selected solution properties of 15 wt% Nylon in formic acid solution containing CTAB. ....	147
<b>Table 5.3.</b> Comparison of total fiber surface area of fibrous mats on $1.88\text{ cm}^2$ coupons to bacterial log kill. ....	153
<b>Table 5.4.</b> Comparison of observed QAS surface concentration with calculated surface concentration assuming even dispersion. Concentration factor was determined by dividing % N observed by % N calculated. ....	154



## LIST OF FIGURES

Figure	Page
<b>Figure 1.1.</b> Structure of the vesicant HD. ....	5
<b>Figure 1.2.</b> Formation of sulfonium ion from HD. ....	6
<b>Figure 1.3.</b> Structures of GA, GB, and GD. ....	9
<b>Figure 1.4.</b> Structures of VX (left) and VR (right). ....	11
<b>Figure 1.5.</b> Chemical structure of EA-2192, a by-product resulting from the hydrolysis of VX. ....	16
<b>Figure 1.6.</b> Comparison of the structure of VX (left) to Demeton- <i>S</i> (center) and Malathion (right). ....	17
<b>Figure 1.7.</b> Formation of a urethane linkage by the reaction of an isocyanate and a primary alcohol. ....	20
<b>Figure 2.1.</b> DRIFT spectra of a) C <sub>12</sub> EO <sub>1</sub> , b) C <sub>12</sub> EO <sub>2</sub> , c) C <sub>16</sub> EO <sub>1</sub> , d) C <sub>16</sub> EO <sub>2</sub> , e) CTAB, and f) POM. ....	37
<b>Figure 2.2.</b> Diffuse reflectance IR of QAS-POM complexes. ....	39
<b>Figure 2.3.</b> <sup>1</sup> H NMR spectra of neat C <sub>16</sub> EO <sub>1</sub> (top) and C <sub>16</sub> EO <sub>2</sub> (bottom) and peak assignments. ....	41
<b>Figure 2.4.</b> <sup>1</sup> H NMR overlay of C <sub>16</sub> EO <sub>1</sub> and C <sub>16</sub> EO <sub>1</sub> -POM3 in the region of 3.0 to 5.0 ppm. ....	43
<b>Figure 2.5.</b> Representative inversion recovery stacked array of <sup>1</sup> H NMR spectra of increasing delay (d7) times for neat C <sub>12</sub> EO <sub>1</sub> . ....	44
<b>Figure 2.6.</b> Representative plot of inversion recovery <sup>1</sup> H NMR signal intensity vs. delay time (d7) in ms for C <sub>16</sub> EO <sub>2</sub> -POM. ....	45
<b>Figure 2.7.</b> Estimated T <sub>1</sub> relaxation time assignments (ms) for protons of QAS and QAS-POMs (T <sub>1</sub> in parentheses). ....	47
<b>Figure 2.8.</b> Heating (top) and cooling (bottom) ramps of QAS and polyoxometalate, uncoordinated. ....	51
<b>Figure 2.9.</b> DSC 2 <sup>nd</sup> heating (top) and 1 <sup>st</sup> cooling (bottom) ramps of QAS-POMs including enthalpy calculations from peak integrations. ....	53
<b>Figure 2.10.</b> General synthetic scheme and lengths of ethoxy ( <i>m</i> ) and alkyl ( <i>n</i> ) moieties of QAS-POM coordinates. ....	57
<b>Figure 3.1.</b> General chemical structures of Hydrothane (top) and Tecoflex (bottom). ....	64
<b>Figure 3.2.</b> SEM micrographs of Hydrothane films loaded at increasing wt% concentration of C <sub>16</sub> EO <sub>1</sub> (left column), POM3 (center), and C <sub>16</sub> EO <sub>1</sub> -POM3. ....	65
<b>Figure 3.3.</b> Average domain diameter vs. wt% loading of C <sub>16</sub> EO <sub>1</sub> POM3 in Hydrothane films. ....	66

<b>Figure 3.4.</b> Loading wt% relative to 3 wt% loading compared to circular areas and spherical volumes calculated from domain diameters. ....	67
<b>Figure 3.5.</b> Histogram of domain diameters on 10 wt% C <sub>16</sub> EO <sub>1</sub> -POM3 Hydrothane films dried at various rates. ....	69
<b>Figure 3.6.</b> SEM micrographs of Hydrothane films loaded with 6 wt% of POM3 coordinated with A) C <sub>10</sub> EO <sub>1</sub> , B) C <sub>12</sub> EO <sub>1</sub> , C) C <sub>12</sub> EO <sub>2</sub> , D) C <sub>16</sub> EO <sub>1</sub> , and E) C <sub>16</sub> EO <sub>2</sub> .....	71
<b>Figure 3.7.</b> Effect of ratio of C <sub>16</sub> EO <sub>2</sub> P and C <sub>16</sub> EO <sub>1</sub> P on domain diameter when incorporated into Hydrothane films at a total loading concentration of 10 wt%. ....	73
<b>Figure 3.8.</b> EDS mapping mode of W signal (purple) overlaid onto SEM micrograph of mixtures of C <sub>16</sub> EO <sub>1</sub> POM:C <sub>16</sub> EO <sub>2</sub> POM. ....	74
<b>Figure 3.9.</b> XPS W 4f signal from Hydrothane films loaded at 6 wt% QAS-POM3 ....	75
<b>Figure 3.10.</b> XPS nitrogen elemental scan of surface (top) and bulk (bottom) of 6 wt% C <sub>16</sub> EO <sub>1</sub> POM Hydrothane film. ....	76
<b>Figure 3.11.</b> Contact angle of Tecoflex films containing QAS-POM3s loaded at 10 wt%. ....	78
<b>Figure 3.12.</b> SEM images of Tecoflex films loaded at 10 wt% QASPOM3. ....	79
<b>Figure 3.13.</b> ATR-IR Spectra of Tecoflex films loaded with C <sub>16</sub> EO <sub>2</sub> -POM3. ....	80
<b>Figure 3.14.</b> 3D Confocal microscopy images of control Tecoflex (left) and 10 wt% C <sub>16</sub> EO <sub>2</sub> -POM Tecoflex. Note the image dimensions in the z-axis are magnified 25X in order to highlight roughness. ....	83
<b>Figure 3.15.</b> Laser confocal microscope images of C <sub>16</sub> EO <sub>2</sub> -POM3 loaded Tecoflex including surface domain dimensions, diameter (D) and height (H).....	84
<b>Figure 3.16.</b> a) Example of confocal microscope image of C <sub>16</sub> EO <sub>2</sub> -POM3 Tecoflex film after adhesive removal and b) proposed dimensions of an average surface domain.....	85
<b>Figure 3.17.</b> Microscope images of Tecoflex surfaces containing C <sub>16</sub> EO <sub>2</sub> -POM after a) fast, b) intermediate, and c) slow solvent evaporation rates. ....	87
<b>Figure 3.18.</b> ATR-IR comparison of the top and bottom of 10 wt% C <sub>16</sub> EO <sub>2</sub> -POM Tecoflex film.....	88
<b>Figure 3.19.</b> XPS nitrogen 1s signal of 10 wt% C <sub>16</sub> EO <sub>2</sub> POM in Tecoflex a) top surface, b) sputtered top bulk, c) bottom surface, and d) sputtered bottom bulk. ..	89
<b>Figure 3.20.</b> Antimicrobial activity of Hydrothane films loaded at increasing concentration of C <sub>16</sub> EO <sub>1</sub> POM3.....	90
<b>Figure 3.21.</b> Antimicrobial activity of Tecoflex films loaded with a range of additives.....	91
<b>Figure 4.1.</b> ATR-IR spectra of Tecoflex films containing C <sub>60</sub> and EO <sub>3</sub> -C <sub>60</sub> additives. ....	103
<b>Figure 4.2.</b> Comparison of DSC thermograms for Tecoflex films containing C <sub>60</sub> and neat C <sub>60</sub> . ....	107
<b>Figure 4.3.</b> XRD patterns of Tecoflex films containing additives. ....	108
<b>Figure 4.4.</b> a) Water contact angle and b) surface roughness (Sq) of Tecoflex films loaded with C <sub>60</sub> and EO <sub>3</sub> -C <sub>60</sub> . ....	110
<b>Figure 4.5.</b> Demeton-S recovered from Tecoflex films after 18 hour residence in dark (a) and daylight (b) conditions. ....	113

<b>Figure 4.6.</b> Detected <i>S</i> -vinyl product (shown as normalized ratio of <i>S</i> -vinyl peak area to tetralin peak area) from Tecoflex films loaded with a) C <sub>60</sub> and b) EO <sub>3</sub> -C <sub>60</sub> over an 18 h Demeton- <i>S</i> challenge. ....	115
<b>Figure 4.7.</b> Demeton- <i>S</i> (1), <i>S</i> -vinyl degradation product (2), CEPS (3), and vinyl phenyl sulfoxide (4). ....	116
<b>Figure 4.8.</b> Hypothesized Lewis acid catalyzed sulfide elimination.....	117
<b>Figure 4.9.</b> Proposed oxidation mechanism of Demeton- <i>S</i> and the formation of elimination product from photogenerated singlet oxygen. ....	118
<b>Figure 4.10.</b> CEPS by-product resulting from residence on Tecoflex films of several additive concentrations following exposure to daylight conditions for 18 hrs. ....	119
<b>Figure 4.11.</b> Concentration of CEPS recovered from samples over 165 hour residence (a) and normalized vinyl phenyl sulfoxide degradation product (b).....	122
<b>Figure 4.12.</b> Potential pathway of sulfide oxidation followed by dehydrohalogenation of CEPS. ....	123
<b>Figure 4.13.</b> Reaction scheme for the synthesis of an amphiphilic fullerene additive. ....	125
<b>Figure 4.14.</b> <sup>1</sup> H NMR spectra of azide reactant (top) and EO <sub>3</sub> -C <sub>60</sub> product (bottom). .	126
<b>Figure 4.15.</b> Structures of HD simulants 2-chloroethyl ethyl sulfide and 2-chloroethyl phenyl sulfide. ....	129
<b>Figure 4.16.</b> Emission spectrum of custom-built photochemical reactor. ....	133
<b>Figure 5.1.</b> Comparison of average surface tension and average fiber diameter of PC/QAS solutions. ....	143
<b>Figure 5.2.</b> SEM micrographs (10,000x mag.) of electrospun PC fibers containing no additive (a), 1 wt% CTAB (b), 5 wt% CTAB (c), 10 wt% CTAB (d), 1 wt% C <sub>16</sub> EO <sub>1</sub> (e), 5 wt% C <sub>16</sub> EO <sub>1</sub> (f), and 10 wt% C <sub>16</sub> EO <sub>1</sub> (g). ....	145
<b>Figure 5.3.</b> SEM micrographs (20,000x mag.) of electrospun Nylon fibers containing no additive (a), 1 wt% CTAB (b), 5 wt% CTAB (c), 10 wt% CTAB (d), 1 wt% C <sub>16</sub> EO <sub>1</sub> (e), 5 wt% C <sub>16</sub> EO <sub>1</sub> (f), and 10 wt% C <sub>16</sub> EO <sub>1</sub> (g). ....	149
<b>Figure 5.4.</b> Average log reduction <i>S. aureus</i> on Nylon and PC electrospun fibers containing quaternary ammonium salts. ....	151
<b>Figure 5.5.</b> XPS N1s region scans demonstrating nitrogen (398 eV) and quaternary ammonium nitrogen (402 eV) in Nylon fibers containing QAS.....	155
<b>Figure 5.6.</b> Comparison of Gram-positive log reduction and surface concentration of QAS in Nylon fibers. ....	157
<b>Figure 5.7.</b> Chemical structures of C <sub>16</sub> EO <sub>1</sub> (left) and CTAB (right). ....	159

## LIST OF ABBREVIATIONS

2-chloroethyl ethyl sulfide .....	2-CEES
2-chloroethyl phenyl sulfide .....	2-CEPS
60 carbon buckminsterfullerene.....	C <sub>60</sub>
acetylcholinesterase .....	AChE
<i>bis</i> (2-chloroethyl) sulfide, distilled.....	HD
centimeter.....	cm
centrifugal force, gravity.....	xg
cetyltrimethylammonium bromide.....	CTAB
chemical Warfare Agent .....	CWA
colony forming units .....	CFU
contact angle .....	θ
critical micelle concentration.....	CMC
decontaminating agent, non-corrosive .....	DANC
degree Celsius .....	°C
demeton- <i>S</i> .....	Dem
differential scanning calorimetry .....	DSC
diffuse reflectance infrared Fourier transform.....	DRIFT
ethylene oxide .....	EO
Gas chromatography/mass spectroscopy .....	GC/MS
glass transition temperature .....	T <sub>g</sub>
gram .....	g
Hertz.....	Hz
hexamethylene diisocyanate .....	HDI
highest occupied molecular orbital .....	HOMO
hydrogen proton .....	<sup>1</sup> H
intersystem crossing.....	ISC
kilogram .....	kg
lethal concentration time to 50 % of population.....	LCt <sub>50</sub>
lethal concentration time.....	LCt
lethal dose to 50 % of population .....	LD <sub>50</sub>
lethal dose .....	LD
liquid-vapor interfacial tension .....	γ <sub>L</sub>
lowest observed lethal dose .....	LD <sub>LO</sub>
Malathion .....	Mal
mass to charge ratio .....	<i>m/z</i>
meter .....	m

microgram	μg
microliter	μL
micrometer	μm
military performance based specification	MIL-PRF
milligram	mg
milliliter	mL
millimole	mmol
mole	mol
Ni containing polyometalate	POM3
nuclear magnetic resonance	NMR
<i>O</i> -Ethyl <i>S</i> -(2-diisopropylaminoethyl) methylphosphonothioate	VX
organophosphorus	OP
paramagnetic relaxation enhancement	PRE
phosphate buffered saline	PBS
polyoxometalate	POM
polyurethane	PU
pound	lb
pounds per square inch	psi
quaternary ammonium salt	QAS
reactive oxygen species	ROS
rotational correlation time	$\tau_c$
Sarin	GB
singlet molecular oxygen	$^1\Delta_g$
singlet-state $C_{60}$	$^1C_{60}$
solid-liquid interfacial tension	$\gamma_{SL}$
solid-vapor interfacial tension	$\gamma_S$
Soman	GD
spin-lattice relaxation	$T_1$
spin-spin relaxation	$T_2$
Tabun	GA
tetrachloroethane	TCE
thermal gravimetric analysis	TGA
triplet molecular oxygen	$^3\Sigma_g^-$
triplet-state $C_{60}$	$^3C_{60}$
ultraviolet	UV
visible	Vis
watt	W
weight	wt.
weight percent	wt%
World War I	WW I
World War II	WW II

## **ABSTRACT**

### **SYNTHESIS, CHARACTERIZATION, AND DISPERSION OF AMPHIPHILIC SELF-DECONTAMINATING POLYMER ADDITIVES**

Jeffrey G. Lundin, Ph.D.

George Mason University, 2014

Dissertation Co-Directors: Dr. Robert F. Cozzens and Dr. Gerald L.R. Weatherspoon

The threat of chemical warfare agent (CWA) release poses risks to exposure from contact with vehicle and building surfaces that are susceptible to remain contaminated for extended duration after a release event. Current decontamination approaches require the application of the caustic and corrosive solutions which, in addition to decomposing the toxic contaminant, also contribute to the degradation of the object being decontaminated and present their own inherent health risks. Often material surfaces are covered in polymeric coatings, paint, that provides a convenient substrate into which novel reactive additives can be incorporated to impart automatic decontamination capability to their surface. A self-decontaminating coating has the capability to automatically facilitate the decomposition of toxic contaminants on its surface, thereby reducing the risk of exposure and the reliance on aggressive decontamination solutions. Reactive molecules  $C_{60}$  and polyoxometalate (POM) have exhibited capability to impart self-decontaminating behavior to a coating surface; however, these additives also impart negative properties

onto the coating such as roughness and reduced physical characteristics that arise from intermolecular incompatibilities between additive and polymer matrix. Herein, amphiphilic modifications of reactive additives were performed to improve the incorporation into polymer coating systems. Further, POM additives exhibiting a range of amphiphilic character were synthesized to investigate the role of additive composition in dispersion in a polymer matrix. The synthetically modified products were thoroughly characterized to elucidate their intramolecular binding. Amphiphilic modification was investigated as it has the potential to cause the additive to automatically orient at the polymer-air interface, or surface segregate. The amphiphilic additives were incorporated into control polymer solutions and their surface and bulk properties were comprehensively analyzed. Amphiphilic modification resulted in the improved incorporation of POM and the surface segregation of C<sub>60</sub> in polyurethane polymers. Upon incorporation of amphiphilic additives into polyurethane coatings, surface reactivity against CWA simulants in simulated environmental conditions confirmed imparted self-decontamination. The mechanism of reaction for the amphiphilic C<sub>60</sub> was determined to be a photocatalytic oxidation upon challenge with chemical warfare agent simulants.

## **1. INTRODUCTION**

Chemical warfare agents (CWAs) are molecules, which have been specifically selected and synthesized for either standalone use or incorporated into weapons as means to incapacitate an enemy during warfare. However, despite their development for use in times of war CWAs have since become major terrorist threats due to the persistence, toxicity, and detectability that the molecules generally exhibit.<sup>1-3</sup> The recent string of revolutions in the Middle East, which has toppled several former militant regimes and left numerous stockpiles open to looting and thievery by extremists, significantly compound the threat.<sup>4</sup> In response to the threats posed by CWAs from both military and rogue groups, research has focused on decontaminating solutions and, more recently, materials capable of automatically decontaminating upon CWA exposure.<sup>5</sup>

### **1.1. Terminology**

Toxicities for most agents are well documented and are represented in several formats. The terms associated with each agent must first be briefly defined to circumvent potential confusion. Dose refers to the quantity of chemical received by the subject. A dose for toxicity research is often administered topically on the skin (dermal), injected directly into the bloodstream (intravenous), injected under the skin (subcutaneous), or swallowed (oral). The lethal dose (LD) which kills 50 % of a given population is abbreviated by LD<sub>50</sub>. Often LD<sub>50</sub> is normalized as a measurement of the mass of



chemical (usually mg) per kilogram of body weight ( $\text{mg}\cdot\text{kg}^{-1}$ ). Lethal dose low ( $\text{LD}_{\text{Lo}}$ ) expresses the minimum quantity by mass of chemical agent per kilogram of body mass which has been observed to be fatal to an individual of a given population. The lethal concentration time (LCt), measured in milligram minutes per cubic meter ( $\text{mg}\cdot\text{min}\cdot\text{m}^{-3}$ ), is frequently used to measure the toxicity of exposure to the vapor or aerosol forms of a substance. This unit is purely the product of concentration ( $\text{mg}\cdot\text{m}^{-3}$ ) and time (min). LCt is useful to determine the lethality of variable combinations of concentration and time.<sup>6</sup> Correspondingly,  $\text{LCt}_{50}$  signifies the lethal concentration time sufficient to kill 50 % of a given population. For example, a compound with an  $\text{LCt}_{50}$  of  $50 \text{ mg}\cdot\text{min}\cdot\text{m}^{-3}$  is lethal to 50 % of the population that has received an exposure of  $50 \text{ mg}\cdot\text{m}^{-3}$  for a period of 1 min. The same compound is also lethal at a concentration of  $5 \text{ mg}\cdot\text{m}^{-3}$  for 10 min.

## **1.2. Historical Use of CWA**

Civilizations have resorted to the use of chemicals since the beginning of warfare. Early use occurred by burning materials with the aim to smoke out well entrenched defenders. Eventually, primitive chemical warfare developed into burning specific plants or materials such as sulfur containing compounds to increase effectiveness.<sup>7</sup> Although the technology has improved, chemical warfare remains a viable method of combat today. The historical use of CWA has been succinctly summarized in recent works.<sup>4,8</sup>

The history of CWA use demonstrates several important points. First, CWAs have been employed around the world, with no area that is free from the threat. Second, repeatedly throughout history chemical weapons have been used despite international condemnation and treaties banning their use. Additionally, independent rogue

organizations may now have access to these deadly chemicals. Finally, the potency and persistence of CWAs have increased dramatically. Furthermore, the decontamination process following CWA exposure has not kept pace with the development of evolving threats. The need for detection currently also demonstrates the necessity for new continuous decontamination approaches.

### **1.3. CWAs of Interest**

The CWAs of concern for most decontamination efforts fall into one of two classes, blister and nerve agents. The primary blister agent, *bis*(2-chloroethyl) sulfide, is known as mustard gas and by the NATO designation HD. HD was first used in World War I and since has been one of the most produced and stockpiled agents in world history.<sup>4</sup> HD is an oily liquid that is clear to pale yellow in color and acts as an alkylating agent that reacts with skin resulting in severe blisters.<sup>4</sup> The eyes and lungs are particularly sensitive to this agent and exposure to a very large dose ( $LD_{50} = 100 \text{ mg/kg}$ )<sup>9</sup> can result in a systemic response resulting in death. The primary decomposition pathway for HD is oxidation of the sulfur to the sulfoxide. Secondary oxidation to the sulfone product regenerates a vesicant molecule. Oxidation of HD has been achieved with oxidative agents such as hypochlorite and peroxides.

Nerve agents comprise two subclasses, the G-agents and V-agents. G-agents were developed in Germany the 1930's prior to and during World War II and consist of Tabun (GA), Sarin (GB), and Soman (GD).<sup>4</sup> Although all of these are very toxic, with respective  $LD_{50}$  of 1000, 1700, and 50 mg,<sup>9</sup> each has a relatively high vapor pressure<sup>1,3</sup> and can be degraded via aqueous hydrolysis. Hydrolysis with ambient moisture and

evaporation into the atmosphere are likely natural routes of agent attenuation. Therefore, decontamination of G-agents is not a major target for current research efforts. On the other hand, the primary V-agent, VX (*O*-ethyl-*S*-(2-diisopropylaminoethyl) phosphonothiolate), presents a very difficult decontamination challenge because VX is persistent in the environment and also resistant to hydrolysis. VX is the most toxic agent of those discussed herein. The very low vapor pressure of VX ( $7 \times 10^{-4}$  mmHg at 20 °C) indicates that evaporation is not adequate to rid surface or material from contamination.<sup>3</sup> VX decomposition can follow one of several pathways, the most desirable of which, with respect to decontamination, occurs by oxidation at the S atom, nucleophilic attack on the P atom, then cleavage of the P-S bond.<sup>1</sup>

HD and VX are the particular CWAs of interest concerning surface decontamination because both agents are incredibly persistent in the environment. Neither agent readily evaporates or hydrolyzes, especially compared to the G-agents. Large stockpiles of HD and VX are known to exist throughout the world. HD has been extensively stockpiled since WW I because of its effectiveness and simple synthesis. VX has been extensively stockpiled because it is the most potent of the nerve agents. From a chemical perspective, both HD and VX present the most difficult decontamination challenges, as they require strong reactants and also may produce toxic by-products.<sup>1</sup>

#### **1.4. Vesicants**

Vesicant agents, along with nerve agents, pose the greatest threat of surface contamination. Vesicant agents cause serious blistering and chemical burn symptoms upon contact with skin, eyes and lung tissue.<sup>10,11</sup> The principle agent of this class is

*bis*(2-chloroethyl) sulfide, which was highly stockpiled. The name mustard is more commonly used to refer to *bis*(2-chloroethyl) sulfide (Figure 1.1) and originates from the pale yellow color and odor the compound exhibits, which resembles the mustard plant. The yellow color and odor result from impurities present in the mixture when first produced by the Levinstein process.<sup>10</sup> Pure *bis*(2-chloroethyl) sulfide is actually colorless and odorless. The color of mustard agent can range, depending on purity, from clear to pale yellow and even black.<sup>10</sup>

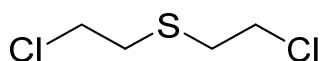


**Figure 1.1.** Structure of the vesicant HD.

HD was highly stockpiled because it is easily synthesized, stable during storage, persistent after release and very effective in causing casualties.<sup>12</sup> As of 2009, there were 11,450 metric tons of HD were declared worldwide.<sup>13</sup> Table 1.1 provides an overview of various physical properties of HD.

**Table 1.1.** Physical properties of HD.

Property	Value
Molecular Weight	159 g-mol <sup>-1</sup>
Liquid Density (@ 20 °C)	1.27 g-cm <sup>-3</sup>
Boiling Point (@ 750 mm Hg)	227 °C
Melting Point (@ 750 mm Hg)	14.11 °C
Vapor Pressure (@ 20 °C)	7.2 x 10 <sup>-2</sup> mm Hg
Volatility (@ 20 °C)	610 mg-m <sup>-3</sup>
Vapor Density (air = 1.0)	5.4
Solubility in Water (g-100 mL <sup>-1</sup> )	0.11

The blistering effect of HD is attributed to an alkylating mechanism.<sup>14</sup> Generally, a  $\text{Cl}^-$  is eliminated from one terminus, resulting in the formation of the carbocation sulfonium ion with the central heteroatom (sulfur), as depicted in Figure 1.2. The resulting sulfonium ion is very reactive towards a variety of nucleophiles and consequently reacts with the nucleotide guanine in DNA, effectively alkylating the nucleotide. This action is particularly harmful to the skin, resulting in blisters and carcinogenic effects.<sup>11,15-17</sup>

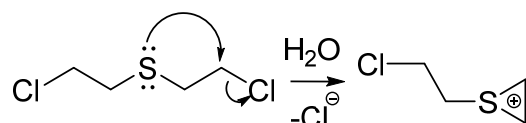


**Figure 1.2.** Formation of sulfonium ion from HD.

The concentration of HD required to induce vesication is extremely low and symptoms can appear at concentrations as low as  $0.003 \text{ mg}\cdot\text{m}^{-3}$ . However, the  $\text{LD}_{50}$  of sulfur mustard, when applied to the skin, is  $100 \text{ mg}\cdot\text{kg}^{-1}$ .<sup>18</sup> The high lipophilicity of HD allows rapid penetration of the skin, at a rate of  $1\text{-}4 \text{ }\mu\text{g}\cdot\text{cm}^{-2}\cdot\text{min}^{-1}$ .<sup>18</sup> Symptoms, including severe blisters, begin to appear 12-24 hours following exposure.<sup>19</sup> This delay in presentation increases the danger of residual contamination due to a possible lapse in recognition of exposure to the agent and consequent inadequate decontamination. Treatment involves application of antibiotics to prevent infection and soothing compounds to relieve painful symptoms resulting from the chemical burn.<sup>20</sup> Respiratory

failure and systemic organ failure can result from excessive exposure of HD to lung and skin tissue. Historically, fatalities often occurred due to secondary infections of the massive blistering of the skin, especially prior to the invention of modern antibiotics.

### **1.5. Nerve Agents**

The nerve agents are a class of CWAs which comprise organophosphorus (OP) compounds that affect the nervous system. Specifically nerve agents, including OP pesticides, act to inhibit the enzyme acetylcholinesterase (AChE) in neurological synapses. In the muscarinic, nicotinic, and the central nervous systems, acetylcholine is an important neurotransmitter. Acetylcholine transfers a signal along the nerve pathway by leaving the axon and subsequently binding to a receptor. AChE facilitates the hydrolysis of acetylcholine into acetic acid and choline, which release from the receptor and reactivate the cholinergic receptors.<sup>21</sup> Release of the neurotransmitter from the receptor is essential to deactivate the nerve signal. Nerve agents inhibit AChE by irreversibly binding to the hydroxyl group of a serine in the active site of the enzyme.<sup>21,22</sup> The serine hydroxyl of AChE is phosphorylated by the nerve agent through the loss of a leaving group from the nerve agent.

The active site of AChE is inhibited by phosphorylation and AChE cannot catalyze acetylcholine. Therefore, an accumulation of acetylcholine occurs at the receptor and causes overstimulation of the nervous pathway, which results in cholinergic toxic effects.<sup>21</sup> The muscarinic receptors almost exclusively use acetylcholine as the neurotransmitter to conduct signals and are therefore the most affected. Exposure to nerve agents initially present symptomatically as miosis, bronchoconstriction, salivation,

lacrimation and loss of muscle control.<sup>18</sup> Frequently, symptoms appear 2-18 hours following exposure.<sup>23</sup>

Another aspect concerning nerve agents is the permanent and irreversible binding to AChE. The amount of time required to irreversibly bind is referred to as aging. Aging is a result of the dealkylation of the bound agent, resulting in a very stable phosphorous-AChE bond.<sup>21</sup> The time required for aging to occur varies; the faster the agent ages the more rapidly treatment must be administered following exposure.<sup>24</sup> Once aging has occurred, treatment has no effect and the only relief comes from the production of more AChE by the body, which can take several months if a lethal dose has not been administered. Treatment of nerve agent exposure focuses on the timely administration of a mixture of atropine and oxime solution, which stoichiometrically blocks further acetylcholine from binding to the receptor and allows the release and degradation of the nerve agent.<sup>18</sup>

Nerve agents can be divided into two subgroups consisting of the G-agents and the V-agents. The “G” in G-agents stands for either “German” or “Germany.” The “V” in V-agents does not necessarily represent a word, but has been designated to represent a series of particularly persistent agents. The G-agents were developed in Nazi Germany during the 1930’s and 1940’s.<sup>25</sup> The most important agents of this group are *O*-ethyl *N,N*-dimethyl-phosphoramidocyanidate (Tabun), isopropyl methyl-phosphonofluoridate (Sarin) and pinacolyl methyl-phosphonofluoridate (Soman), as seen in Figure 1.3.

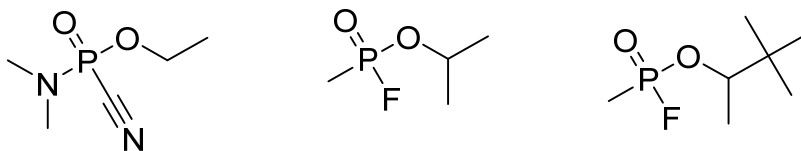


**Figure 1.3.** Structures of GA, GB, and GD.

NATO has designated the G-agents Tabun, Sarin, and Soman with the code letters GA, GB, and GD, respectively. Sarin and Soman are similar in structure in that they are both methylphosphonofluoridate compounds, only exhibiting variation in the alkoxy substituent. Toxicities of the nerve agents are shown in Table 1.2.

**Table 1.2.** Toxicities of nerve agents.

Toxicity, administration	GA	GB	GD
LD <sub>50</sub> Rat, oral ( $\mu\text{g}\cdot\text{kg}^{-1}$ )	3700	550	NA
LD <sub>50</sub> Rat, subcutaneous ( $\mu\text{g}\cdot\text{kg}^{-1}$ )	193	103	75
LD <sub>Lo</sub> Human, skin ( $\text{mg}\cdot\text{kg}^{-1}$ )	23	NA	18
LCt <sub>50</sub> ( $\text{mg}\cdot\text{min}\cdot\text{m}^{-3}$ )	400	100	70
LD <sub>50</sub> Human; skin <sup>a</sup> (mg) <sup>18</sup>	1000	1700	50

<sup>a</sup>LD<sub>50</sub> Human skin is calculated for a 170 lb male.

Of the G-agents, Sarin and Soman have been the most produced and stockpiled primarily due to their selection as agents of choice by the militaries of the United States and the former Soviet Union.<sup>13</sup> The United States selected Sarin for mass production into its chemical arsenal and currently holds a stockpile of thousands of tons.<sup>13</sup> The former Soviet Union, which includes Russia and several Eastern European nations, stockpiled large amounts of both Sarin and Soman in its chemical arsenal, which is evident by the remaining declared stockpiles.<sup>13</sup>



However, G-agents are not considered persistent contaminants relative to HD and VX. At room temperature, Tabun and Soman exhibit hydrolysis half-lives of 8.5 and 5.25 hours, respectively. These half-lives are considerably short, especially in comparison to that of VX, which is 41 days.<sup>2</sup> Also, while Sarin exhibits a hydrolysis half-life which can range from 39 to 135 hours, a relatively high vapor pressure causes Sarin to evaporate and quickly diffuse into the atmosphere to non-lethal concentrations leaving the surface free from contamination.<sup>2</sup> Table 1.3 presents several physical properties of the G-agents.

V-agents are organophosphorus nerve agents, more specifically phosphonothioate nerve agents, first developed by British scientists in the 1950's.<sup>25</sup> V-agents are similar to G-agents in that they are organophosphorus compounds; however the primary difference is the thiolate sulfur bound to the phosphorous, which results in increased toxicity.

**Table 1.3.** Physical properties of GA, GB, and GD.

	<b>GA – Tabun</b>	<b>GB – Sarin</b>	<b>GD – Soman</b>
Molecular weight (g-mol <sup>-1</sup> )	162	140	182
Liquid density (g-mL <sup>-1</sup> )	1.07 @ 25 °C	1.102 @ 20 °C	1.02 @ 25 °C
Freezing point (°C)	-50	-56	-42
Boiling point (°C) (@ 750 mm Hg)	247	147	167
Vapor pressure (mm Hg @ 25 °C)	7.0 x 10 <sup>-2</sup>	2.9	0.4
Volatility (mg-m <sup>-3</sup> @ 25 °C)	610	17,000	3,900
Vapor density (air = 1.0)	5.63	4.86	6.33
Solubility in water (g agent/g water)	9.8/100 @ 25 °C	miscible	2.1/100 @ 20 °C

There are several V-agents, however *O*-ethyl *S*-(2-diisopropylaminoethyl) methylphosphonothioate, known as VX, is the most toxic and most important agent for research due its military importance. *O*-isobutyl *S*-(2-diethylaminoethyl) methylphosphonothioate, known by the NATO code VR, is the Soviet isomer of VX and is also of military significance. Structures of both VX and VR are shown in Figure 1.4. Because of its structural similarity, VR has a decontamination mechanism similar to VX. This research does not specifically focus on VR, as any work related to VX is believed to have a direct application to VR as well.

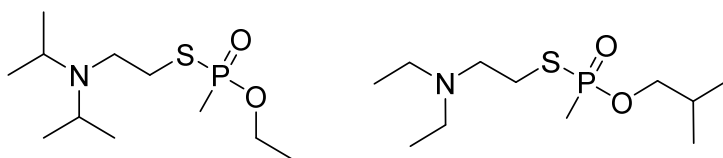


**Figure 1.4.** Structures of VX (left) and VR (right).

VX, in addition to Sarin, was selected by the United States military for mass production and stockpile.<sup>13</sup> VX, an amber colored, tasteless, and odorless oily liquid, has a human dermal LD<sub>50</sub> of 0.040 mg·kg<sup>-1</sup> and an inhalation LCt<sub>50</sub> of 30 mg·min·m<sup>-3</sup>.<sup>23</sup> Because the values of VX are much lower than those of G-agents, VX requires a far lesser dose to be fatal. Table 1.4 presents several significant and pertinent physical properties of VX.

**Table 1.4.** Physical properties of VX.

Property	Value
Molecular weight	267 g-mol <sup>-1</sup>
Liquid density (@ 25 °C)	1.01 g-mL <sup>-1</sup>
Melting point	-50 °C
Boiling point (@ 750 mm Hg)	298 °C
Vapor pressure (@ 25 °C)	7.0 x 10 <sup>-4</sup> mm Hg
Volatility (@ 25 °C)	10 mg-m <sup>-3</sup>
Vapor density (air = 1.0)	9.2
Solubility in water (@ 25 °C)	30 g/100 g*

\*VX is miscible in water below 9.4 °C

### 1.6. Decontamination Solutions

Current decontamination processes utilize liquid solutions to chemically degrade the agent. Typically, an exposed surface is rinsed with the selected solution and scrubbed vigorously. Yet, successful decontamination solutions fall short in many aspects. They are often corrosive and caustic to the individual performing the decontamination as well as the asset being decontaminated.<sup>26</sup> Furthermore, the solution may merely wash away the contaminant and, if aqueous, result in large volumes of contaminated water.

The first military decontamination solutions used were bleaching powders developed by the allies in WW I, which consisted of a solution of calcium hypochlorite (Ca(OCl)<sub>2</sub>). Dakin's solution was also employed, which is composed of sodium hypochlorite and boric acid; however, this solution is unstable once mixed, requiring on-site preparation and immediate use.<sup>27</sup> Current protocols recommend 0.5 % sodium or calcium hypochlorite solutions for decontamination of the skin, while a 5 % concentration is recommended for equipment.<sup>18</sup> However, equipment composed of aluminum, such as aircraft, are incompatible with hypochlorite solutions due an extreme

susceptibility to corrosion. Numerous specialized decontaminating solutions have been developed throughout the years, however most fall short of being effective, non-corrosive and safe to use. This frequently results in the use of soap and water solutions, which do not degrade or detoxify the contaminants.

Decontaminating agent, noncorrosive (DANC), a commercially available product, is composed of a 1 to 15 wt% solution of the active chlorine compound dichlorodimethylhydantoin in tetrachloroethane. DANC is effective against HD and VX, but not G-agents. DANC functions through a reaction with  $H_2O$ , forming hypochlorous acid, which then reacts with the agent. DANC facilitates metal corrosion in the presence of moisture and frequently swells and damages polymeric materials, yet DANC is less corrosive than bleaches, while acting faster and possessing superior solubility properties than concentrated hypochlorite solutions. Serious toxicity from inhalation and absorption of DANC through the skin resulted in its discontinuation and it was subsequently discarded by the Navy following World War II.<sup>28</sup>

Decontamination Solution 2 (DS2) was developed in 1951 and incorporated into military protocol in 1960. DS2 is a general purpose, ready to use decontaminant. DS2 also offers long term storage stability and a large temperature range of activity (-26 to 52 °C).<sup>1</sup> The chemical composition of DS2 is diethylenetriamine (70 % w/w), ethylene glycol monomethyl ether (28 %), and sodium hydroxide (2 %).<sup>1</sup> The active component in this solution was found to be the conjugate base of the ethylene glycol monomethyl ether, which works well with both mustard and V-agents at ambient temperatures. A major drawback of DS2 is that it frequently damages polymer based surfaces such as paints,

plastics, rubber, and leather. Because of this, application time is limited to 30 min on such surfaces.<sup>1</sup> DS2 is also harmful upon contact with skin as well as inhalation. During application of DS2 to an affected surface, individuals need to wear full respirator, eye shield, and chemical resistant gloves for protection from the caustic decontaminating solution. A reaction product resulting from DS2 use was found to cause birth defects in rats.<sup>1</sup> Yet another drawback of DS2 is its rapid degradation upon contact with air and large amounts of water, thereby reducing decontamination efficacy.<sup>1</sup> Reactions with ambient atmosphere slowly degrade the decontaminating ability of DS2. These reactions include: the reaction of carbon dioxide with the sodium hydroxide to form sodium carbonate; reaction of carbon dioxide with the amine in DETA to form solid amine carbonate; and the absorption of water.<sup>28</sup> For these reasons and others, DS2 was also discontinued.

An aqueous decontaminant that is applied as a foam, DF-200, was developed at Sandia National Laboratory. Initially DF-100 was developed in 1999, however DF-200 improved upon DF-100 through pH optimization and exhibited a faster reaction rate with HD.<sup>8</sup> DF-200 has shown to completely eliminate GD in 1 minute, VX in 15 minutes, and HD in 15 minutes, in addition to being environmentally benign. DF-200 was developed with the primary objective of decontaminating civilian facilities in the event of a domestic terrorist attack in urban environments,<sup>29</sup> however logistically, this solution is not very practical as it requires foam spraying equipment.

Decon Green Classic is another commercial product that exhibits extraordinary decontamination ability. Decon Green is a solution based decontaminant; however, the

decontaminant has deleterious effects upon coatings and plastics, such as the ocular in a gas mask. New Decon Green was developed to remedy the reactivity of the decontamination solution with coatings and polymers. New Decon Green succeeds in reducing the amount of damage caused to such surfaces; however the decontamination ability is sacrificed.<sup>30-33</sup>

A common problem among all decontamination solutions results from decontamination of agent that is sorbed into a coating.<sup>34-37</sup> A chemical reaction can only occur when the applied solution is in physical contact with the agent.

#### **1.6.1. CWA Decontamination**

CWAs have been a factor on the stage of war for over a century, yet the same concepts still apply for decontamination as do those that were first employed. Decontamination of CWAs is critical since the agents are highly toxic and typically persist for long periods of time following a release. The decontamination chemistry and approach has remained the same, only the disadvantageous effects have been reduced with each subsequent decontamination solution. Briefly, basic hydrolysis is the ideal degradation pathways for G-agents and oxidation is the preferred pathway for HD and VX.<sup>1</sup> HD is very insoluble in water, which limits its susceptibility toward hydrolysis, and hydrolysis of VX can result in the production of by-products which are nearly as toxic and more persistent such as EA-2192 (Figure 1.5).<sup>1</sup>

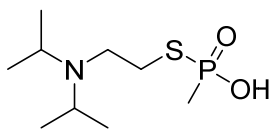


**Figure 1.5.** Chemical structure of EA-2192, a by-product resulting from the hydrolysis of VX.

Decontamination of surfaces which have been exposed to CWAs is of concern to not only military equipment and personnel, but also civilian and public buildings. Numerous decontamination systems have been developed since the development of CWAs, most of which were developed for decontamination of military assets.<sup>1</sup> The conventional approach to surface decontamination is a post-exposure wash or rinse with a decontamination solution, which can either simply rinse the agent away or chemically react with and break down the contaminant. The latter option is more desirable in that the toxic agent can be decomposed into non-toxic by-products, thereby resulting in a reduced potential of personnel exposure.

Due to the incredible toxicity of CWAs, decontamination research is initially performed with chemicals that simulate CWA in both chemical and physical properties, while exhibiting reduced toxicity and health risk. Such molecules are referred to as simulants. The physical properties that are significant when selecting simulants include vapor pressure, solvent miscibility, melting point, and surface tension. Equally important to consider is chemical reactivity. Chemistry required to decompose live agents must be able to be simulated in the selected simulants. Therefore, the simulant molecules must exhibit comparable chemical structures, atomic composition, acidity, basicity, and redox potential.

In early decontamination research, simulants were selected primarily by similarity in chemical structure. Recently, computational models, as well as thorough literature surveys, confirmed that the conventional simulants are indeed the most appropriate.<sup>38</sup> Therefore, the simulants utilized in this work for HD are 2-chloroethyl ethyl sulfide (2-CEES) and 2-chlorethyl phenyl sulfide (2-CEPS). Nerve agent simulants selected for this study included Demeton-*S* and Malathion.

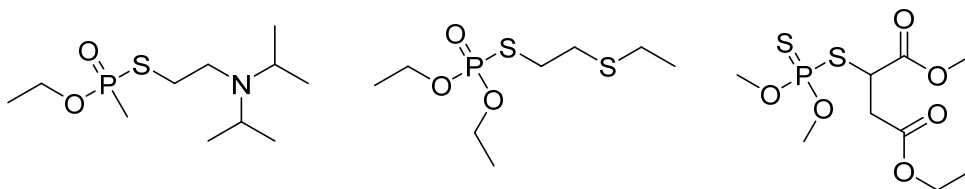


**Figure 1.6.** Comparison of the structure of VX (left) to Demeton-*S* (center) and Malathion (right).

### 1.7. Polymeric Coatings

In the simplest sense, polymers are relatively large organic molecules composed of repeating units, or monomers. Conventionally, polymer classes are named by the type of linkage which bonds together each monomer. Furthermore, nomenclature for each specific polymer is based on the name of the individual monomer preceded by the prefix “poly”. The development of polymer chemistry in the 1920’s and 30’s drastically reduced the dependence on natural products for materials such as rubber and led to an explosion of new products and research.<sup>39</sup> Theoretically, an infinite number of materials can be created by merely manipulating the order and chemistry of specific monomers in a



polymer chain. Today, polymeric materials play integral roles in nearly every aspect of daily living, one of which is coatings and paints.

“Coatings” is a general term which can apply to anything that simply covers or coats another object. In the context herein, “*coatings*” specifically refers to polymers which are applied to a substrate for at least one of two primary purposes: (1) to protect from physical damage (corrosion, abrasion, etc.) and (2) to enhance appearance (color and gloss). This rather straightforward definition includes a large range of materials which have been developed for one or both of these intentions. A commonly used synonym for coatings, which also implies a primary intention of enhancing appearance over providing physical protection, is the term paint. In the most general sense, paint is a polymer film applied to cover a surface. Often, paints are polymers dissolved in organic solvents which when cast and solvent evaporated, result in a thin polymer coating.

A major development in the last few decades in paint technology has been water-based systems. The most commonly known water-based system is latex paint, a class which comprises typical interior household coatings sold at most home improvement stores. Latex paint is a coating formed from an emulsion of polymer micelles in water.<sup>40</sup> As the paint dries, water evaporates and the latex particles become closer in proximity to one another, eventually disrupting the micelles formed by surfactant molecules and coalescing into a continuous, entangled polymer film.<sup>41</sup> While latex coatings offer benefits in regards to volatile organic compound (VOC) emission, as they only off-gas water vapor, coatings formed from latex solutions typically have poor resistance to abrasion and organic solvents (or for that matter CWAs). For these reasons, organic

based coatings, such as polyurethanes, are still used for applications requiring high performance.

Important physical properties for polymeric coating material are storage modulus, Young's modulus, glass transition temperature ( $T_g$ ), tack, oxygen/air permeability, and degradation onset temperature. The storage modulus of a material can be thought of as a function of its flexibility. A low storage modulus would indicate that a material can easily be deformed, i.e. flexible. Young's modulus, or elastic modulus, is a ratio of tensile stress and tensile strain over the initial 5 % strain of a material. For example, a low Young's modulus is indicative of a material that can easily be stretched. Glass transition temperature ( $T_g$ ) is the temperature above which a semi-crystalline polymer is rubbery and below which it is glassy and more brittle. For each of these properties, there is a desirable range in which the material functions best.

#### **1.7.1. Polyurethanes**

Polyurethane (PU) is a class of polymer in which the main covalent bonding between monomers is a urethane linkage. Typically the urethane linkage is formed by the reaction of an isocyanate end group with a terminal hydroxyl (Figure 1.7); however, there are other methods. To form a polymer, diisocyanates are reacted with diols, which subsequently grow via a step-growth polymerization into a high molecular weight molecule.<sup>39</sup> PUs are significant commercial polymers due to their physical properties, which include robust strength, elasticity, rigidity, cross-linking potential, and hydrolytic stability. PU foams can be synthesized and modified to become fire retardant for use as cushions and thermal insulation.<sup>42</sup>

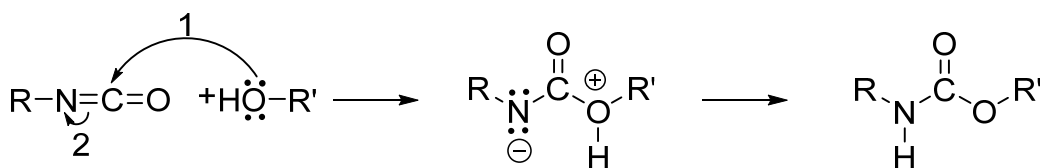


**Figure 1.7.** Formation of a urethane linkage by the reaction of an isocyanate and a primary alcohol.

Polyurethanes have emerged as useful polymers from which to create robust performance coatings due to their aforementioned advantageous properties.<sup>43</sup> Thermoplastic polyurethanes are elastic polymers composed of diisocyanates and diols. Incorporation of long and short chain diols in the same system results in a biphasic material with soft and hard segments, respectively. Polyester based polyurethanes exhibit good thermo-oxidative stability and resistance to oil. Polyether based polyurethanes afford excellent low temperature performance and resistance to microbial degradation.<sup>44</sup> Mechanical properties such as elasticity and strength can be modified by employing various hard and soft segments to control the level of crystallization and cross-linking.<sup>39</sup>

Military applications demand the most robust coatings available in order to withstand the unique physical challenges placed on the material as well as the often very expensive asset over which the coating is applied. Specifically, military coatings need to inhibit corrosion, provide camouflage, withstand rigorous physical abuse, and protect from chemical exposure.<sup>45</sup>

### **1.7.2. MIL-PRF-85285**

Polyurethane coatings encompass a broad range of polymeric coatings that can be applied to a wide variety of surfaces. Due to complexities of coating chemistry and formulations, military coatings are often specified by performance based standards. Standards that require the specified coating exhibit certain physical properties such as: ability to withstand physical stress (scratching, puncture, cracking), resistance to most chemical solvents, ability to withstand a wide range in temperatures, and acceptable adhesion to aluminum and steel. The specific military polyurethane coating utilized in this work is MIL-PRF-85285, which is typically applied as a top coat to Air Force and Navy fixed wing aircraft. MIL-PRF-85285 is a two component high-solids solvent borne polyester based urethane, which consists of a hydroxyl terminated aliphatic polyester cross-linked with an aliphatic hexamethylene diisocyanate (HDI) based polyisocyanate.<sup>46</sup> An additional benefit of MIL-PRF-85285 is that this polyurethane coating also affords compatibility with a variety of potential additive chemistries.

### **1.7.3. Functionalized Polymers**

Conventionally, coatings have been utilized to either impart changes to appearance or to provide additional physical protection to the substrate from the environment. However, recent research has focused on incorporating functionality to coatings in addition to aesthetics and physical protection. Early work on functionalized coatings developed surfaces that exhibited very low surface energy or specific surface roughness to result in a highly hydrophobic surface, therefore facilitating water to bead and easily roll-off.<sup>47</sup> Additionally, antimicrobial coatings and surfaces have been

recently developed. These have been achieved utilizing a variety of methods including post-functionalization, incorporation of antimicrobial additives,<sup>48–50</sup> and utilization of monomers, which orient at the surface, during polymerization to create surface energy heterogeneity.<sup>51</sup>

Numerous functionalized polymers and coatings have recently been developed for various reasons, such as to improve upon existing products or to adhere to increasingly stringent regulations. Polymers which can self-heal at room temperature following a fracture have been developed utilizing phase separated healing capsules.<sup>52</sup> Many different approaches have been taken to create antimicrobial surfaces.<sup>53</sup> Phase separation of amphiphilic molecular additives in coating matrices results in increased surface concentration at the polymer-air interface.<sup>49</sup> Reactive surfaces have potential applications which range from the immediate decontamination of military assets to the improvement of food preservation and packaging.<sup>54,55</sup>

Numerous options are available to modify the surface of polymers to achieve reactive surfaces.<sup>56</sup> A large collection of materials has been developed that relied on biocides and antimicrobials that leach out of the material to kill bacteria. However, this section will focus on the methods used to create coatings with surfaces that prevent the growth of bacteria by utilizing imbedded and covalently bound antimicrobial compounds. Non-leaching biocides provide the benefits of both limiting effects on the surrounding environment and also prolonging antimicrobial lifetime of the surface.

There are two fundamentally different approaches to create functionalized surfaces in polymeric materials. The first is to synthesize the surface or material

completely, then to modify the surface in some way via surface treatments to result in a functionalized surface. A principal method to post-functionalize surfaces is plasma treatment which can chemically modify the very outermost monolayer of a surface from exposure to a plasma discharge. Generally, the plasma, regardless of ion, creates reactive species on the surface subjected to the plasma discharge which can then chemically react with a variety of functional groups including hydroxyl, carboxyl, and carbonyl groups.<sup>57,58</sup> In addition to plasma treatment, electron beam radiation can be used to modify surfaces for functionalization which can range from high energy gamma radiation to relatively lower energy UV.<sup>59,60</sup> However, both plasma and electron beam radiation surface treatment techniques involve highly specialized equipment that is both expensive and difficult to scale up for commercial production.

Wet-chemical methods have also been developed to post-functionalize a variety of polymer surfaces. Typically, the surface is first oxidized then functionalized with the desired chemical moiety. This approach has successfully resulted in antimicrobial polyurethane,<sup>61</sup> Nylon, and polyethylene terephthalate surfaces.<sup>62</sup> Wet-chemical surface modification presents a major disadvantage for functionalizing real-world surfaces such as vehicles and metallic surfaces due to corrosion risks posed by the oxidative nature of the wet-chemical methods.

The second approach involves the simultaneous synthesis and functionalization of the material. This can include either the inclusion of antimicrobial polymer units or monomers, if the surface is polymeric, or the incorporation of antimicrobial additives.

#### **1.7.4. Self-decontaminating Materials**

Conventional materials were typically developed with a single purpose in mind. Coatings tend to perform very well in one aspect (appearance, durability, adhesion, etc.) and neglect various others (resistance to absorption, ease to clean, self-decontamination, etc.). In order to form a system that is capable of withstanding the multitude of potential challenges posed by a particular environment, multiple complimentary materials need to be employed. The addition of functionalities to a material, while maintaining the originally designated performance, ultimately affords the creation of a more robust system by reliance on fewer materials. The functionality with which this work is concerned is self-decontamination. That is to say, to impart to a coating the ability to automatically degrade harmful chemical contaminants to harmless products without the input of manpower.

Self-cleaning surfaces have been the focus of research for many years and are often cited to be inspired by the water beading properties of the lotus leaf.<sup>63</sup> As such, a majority of research in this field has been in attempt to create surfaces that will bead and roll-off water, thereby cleaning the surface by two modes: (1) preventing adsorbates and (2) rinsing off particulates with water roll-off.<sup>64</sup> In the case for CWAs, decomposition and detoxification, in addition to removal, are the most desired functionalities.

Self-decontaminating coatings have recently emerged that utilize the enzyme organophosphorus hydrolase (OPH).<sup>65,66</sup> OPH is an efficient catalyst for the hydrolysis of organophosphates, including G- and V-agents. Recently, OPH has been incorporated into the amphiphilic block copolymer Pluronic F127, in order to create micellar species

and improve the stability of the enzyme. The micelle encapsulated OPH did demonstrate improved stability compare to the native enzyme.<sup>67</sup> However, such catalysts afford limited applicability for robust high performance coatings due to the fact that OPH is a protein based enzyme, thus requiring a specific range of conditions to function and outside of which can be easily inhibited by a variety of relatively benign conditions, including high temperature, low moisture, and pH variation. Furthermore, incorporation of a surfactant of the molecular weight such as Pluronic F127 would greatly affect the surface properties of a polymeric coating.

Several approaches from recent developments that have been made in self-cleaning surfaces and functionalized materials in order to impart antimicrobial activity can be applied to impart active chemical protection into a material. Our group has recently developed a novel class of broad spectrum antimicrobial additives based on quaternary ammonium salts (QAS) specifically for incorporation into polymeric systems. The various polymer systems in which this class of antimicrobial additive has proven successful include polydimethylsiloxanes,<sup>68,69</sup> siloxane epoxy,<sup>70</sup> urethane hydrogels,<sup>71</sup> latex coatings,<sup>48</sup> and polyurethanes.<sup>72</sup> Recently developed amphiphilic antimicrobial peptides have been utilized to afford latex coatings with antimicrobial surfaces.<sup>50</sup> Significant innovation in these works were to utilize amphiphilic molecules to facilitate the automatic rise of the additive to the surface of a coating to achieve very high bacterial killing with extremely low additive loading. This concept of amphiphilicity can be leveraged onto CWA decomposing additives to result in a highly active coating surface.



### 1.7.5. Recent Research in Novel Reactive Systems

Recent research has been conducted in the development and incorporation of novel reactive additives into various coating formulations in attempts to create functionalized coatings. Recent work with reactive coating additives include nonionic biocides,<sup>71</sup> quaternary ammonium biocides,<sup>51,70</sup> surface concentrating biocides,<sup>49</sup> functionalized coatings,<sup>68,69</sup> and antimicrobial peptides.<sup>50</sup> Additionally, polystyrene adhesives containing modified fullerenes have exhibited singlet oxygen generation.<sup>73</sup>

Recently, functionalized polymeric coatings containing photoactive porphyrin species had demonstrated photochemically induced oxidative degradation of CWA simulants.<sup>74</sup> Porphyrins, which are heterocyclic molecules composed of four pyrrole units, are also effective photosensitizers capable of producing singlet oxygen. Covalent modification of each unit affects the photosensitivity and solubility of the molecule. Recently, a covalently modified porphyrin molecule has demonstrated the ability to generate and store singlet oxygen upon exposure to visible light in solution,<sup>75</sup> yet its compatibility and activity within a polymer matrix was not investigated. While effective photo oxidizers, porphyrins are also potent dyes, which exhibit unique color in the visible spectrum. Thus, their incorporation into commercial coating systems imparts undesirable color and added signature to the coating.

Another approach to create self-decontaminating polymers is to incorporate reactive moieties that, when exposed to a particular solution such as hypochlorite solution, can be charged to form reactive species on their surface. One such group has employed this method by attaching *N*-chloramide moieties onto Nomex, a polymeric

substrate.<sup>76</sup> This approach demonstrated successful oxidation of CWA simulants. While both effective and innovative, the down-fall of the rechargeable approach lies in the fact that without solution recharging it is essentially a single use self-decontaminant that lacks turnover. Although the innovative functional coatings are effective, none demonstrate activity against CWAs.

### **1.8. Heterogeneous Catalysis**

A bimolecular chemical reaction in which the reactants are of different phases is a heterogeneous reaction. It follows that a system in which the catalyst is of a different phase from that of the reactants is a heterogeneous catalytic system. Heterogeneous catalysts are the opposite of homogeneous catalysts, species which catalyze reactions comprising reactants in the same phase as that of the catalyst.<sup>77</sup> Self-decontaminating coatings, which are solid coatings containing supported non-leaching reactive catalysts that react with liquid contaminants, are in essence heterogeneous catalysts. Many recent advances in heterogeneous catalysis have emerged from efforts to improve crude oil refinery. The major benefit of a catalyst that is in a different phase from that of the reactants is the simplification it allows in recollecting the catalyst from the reaction mixture following completion. Since heterogeneous catalysts are not consumed in a reaction and allow for simple collection following a reaction since they are in different phases, costs can be reduced by the reuse of a catalyst for multiple reactions. The same concept is at the core of the approach to develop self-decontaminating coatings. A coating which can automatically decompose toxic CWA upon exposure automatically separates reactants and catalyst as the catalyst is embedded in the polymer matrix of the

coating. Therefore the self-decontaminating coating is available for multiple decomposition reactions with minimal, if any, input of energy to recharge the surface.

Numerous additives have been previously synthesized, formulated, and screened for their reactivity against CWA simulants.<sup>8</sup> The most promising additives to result from that study were C<sub>60</sub> and  $\alpha_2$ -K<sub>8</sub>P<sub>2</sub>W<sub>17</sub>O<sub>61</sub>(Ni<sup>2+</sup>·Br), which is referred to in this document as POM3. These additives have since been selected for further chemical modification in an attempt to improve their coating compatibility and to facilitate their automatic surface segregation in order to maximize surface activity against chemical contaminants.

### 1.8.1. Fullerene

C<sub>60</sub> fullerene molecules have been observed to exhibit intriguing photochemical properties, which hold exciting potential for development of a self-decontaminating coating.<sup>78–81</sup> Exposure of C<sub>60</sub> fullerene in solution to visible light is known to cause its excitation to a higher electronic energy state.<sup>78,82,83</sup> The photosensitized fullerene holds the potential to transfer energy to available molecular oxygen, thereby creating reactive oxygen species (ROS).<sup>79,84,85</sup> C<sub>60</sub> fullerene is first excited to its singlet state C<sub>60</sub> (<sup>1</sup>C<sub>60</sub>), which then through intersystem crossing (ISC), forms the triplet state species of C<sub>60</sub> (<sup>3</sup>C<sub>60</sub>). <sup>3</sup>C<sub>60</sub> has a lifetime on the order of  $\mu$ s whereas <sup>1</sup>C<sub>60</sub> exhibits a lifetime of several ns.<sup>78,86–88</sup> This triplet state species of fullerene has the ability to convert ground state triplet oxygen (<sup>3</sup> $\Sigma_g^-$ ) into singlet oxygen (<sup>1</sup> $\Delta_g$ ), a ROS.<sup>79,84</sup> The combination of a high quantum yield<sup>79</sup> and low rate of degradation by ROS of C<sub>60</sub> fullerene<sup>78</sup> make this molecule extremely attractive as a photoactive coating additive. Extensive studies have

been conducted to analyze and characterize the photosensitivity of C<sub>60</sub> in solution with varying degrees of success.<sup>84,86,89–92</sup>

Although extensive studies have been conducted with regards to C<sub>60</sub> fullerene, little has been done in the way of the direct incorporation of fullerene into a coating polymer. The hypothesis proposed here is that the fullerene infused into the coating produces singlet oxygen from the atmosphere by the aforementioned mechanism and subsequently reacts with toxic contaminants that are present on the surface. The action of the additive in the coating should reduce the hazard and subsequently present a surface free from contamination.

### **1.8.2. Polyoxometalates**

Polyoxometalates (POMs) are a broad class of inorganic molecules composed of anionic metal oxide clusters that exhibit a range of dimensions and also afford promising potential for catalysis.<sup>93</sup> A variety of structure types are possible, including Keggin (XM<sub>12</sub>O<sub>40</sub>), Dawson (X<sub>2</sub>M<sub>18</sub>O<sub>62</sub>),<sup>94</sup> and sandwich.<sup>95</sup> POMs have recently been incorporated into materials to result in self-decontaminating materials, the benefit of which would be to actively and automatically degrade and detoxify chemical contaminants upon exposure.<sup>76</sup> POMs are molecules with metal-oxygen cage structures that have been used as catalysts and other applications resulting from the ability to substitute hetero-metal atoms into the cage structure.<sup>96–101</sup>

Dawson type POMs afford the capability to remove one or more metal oxide species from the cage, leaving a void in which functionality can be incorporated. Specifically, transition metals have been inserted into POM structures to improve the

electron transfer capability of the molecule for catalysis applications.<sup>100</sup> Furthermore, the anionic nature of the POM cage can be utilized through ion exchange to graft cations and alter POM solubility. Amphiphilic species can thus be created if organic non-polar moieties are utilized.<sup>102</sup>

### **1.9. Surface Segregation**

The automatic arrangement of additives at the polymer-air interface is surface segregation. Surface concentrating behavior allows maximum additive performance at very low additive loading concentrations, which creates minimal disruption to the primary purpose of the polymer. Surface segregation is a cumulative effect of the interplay between the properties of all the components in a coating formulation including polymer molecular weight, polymer cross-linking density, polymer solution concentration, vapor pressure of solvent, solvent polarity, additive polarity, additive solubility, and additive concentration.

An effective method to facilitate surface segregation is to impart amphiphilicity onto an additive or molecule of interest. Amphiphilic compounds are molecules which exhibit both hydrophobic and hydrophilic regions. Therefore, when amphiphiles are incorporated into a polymeric system of a particular surface energy, the molecule will orient to the lowest energy by aligning at the interface so that the hydrophobic region and hydrophilic regions are each in compatible low energy environments. The chemistry of the amphiphilic quaternary ammonium salt (QAS) additives has been optimized to afford maximum killing of Gram-positive and Gram-negative bacteria, *Bacillus* endospores, as well as to automatically concentrate at the polymer-air interface to allow maximum

surface concentration.<sup>49,103</sup> Therefore, amphiphilic modification of a CWA reactive catalyst has potential to impart surface segregation and afford activity at lower loading concentrations.

### **1.10. Electrospinning**

Recently, another approach to maximize activity of functionalized materials via increased surface area has emerged. Since the activity of a functionalized material is dependent on both the additive and the target being present at the surface, activity can be further improved by increasing the available surface area of a material. The available surface area of polymeric materials can be efficiently increased by electrospinning.

Electrospinning is an intricate process which utilizes electrostatic forces to create polymeric, ceramic, and sol-gel fibers with nanoscale diameters.<sup>104</sup> It can be presumed that surface reactivity will directly correlate with surface concentration of reactive additive. An inherent disadvantage of working with a paint coating system is that the coating exhibits, by its nature, a flat surface, thereby limiting the surface area available for the interaction of contaminant and reactive surface. A surface which was composed of numerous small shapes, for instance fibers, would exhibit a far greater effective surface area to afford far greater potential decontamination sites. Within the past decade, electrospinning methods have been optimized and are capable to create monodisperse polymeric fibers with diameters on the scale of less than 100 nm.<sup>104</sup> A broad range of polymers are compatible with this method of fiber creation. The combination of extreme surface area by way of nanometer scale diameter fibers, in addition to surface segregating additives yields the potential benefit of improved reactivity of the resultant fibrous mat.

Additionally, a material composed of fibers offers applications beyond that of surface coatings and includes fabrics, bandages, composite reinforcement, and filtration.

Electrospinning has recently emerged as a promising method through which to develop novel polymeric fiber and fabric formulations for biological threat protection.<sup>105,106</sup> Work has recently optimized electrospinning conditions to create antimicrobial electrospun Nylon and polycarbonate nanofibers of uniform fiber diameter that exhibit significant bacterial killing (5-log) of Gram-positive challenge.<sup>107</sup> This demonstration of added functionality to electrospun fibers emphasizes the potential of these materials for incorporation of other functionalities, such as chemical self-decontamination.

## **2. SYNTHESIS AND CHARACTERIZATION OF QAS ENCAPSULATED POMs**

### **2.1. Overview**

The ionic nature of polyoxometalates (POMs) affords a facile route for synthetic modification in order to improve compatibility with polymer solutions. A series of amphiphilic QAS have been recently developed that automatically segregate to the surface of paint coatings during drying. The encapsulation of POMs with amphiphilic QAS creates the possibility of a surface segregating POM species with the potential ability to impart chemical agent reactivity to the surface of polymer coatings. While POMs have been encapsulated with QAS in the past, the novel series of QAS have not been investigated and the coordination between QAS and POMs has only been implied from qualitative methods. In this chapter, POM are encapsulated with the series of amphiphilic QAS which span a range of hydrophobic and hydrophilic character. Thorough characterization of these conjugate molecules resulted in the elucidation of the average number of QAS coordinated to each POM and also the exact regions of the QAS that were coordinated to POM.

### **2.2. Prologue**

Polyoxometalates (POMs) consist of a broad class of metal oxide compounds that exhibit catalytic activity towards a variety of substrate, such as CWA simulants.<sup>93</sup> There are various types of POMs, including Keggin, Sandwich, and Wells-Dawson, each differentiated by the shape formed by metal oxide polyhedra.<sup>108,109</sup> Effective oxidative catalysis against CWA simulants makes POMs a very promising class of candidates for



self-decontaminating coating additives.<sup>110</sup> In addition, several POM derivatives have exhibited capability to oxidize toxic chloroalkyl sulfides, the class of compounds in which sulfur mustard is a member.<sup>110</sup> Wells-Dawson polyoxometalates containing substituted heterometal defects have exhibited improved capability of catalytic oxidation.<sup>111</sup> Recent work has demonstrated that the Wells-Dawson polyoxometalate  $\alpha_2$ - $\text{K}_8\text{P}_2\text{W}_{17}\text{O}_{61}(\text{Ni}^{2+}\cdot\text{OH}_2)\cdot 17\text{H}_2\text{O}$  (POM) exhibits decontamination activity against CWA simulants when directly mixed into a commercial coating matrix.<sup>8</sup> Despite the numerous benefits of POMs for toxic chemical catalysis, POMs often exhibit limited solubility in organic polymer matrices, of which coatings are typically composed.

Therefore, modification of POMs presents a viable method to improve the solubility and compatibility of POMs with organic polymer matrices while preserving their catalytic behavior. POMs afford the potential for chemical modification through cation exchange due to their anionic metal oxide composition.<sup>94</sup> Cation exchange can occur upon solvation of POMs in aqueous solution containing suitable cations. If the exchange of ions results in an insoluble product, then the product will precipitate, thus allowing for creative chemical modification through supramolecular assemblies.<sup>112</sup> Ionic encapsulation of POM molecules with surfactant molecules has been a topic of interest for several research groups recently.<sup>100,113</sup> Layer-by-layer deposition of similar POM compounds has been performed;<sup>114</sup> however, such an approach does not allow as broad an application as a direct coating additive. Silica templates have also been employed onto which POMs and quaternary ammonium salts have been adsorbed proximal to one

another to facilitate oxidation.<sup>115</sup> Yet, applications of such devices are limited by the dimensions of the silica template.

It has been shown that amphiphilic coating additives automatically surface segregate to the coating-air interface during curing, thereby increasing the surface concentration of additive.<sup>49,116</sup> Amphiphilic quaternary ammonium salts have been recently synthesized and applied as surface segregating additives in a range of polymeric coating matrices.<sup>70,117</sup> The same concept can be applied toward the encapsulation of POMs to result in a surface segregating amphiphilic molecule. POMs are capable of modification with organic moieties that range in polarity and result in an amphiphilic catalyst.<sup>95</sup> Well-ordered phases of anion clusters and cationic surface lipid bilayers have been observed upon coordination of cetyltrimethylammonium bromide (CTAB) to Keggin-type POMs.<sup>118</sup> However, the effect of encapsulation of POM with a class of amphiphilic QAS that exhibit a range of amphiphilic character has yet to be investigated.

Despite the broad extent of research that has been conducted in regard to encapsulating POMs with QAS, a definitive investigation into the exact coordination between the two molecular components has not yet been performed. Significant research has been performed in the application of NMR to discern intermolecular and intramolecular distances in molecules that contain paramagnetic species, such as Ni.<sup>119</sup> Specifically, <sup>1</sup>H NMR paramagnetic relaxation enhancement (PRE) can be utilized to ascertain relative molecular interactions which occur on the scale of 10-35 Å, such that the proximity of a proton to a paramagnetic species or heterometal in a magnetic field will affect the relaxation dynamics of the proton.<sup>120</sup> Application of PRE has been

successful in determining intramolecular distances of polypeptides<sup>121</sup> and fullerene-peptide interactions.<sup>122</sup> Distances calculated from PRE, which represent the conformation of molecules in solvent, can significantly differ from those calculated from crystal structures.<sup>121</sup> These studies provide precedent that supports the application of PRE to investigate the coordination of amphiphilic QAS-POM conjugates. Thus the synthesis and characterization of novel QAS encapsulating Wells-Dawson polyoxometalates containing Ni heterometal substituents and their molecular coordination are detailed herein.

## **2.3. Results and Discussion**

### **2.3.1. Intramolecular ordering of QAS-POMs**

Precipitation of QAS-POM coordinates from the aqueous reaction solution confirmed successful ion exchange reaction. However, the relative quantity of QAS coordinated to each POM and the molecular orientation of the coordinated QAS-POM are nontrivial. As such, various analyses were performed to both confirm successful synthesis and to elucidate the nature of QAS-POM binding.

Diffuse reflectance infrared spectroscopy with Fourier transform (DRIFT) provided a facile method to analyze the chemical composition of solids and dried powders. DRIFT spectra afforded valuable insight into chemical bonding information that provides an initial glimpse into QAS-POM binding. Neat QAS and POM were analyzed with DRIFT (Figure 2.1) and compared to spectra of QAS-POM complexes (Figure 2.2).

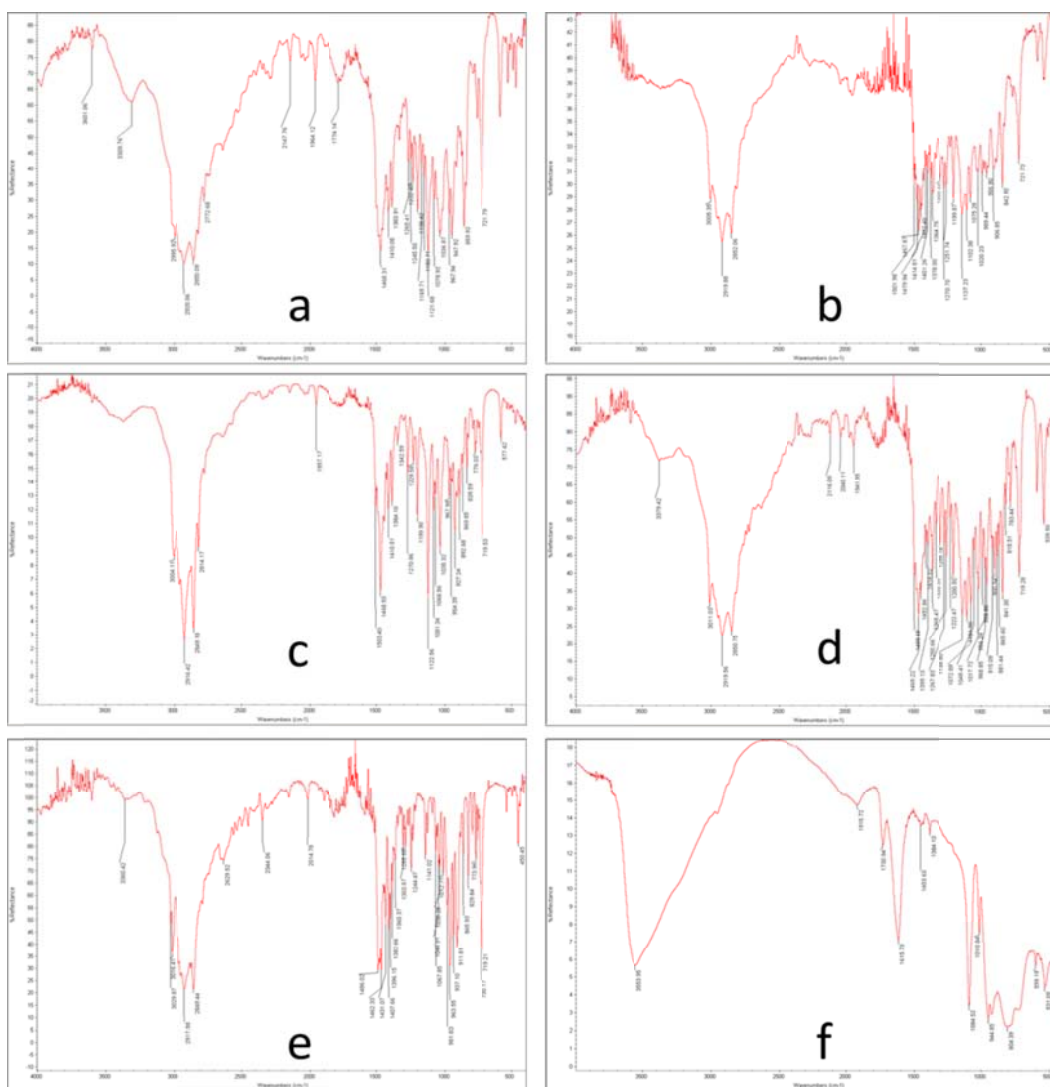


**Figure 2.1.** DRIFT spectra of a) C<sub>12</sub>EO<sub>1</sub>, b) C<sub>12</sub>EO<sub>2</sub>, c) C<sub>16</sub>EO<sub>1</sub>, d) C<sub>16</sub>EO<sub>2</sub>, e) CTAB, and f) POM.

Overall, QAS-POM DRIFT spectra indicated the assimilation of significant vibrations from both POM and QAS. Specifically, the aliphatic stretching modes from 2800-3000 cm<sup>-1</sup> corresponding to CH<sub>2</sub> of QAS and the ether stretching vibrations at approximately 1120 cm<sup>-1</sup> were incorporated into the QAS-POM spectra. As expected,

the absorbance of the ether stretching modes at approximately 1200 and 1120  $\text{cm}^{-1}$  that were observed in the QAS containing ether tail moieties (Figure 2.1a-d) were absent in CTAB spectra (Figure 2.1e). The successful coordination of QAS to POM was suggested from the observation of the ether stretching modes in the DRIFT analysis of the QAS-POM complexes (Figure 2.2). Furthermore, the respective ether stretching modes for neat  $\text{C}_{12}\text{EO}_1$  (1198 and 1121  $\text{cm}^{-1}$ ),  $\text{C}_{12}\text{EO}_2$  (1199 and 1137  $\text{cm}^{-1}$ ),  $\text{C}_{16}\text{EO}_1$  (1199 and 1122  $\text{cm}^{-1}$ ), and  $\text{C}_{16}\text{EO}_2$  (1200 and 1134  $\text{cm}^{-1}$ ) were observed to shift to 1194 and 1117  $\text{cm}^{-1}$  for  $\text{EO}_1$  and 1198 and 1117  $\text{cm}^{-1}$  for  $\text{EO}_2$  when coordinated to POM. The shift in wavenumbers of the ether stretching modes from a wide range in neat QAS to a narrow range upon coordination to POM for each QAS molecule indicated that the ether moieties were in similar chemical environments upon their coordination to POM. Thus, these observations suggest that the ether moiety could reside in close proximity to the POM cage. Vibrational contributions from POM, such as the absorbance due to the asymmetric stretching of  $\text{W}=\text{O}$  and  $\text{W}-\text{O}-\text{W}$  at approximately 950 and 910  $\text{cm}^{-1}$ , respectively, were observed in the IR spectra of QAS-POM coordinates. Taken together, these observations provide evidence that the QAS and POM are electrostatically coordinated, as one would predict.

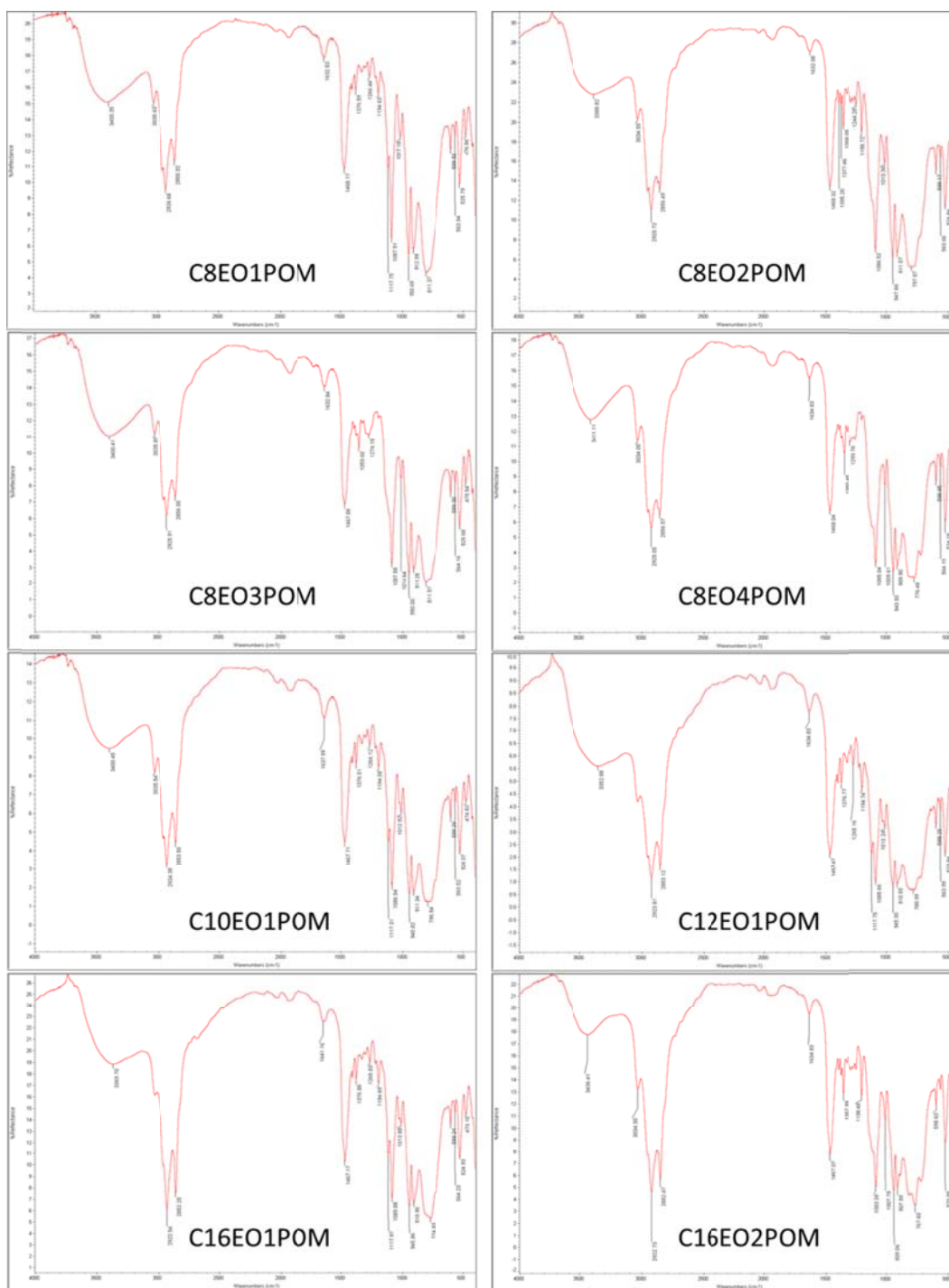


**Figure 2.2.** Diffuse reflectance IR of QAS-POM complexes.

$^1\text{H}$  NMR analyses were performed on QAS and QAS-POM coordinates for comparison. The ethoxy protons of neat QAS were confirmed by the roofing caused by second order coupling between the proximal protons ( $\text{C}_{16}\text{EO}_1$   $\delta = 3.88$  and  $4.00$  ppm). Further peak assignments for  $\text{C}_{16}\text{EO}_1$  and  $\text{C}_{16}\text{EO}_2$  are shown in Figure 2.3.

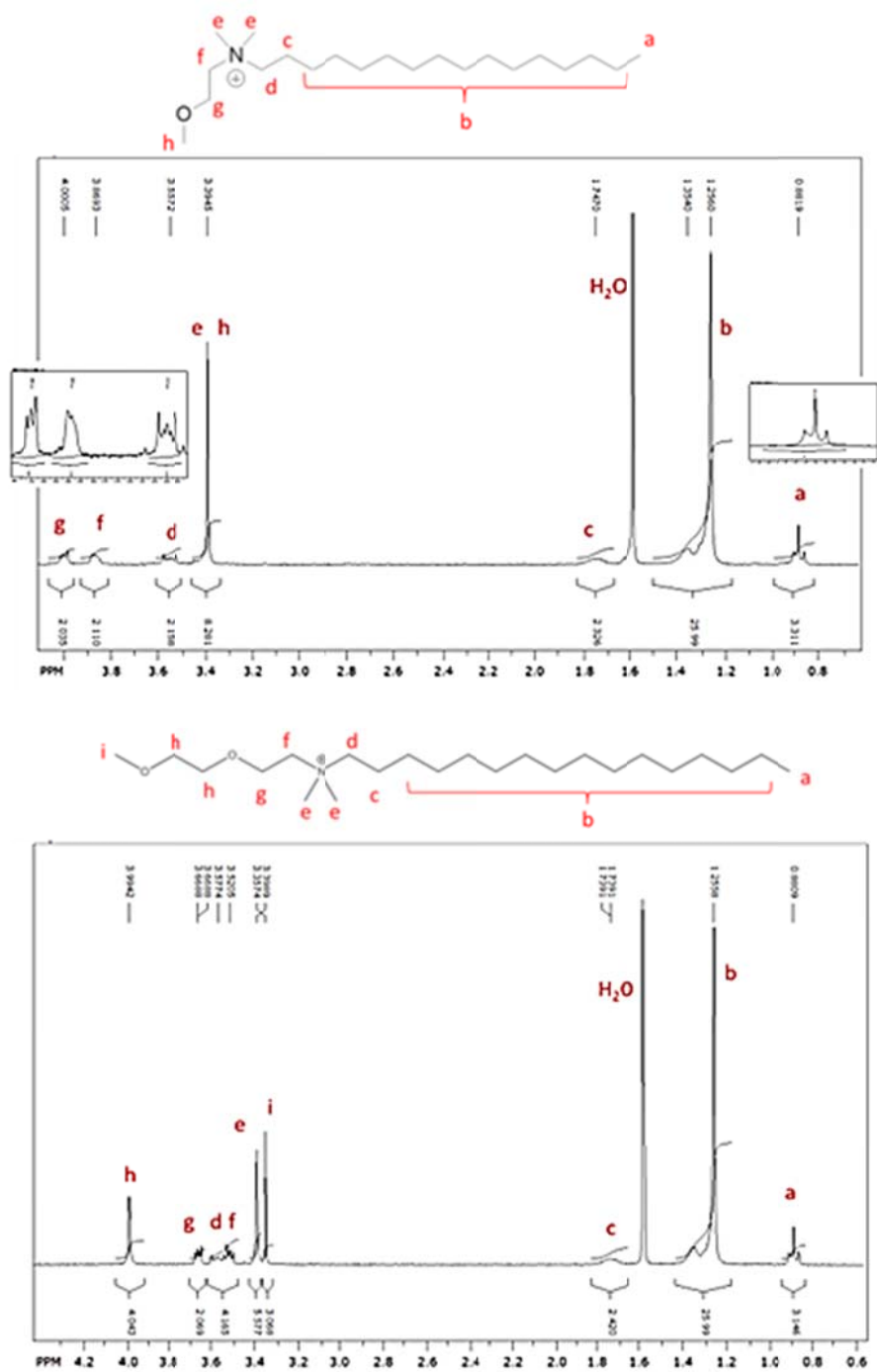


**Figure 2.3.**  $^1\text{H}$  NMR spectra of neat  $\text{C}_{16}\text{EO}_1$  (top) and  $\text{C}_{16}\text{EO}_2$  (bottom) and peak assignments.



Upon coordination to POM, NMR spectra for each QAS-POM molecule exhibited significant peak broadening (Figure 2.4) compared to the neat counterpart of each. Primarily, the NMR line-widths of the C<sub>16</sub>EO<sub>1</sub>-POM3 spectra were significantly broadened. This was observed to the greatest extent for the NMR peaks in the range of 3.4-4.0 ppm. These lines correspond with the protons of the ethylene oxide tail moiety as well as the protons bound to carbons directly bound to the nitrogen atom. Not only were the peaks broadened, but the peaks in the range of 3.4 – 4.0 ppm were also shifted to higher field estimated by the broadened peak roughly centered at 4.1 ppm in the C<sub>16</sub>EO<sub>1</sub>-POM spectrum. Peak broadening resulted from the combination of several factors, the first of which was the presence of paramagnetic heteroatoms in the polyoxometalate structure, both W and Ni. Paramagnetism in the molecule disrupted the homogeneity of the magnetic field and results in both a decrease spin-spin relaxation ( $T_2$ ) and spin-lattice relaxation ( $T_1$ ) of the molecules.<sup>120</sup> NMR peak line broadening indicated decreased  $T_2$ . Additionally, the QAS-POM molecule was significantly larger than the neat QAS, which caused a decreased molecular tumbling rate (correlation time  $\tau_c$ ) relative to the Larmor frequency.<sup>120</sup> Furthermore, the QAS-POM were coordinate systems, in which it is presumed that multiple QAS were coordinated to each POM and thus placed in close proximity to one another. As such, the spin-lattice relaxation ( $T_1$ ) of protons in closest proximity was increased.

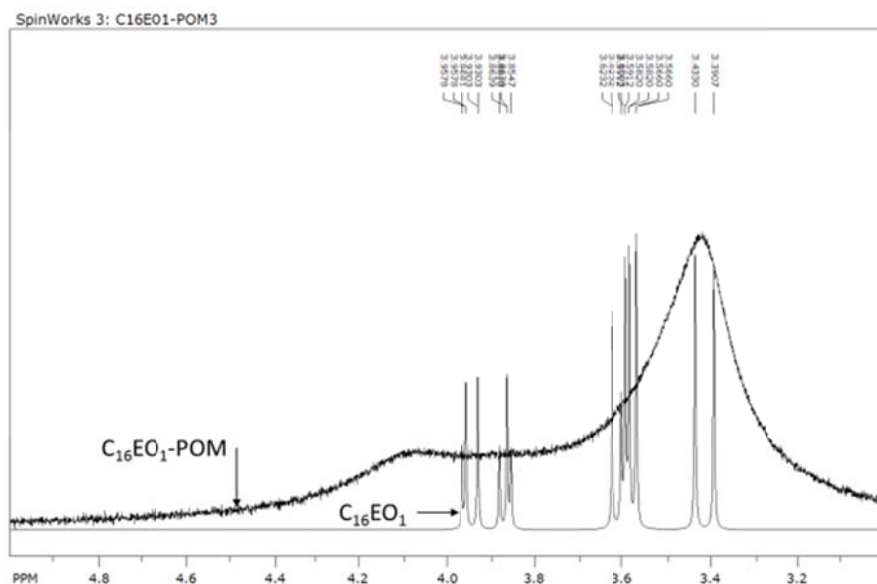


**Figure 2.4.**  $^1\text{H}$  NMR overlay of  $\text{C}_{16}\text{EO}_1$  and  $\text{C}_{16}\text{EO}_1\text{-POM3}$  in the region of 3.0 to 5.0 ppm.

## QAS-POM Coordination via Paramagnetic Relaxation Enhancement

$T_1$  relaxation times were measured via inversion recovery to investigate which moieties of the QAS were in close proximity, and thus coordinated, to POM. In general,  $^1\text{H}$  NMR signals of liquids (small  $\tau_c$ ) and molecules (very large  $\tau_c$ ) exhibit large  $T_1$  relaxation times (on the order of seconds). On the other hand, molecules with intermediate  $\tau_c$  exhibit much shorter  $T_1$  relaxation times due to the close proximity of other protons, the similarity to Larmor frequency, and the potential energy decay pathways they afford.<sup>120</sup> The QAS-POM conjugates in this work resided in the intermediate  $\tau_c$  range. Furthermore, proximity to a paramagnetic species results in a decreased  $T_1$  relaxation time of a proton. Thus, by monitoring the effect that

coordination of QAS to POM has on the  $T_1$  relaxation time for particular  $^1\text{H}$  signals, information pertaining to the environment in which the  $^1\text{H}$  resides was discerned.

Three QAS and their respective POM coordinates were selected for  $T_1$  inversion recovery investigation. These include  $\text{C}_{12}\text{EO}_1$ ,  $\text{C}_{16}\text{EO}_1$ , and  $\text{C}_{16}\text{EO}_2$ . This selection represented QAS of varying alkyl and ethoxy tail lengths, such that their effect on  $T_1$  relaxation, and ultimately their binding to POM, could be determined.

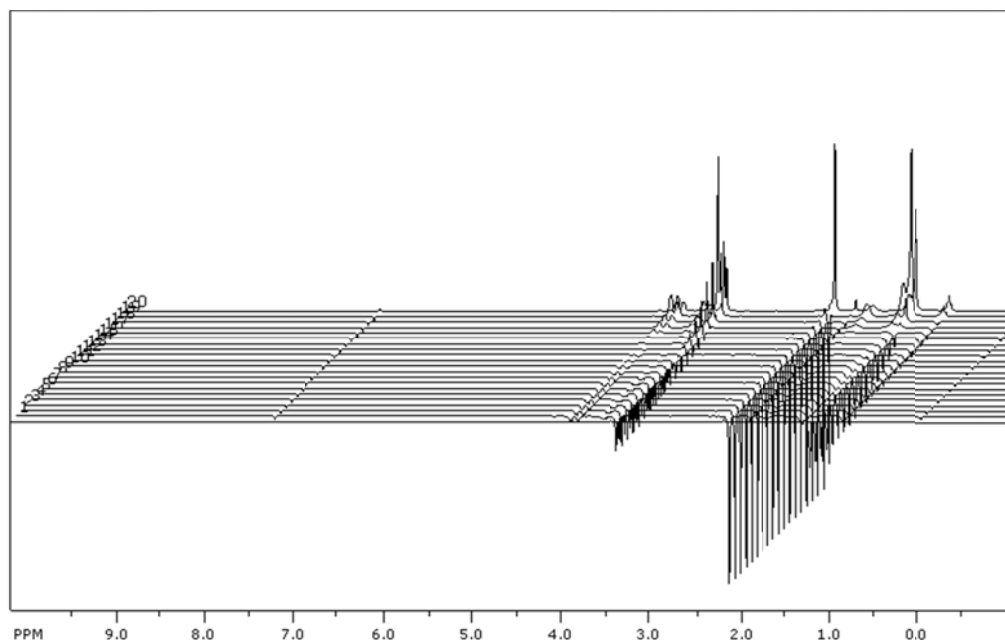


**Figure 2.5.** Representative inversion recovery stacked array of  $^1\text{H}$  NMR spectra of increasing delay (d7) times for neat  $\text{C}_{12}\text{EO}_1$ .

Figure 2.5 presents a representative stacked array of  $^1\text{H}$  NMR spectra. Figure 2.6 presents an example of NMR signal intensity plot that demonstrates the relaxation from negative (inversion), through null, and ultimately to positive intensity for each assigned proton in  $\text{C}_{16}\text{EO}_2$ -POM.

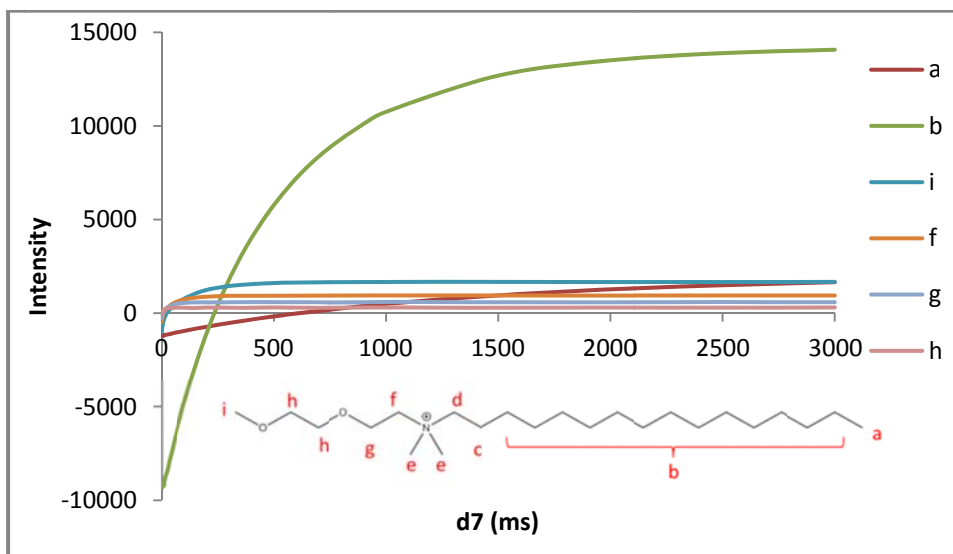


**Figure 2.6.** Representative plot of inversion recovery  $^1\text{H}$  NMR signal intensity vs. delay time (d7) in ms for  $\text{C}_{16}\text{EO}_2\text{-POM}$ .

In an ideal solution, in which the maximum inversion signal intensity is equal to that of the maximum positive signal intensity, the  $T_1$  relaxation time can be estimated by the simple relationship:

$$T_1 = \tau_0 \frac{1}{\ln 2}$$

In the above equation,  $\tau_0$  corresponds to the delay time at which the NMR signal intensity is null. This equation was applied to the inversion recovery experiments performed on the aforementioned QAS and QAS-POM coordinates. The relaxation rate due to paramagnetic effect ( $R_{\text{para}}$ ) can be determined by  $R_{\text{para}} = (T_{1\text{para}} - T_{1\text{diam}})^{-1}$ .  $T_{1\text{para}}$  corresponds to the  $T_1$  relaxation time of the QAS-POM coordinate, while  $T_{1\text{diam}}$

corresponds to the  $T_1$  relaxation time of the diamagnetic QAS. These values were calculated and tabulated in Table 2.1.

**Table 2.1.** Estimated  $T_1$  recovery times (ms) of protons for QAS and QAS-POM conjugates.

$^1\text{H}$	$\text{C}_{16}\text{EO}_1$ (ms)	$\text{C}_{16}\text{EO}_1\text{-POM}$ (ms)	$R_{para}$ ( $\text{s}^{-1}$ )	$\text{C}_{16}\text{EO}_2$ (ms)	$\text{C}_{16}\text{EO}_2\text{-POM}$ (ms)	$R_{para}$ ( $\text{s}^{-1}$ )
a	1855	744	0.81	1753	883	0.56
b	928	313	2.12	870	339	1.80
c	372	20	47.31	294	-	-
d	338	11	87.95	293	13	73.51
e	516	11	88.97	280	33	26.73
f	493	6	164.64	733	13	75.56
g	359	6	163.88	750	10	98.67
h	516	11	88.97	335	3	330.35
i	-	-	-	1584	33	29.67

\* $R_{para}$  – rate enhancement due to paramagnetic effect

The calculated  $T_1$  relaxation times were overlaid onto the respective protons of the chemical structures of QAS and QAS-POM in Figure 2.7. It was clear that coordination of QAS to POM resulted in reduced relaxation times for all of the protons in the system. Furthermore, the protons that exhibited the greatest decrease in relaxation time were those surrounding the ammonium N and along the ethylene oxide tail. These data suggest that the ammonium nitrogen and the ethylene oxide tail were in closest proximity to the paramagnetic species, POM. Therefore, the ammonium nitrogen is electrostatically coordinated to the anionic exterior of the POM, while the ethylene oxide

tail, attracted through polar interactions, is proximal. This proposed coordination orientation necessitates that the alkyl tails are extended outwards from the POM core, presenting a hydrophobic exterior to the surroundings.

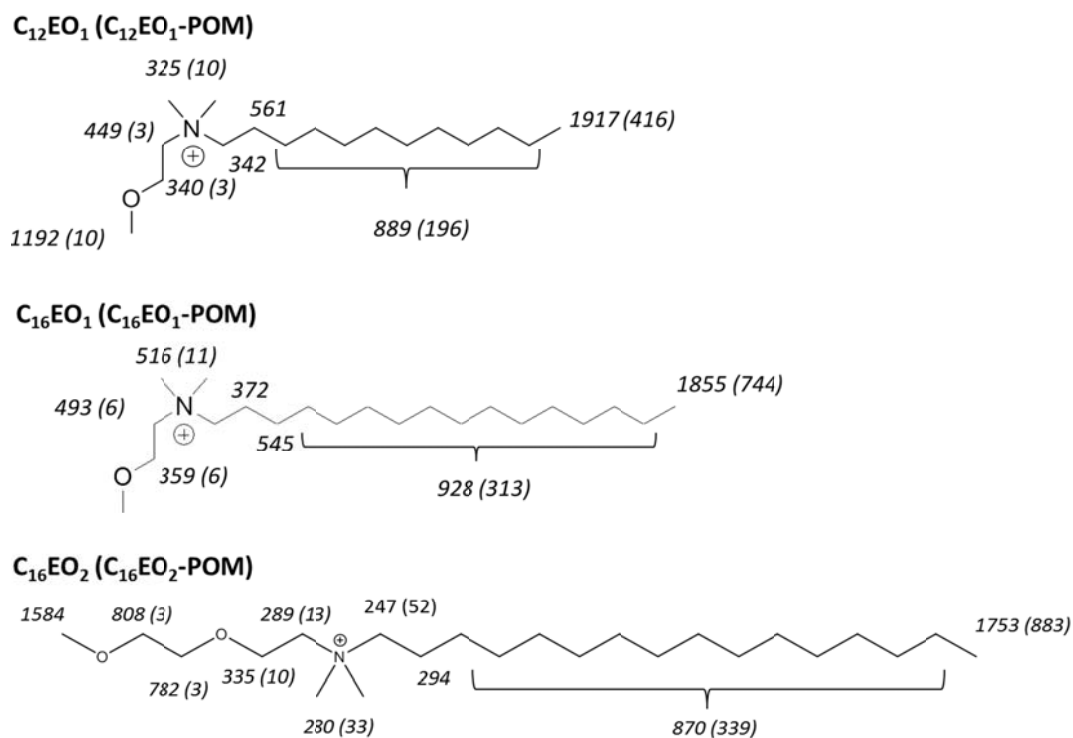


**Figure 2.7.** Estimated  $T_1$  relaxation time assignments (ms) for protons of QAS and QAS-POMs ( $T_1$  in parentheses).

Interatomic distance between a proton and a paramagnetic species can be correlated from  $T_1$  relaxation time measured by inversion recovery through the application of a modified Solomon-Bloembergen equation.<sup>123,124</sup>

### 2.3.2. Intermolecular ordering of QAS-POMs

In addition to the orientation of QAS-POM coordination, the intermolecular ordering between separate QAS-POM molecules and the effects of QAS composition were investigated. Thermal properties of QAS-POMs from TGA are presented in Table 2.2. QAS-POM conjugates were stable to temperatures greater than 200 °C, above which a range of 24 – 41 % mass was lost upon continued heating to 600 °C. TGA of neat POM indicated stability of the molecule to temperatures greater than 600 °C. Thus, the mass loss between 200 and 600 °C was attributed to the loss of the organic QAS component of the molecule. Conversion of percentage of mass loss to mass afforded the molar ratio of QAS to POM for each molecule to be determined. A range of approximately 5 to 8 QAS were coordinated to each POM, depending on QAS composition.

**Table 2.2.** Thermogravimetric data of QAS-POMs.

	Initial Mass (mg)	Mass Loss (mg)	Mols QAS	Final Mass (mg)	Mols POM	QAS:POM Ratio
C <sub>8</sub> EO <sub>1</sub> POM	7.437	1.773	8.19E-06	5.664	1.32E-06	6.22
C <sub>8</sub> EO <sub>2</sub> POM	10.528	3.109	1.19E-05	7.419	1.72E-06	6.92
C <sub>8</sub> EO <sub>3</sub> POM	11.312	3.020	9.92E-06	8.292	1.93E-06	5.15
C <sub>8</sub> EO <sub>4</sub> POM	8.458	2.696	7.74E-06	5.762	1.34E-06	5.78
C <sub>10</sub> EO <sub>1</sub> POM	9.486	2.809	1.15E-05	6.677	1.55E-06	7.40
C <sub>12</sub> EO <sub>1</sub> POM	12.182	4.132	1.52E-05	8.050	1.87E-06	8.10
C <sub>12</sub> EO <sub>2</sub> POM	19.052	6.689	2.11E-05	12.363	2.87E-06	7.35
C <sub>16</sub> EO <sub>1</sub> POM	10.638	4.119	1.25E-05	6.519	1.52E-06	8.27
C <sub>16</sub> EO <sub>2</sub> POM	21.011	8.604	2.31E-05	12.407	2.88E-06	8.01
CTABPOM	5.196	1.762	6.19E-06	3.434	7.98E-07	7.76

A decrease in the QAS:POM binding ratio was expected to be observed with an increase in alkyl tail length from 8 to 16 carbons, since increased nonpolar regions of the longer alkyl tail would experience polar-nonpolar repulsion forces from the polar surface of the POM. Also, an increase in alkyl tail length of coordinated QAS was expected to increase steric hindrance surrounding the POM, discouraging the coordination of additional QAS. However, TGA data indicate that an increase in alkyl tail length of the QAS resulted in increased QAS binding per POM molecule. An increase in alkyl tail length of the QAS results in decreased solubility in aqueous solutions. Therefore, it is possible that due to the increased hydrophobicity imparted to QAS from the long alkyl tail, that the QAS were favored to bind to the POM in order to reduce solvophobic interactions in the aqueous solution compared to the QAS of shorter alkyl tail lengths.

### **Differential Scanning Calorimetry Analysis**

TGA analysis indicated that, on average, between 4 and 7 QAS molecules were coordinated to each POM, depending on QAS composition. To further examine the coordination, DSC analysis was performed on each neat QAS, as well as neat POM (Figure 2.8). Each of the QAS-POM conjugates exhibited reversible melting transitions. Interestingly, DSC analysis of C<sub>12</sub>EO<sub>1</sub> and C<sub>16</sub>EO<sub>1</sub> exhibited only a single melting transition, while the QAS species containing ethoxy tails (EO) of 2 units in length, C<sub>12</sub>EO<sub>2</sub> and C<sub>16</sub>EO<sub>2</sub>, both exhibited two thermal phase transitions. The additional transitions of C<sub>12</sub>EO<sub>2</sub> and C<sub>16</sub>EO<sub>2</sub> occur at 85 and 93 °C, respectively, compared to the primary transition observed for all QAS in the region of 114 - 118 °C. The primary



endothermic transition observed for all QAS corresponds with a solid to liquid melting transition. Research on encapsulated Europium substituted Keggin polyoxometalates attributed a transition at 114 °C of a different, yet comparable, neat QAS species to transitions between lamellar mesophases.<sup>125</sup> Thus, the neat QAS exists in a solid crystalline phase until the transition at heating through 114 – 118 °C. Further, an exotherm in the cooling ramp indicated recrystallization for each QAS, as it occurred at similar temperature as the crystalline melting endotherm.

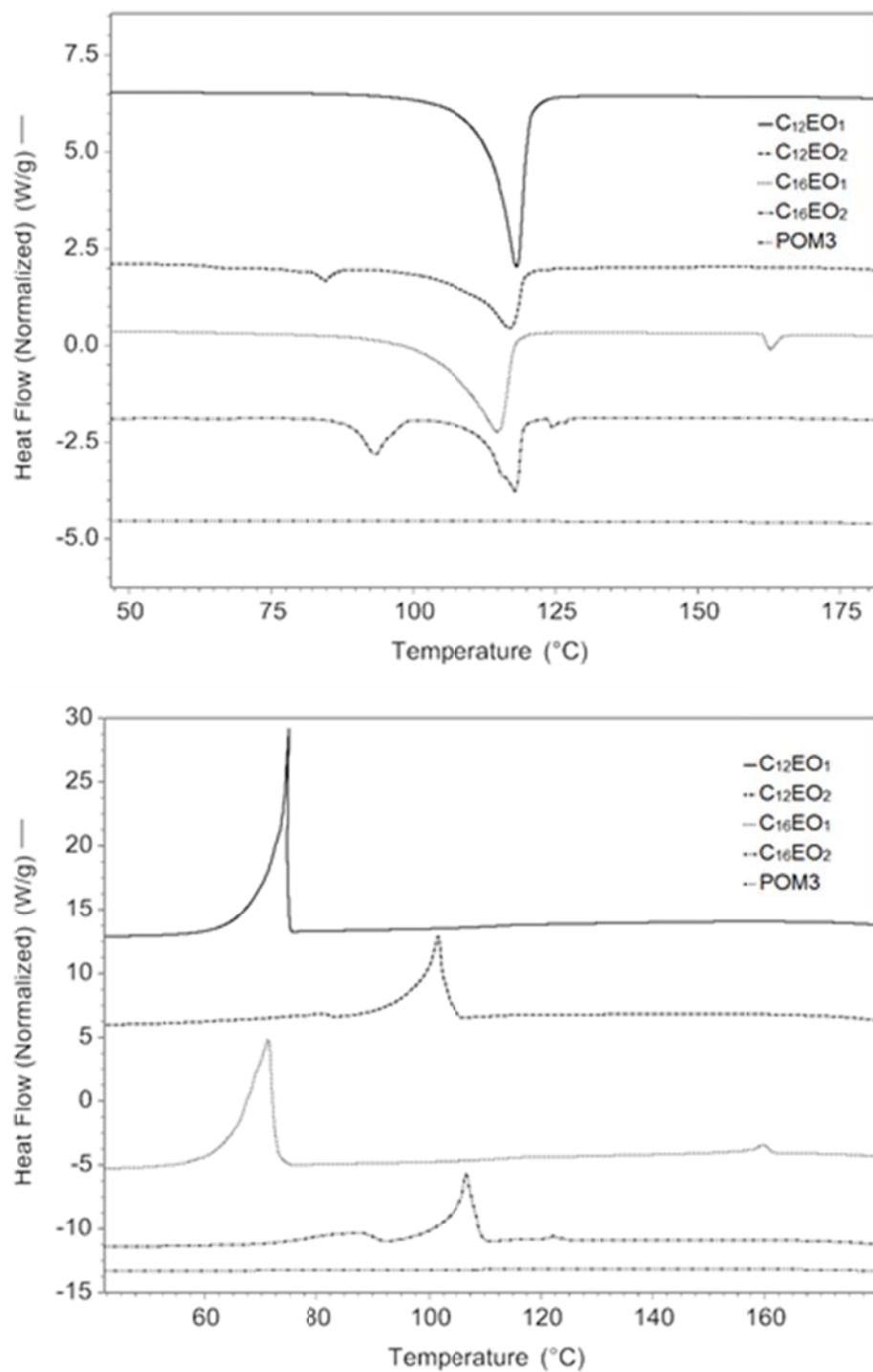


**Figure 2.8.** Heating (top) and cooling (bottom) ramps of QAS and polyoxometalate, uncoordinated.

Analysis of the cooling curves in Figure 2.8 provided additional insight into the hysteresis observed between heating curves of QAS with 1 unit length of ethylene oxide (EO<sub>1</sub>) and two unit lengths of ethylene oxide (EO<sub>2</sub>). Both EO<sub>1</sub> QAS exhibited only a single exothermic transition between the temperatures of 71 and 74 °C during cooling, while the EO<sub>2</sub> QAS exhibited two exothermic transitions, the first in the range of 101 - 106 °C and the second in the range of 81 - 87 °C. It is interesting to note that both of the exothermic cooling transitions for EO<sub>2</sub> occurred at higher temperatures than the single exothermic transition of both EO<sub>1</sub> QAS. Therefore, upon cooling, recrystallization occurred at a lower temperature for the EO<sub>1</sub> QAS than it did for the EO<sub>2</sub> QAS. Also, the secondary transition observed in the EO<sub>2</sub> samples was not significantly shifted from the temperature observed during the heating ramp. Therefore, it was concluded that the additional ethylene oxide unit length contributes a significant role in stabilizing and facilitating the formation of a lamellar mesophase of the QAS during cooling. The additional ethylene oxide tail units likely initiated phase formation amongst the hydrophilic ethylene oxide tail groups, which then facilitated the formation of the crystalline lamellar mesophase of the alkyl tails. This conclusion is supported by the observation of two endothermic transitions in the heating curves of the EO<sub>2</sub> QAS. The lower temperature and lesser magnitude transition resulted from the absorption of energy to transition the ethylene oxide tail sub-phase prior to the primary lamellar mesophase transition of the alkyl tail units.<sup>126</sup>

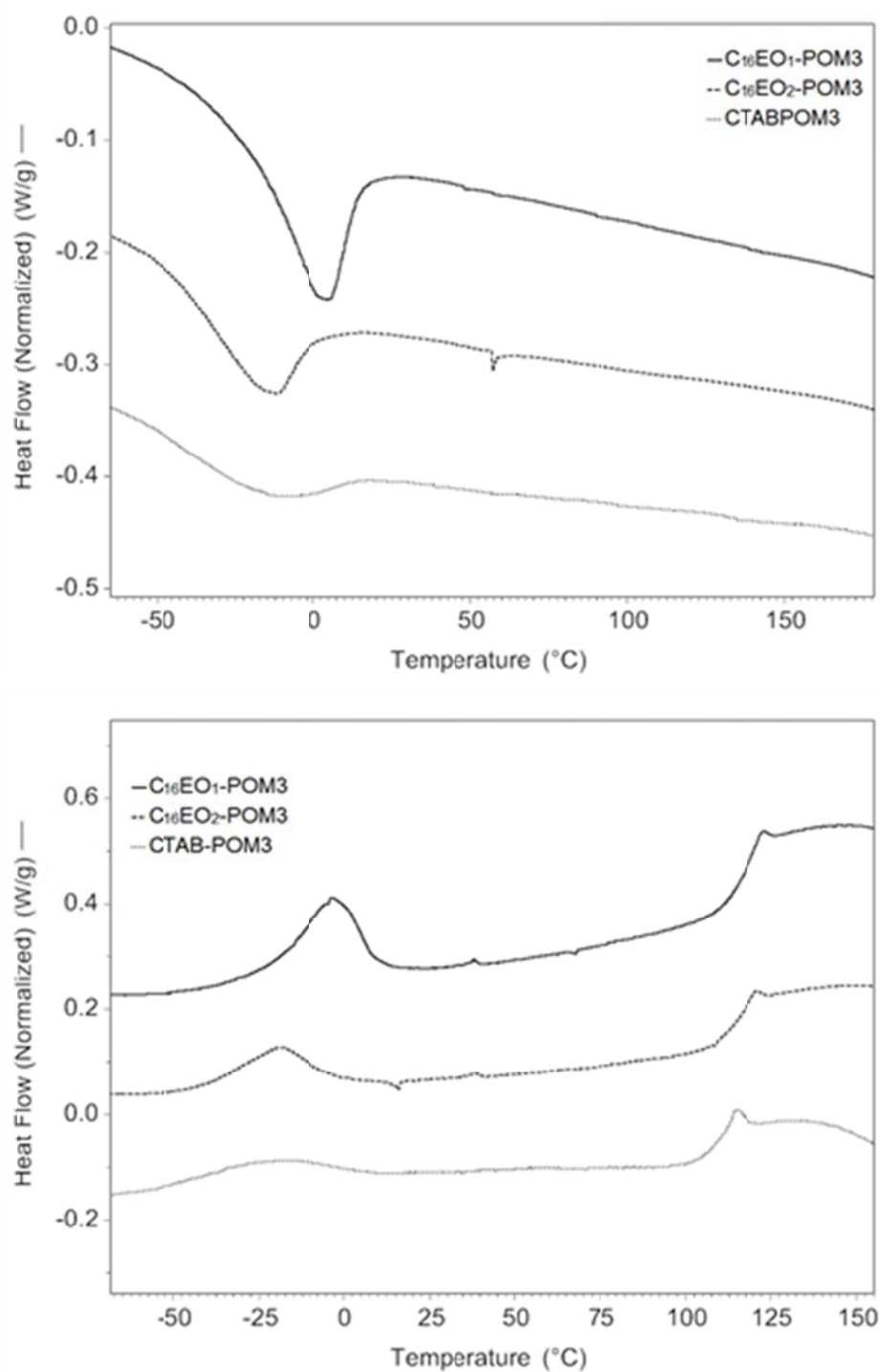


**Figure 2.9.** DSC 2<sup>nd</sup> heating (top) and 1<sup>st</sup> cooling (bottom) ramps of QAS-POMs including enthalpy calculations from peak integrations.

The thermodynamic phase behaviors of QAS-POMs were also investigated with DSC. DSC analysis of QAS-POMs of carbon tail lengths 8-10 did not demonstrate any notable thermal behavior upon heating from -50 to 200 °C. However, the DSC analysis of C<sub>16</sub>EO<sub>1</sub>-POM3, C<sub>16</sub>EO<sub>2</sub>-POM, and CTAB-POM indicate that endothermic transitions occurring between temperatures -50 and 25 °C (Figure 2.9, top). Furthermore, the endothermic transition was determined to be dependent on the carbon and ethylene oxide tail lengths as an endotherm was not observed until the alkyl tail reached 16 carbons in length. Additionally, while a significant difference was observed between the endothermic transitions of C<sub>16</sub>EO<sub>1</sub>-POM and C<sub>16</sub>EO<sub>2</sub>-POM, the only difference in their chemical structure is one single ethylene oxide unit. QAS-POM exhibited crystalline melting endotherms at much lower temperatures than the respective neat QAS. Therefore, the interfacial binding energy of between molecules in crystalline phase of QAS-POM was much less than in neat. Due to combination of the absence of crystalline melting endotherm in QAS-POM species of carbon tail lengths less than 12 and the low temperature endotherm, it is proposed that the alkyl tails between separate QAS-POM molecules were coordinated together through cohesive nonpolar interactions. The shorter alkyl tails did not exhibit such crystalline behavior since it would require an inter-POM radius of interaction that is hindered by their electrostatic repulsion.

Corresponding to the endotherms, exothermic transitions were observed in Figure 2.9 for the same temperature region during the DSC cooling cycles. Considered together, these results confirmed the crystallinity of QAS-POM conjugates of 16 carbon tail length at temperatures below the observed endotherms. Upon heating, the disordering of the

QAS-POM absorbs additional heat relative to the reference resulting in the observed endotherm. Previous studies of branched QAS encapsulating Keggin POMs observed a secondary high temperature transition that increased between 129 and 168 °C as the number of QAS coordinated to POM increased.<sup>127</sup> Yet, only single broad transitions were observed at low temperatures for QAS-POM with alkyl tails greater than 10 carbons in length. The broad transition resulted from heterogeneity within the system.

Comparison of the thermal behavior between neat QAS and the QAS-POM coordinates yielded several insights. Whereas each neat QAS exhibited significant and sharp endothermic transitions upon heating at 114 - 118 °C associated with the melting transition, the corresponding QAS-POM coordinates exhibited broad low temperature (-50 – 25 °C) endothermic transitions. Therefore, the solid-liquid melting transition that existed in the neat QAS did not exist between QAS-POM coordinates. A less stable form of ordering was occurring between QAS-POM coordinates, one which occurred between alkyl tail moieties of separate QAS-POM molecules.

## **2.4. Summary**

The synthesis of novel QAS-POM molecules has been demonstrated. The analysis of the QAS-POM systems detailed herein has afforded the confident determination of the intramolecular and intermolecular orientation with respect to one another. QAS and POM are electrostatically coordinated. The relative interatomic distances of QAS coordinated to POM were determined through utilization of the paramagnetic relaxation enhancement effect. Ammonium nitrogen atom and ethylene oxide tail moieties were determined to be in closest proximity of POM. The quantity of

QAS coordinated to each POM was found to be dependent on QAS composition. Furthermore, crystallinity of QAS-POM species is dependent primarily on the length of the alkyl tail length.

## **2.5. Experimental Methods**

### **Materials**

All solvents and reagents were reagent grade and used without additional purification. Cetyltrimethylammonium bromide (CTAB) was purchased from Sigma Aldrich (St. Louis, MO) and used as received.

### **Synthesis of QAS**

C<sub>16</sub>EO<sub>1</sub>, a surface segregating QAS, was prepared following previously described procedures.<sup>49</sup> Briefly, 7.8 mmol phosphorous tribromide was added drop-wise to a solution of 15.6 mmol 2-methoxyethanol maintained at 0 °C. The solution was allowed to equilibrate to room temperature, and then heated to 90 °C when the solution turned yellow. After the solution was allowed to cool, 6 mL of 10% NaHCO<sub>3</sub> was added. The solution was extracted with diethyl ether and dried with MgSO<sub>4</sub>. This product was reacted with *N,N*-dimethylhexadecylamine under nitrogen in ethanol at 83 °C for 24 h. The resulting C<sub>16</sub>EO<sub>1</sub> product was recrystallized to form an off-white powder.

### **Synthesis of QAS-POM conjugates**

The quaternary ammonium salts utilized in this study were synthesized following a previously reported procedure.<sup>49</sup> Nickel containing polyoxometalates (POMs) were

synthesized by the application of procedures modified from two previous reports.<sup>100,128</sup> Coordination of QAS and POM was achieved via a modification of an ion exchange reaction (Figure 2.10).<sup>100</sup> Briefly,  $\alpha_2\text{-K}_8\text{P}_2\text{W}_{17}\text{O}_{61}(\text{Ni}^{2+}\cdot\text{OH}_2)\cdot 17\text{H}_2\text{O}$  and quaternary ammonium salt were dissolved in deionized water at pH 6-7. The solution was allowed to stir for 10 min, during which time the product precipitated out of solution. The product was subsequently isolated by liquid-liquid extraction with dichloromethane and ether. The organic phase was filtered and dried, resulting in a crystalline green/yellow product. Products were characterized via diffuse reflectance FTIR,  $^1\text{H}$  NMR, TGA, and DSC.

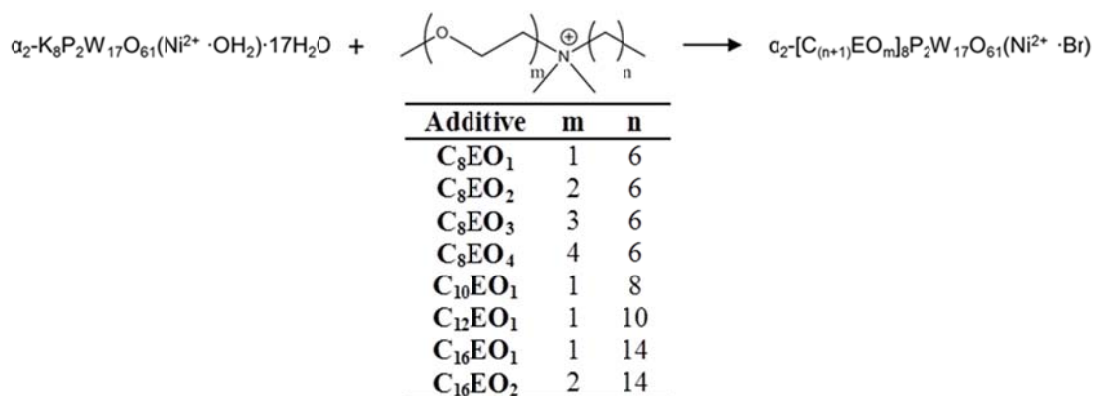


**Figure 2.10.** General synthetic scheme and lengths of ethoxy (*m*) and alkyl (*n*) moieties of QAS-POM coordinates.

### Thermogravimetric analysis

Thermogravimetric analysis (TGA) was performed with a TA Instruments Q50 TGA at a heating rate of 10 °C/min under N<sub>2</sub>. Mass loss at less than 600 °C was correlated to amount of QAS due to relatively lower temperatures at which QAS degrade



compared to POM. By conversion of the percent mass loss to mass and ultimately number of moles, a molecular binding ratio of QAS to POM was determined.

A TA Instruments Discovery Differential Scanning Calorimeter (DSC) was employed. The DSC was first equilibrated to -50 °C under a nitrogen flow of 50 mL/min. Two successive temperature ramps were then performed from -50 °C to 200 °C at a rate of 20 °C/min, between which the sample was equilibrated to -50 °C. TA Instruments Universal Analysis and Trios software were utilized for TGA and DSC analysis, respectively.

### **Diffuse Reflectance FT-IR**

A Thermo Scientific Nicolet 6700 FTIR was utilized for diffuse reflectance infrared Fourier transform (DRIFT) analysis of neat QAS, neat POM, and QAS-POM conjugates. Samples were first mixed with oven dried KBr, finely ground with a mortar and pestle, and placed in an oven at 120 °C for 1 hour prior to analysis.

### **Nuclear Magnetic Resonance (NMR)**

Products were confirmed by  $^1\text{H}$  NMR performed in  $\text{CDCl}_3$  on a Bruker 300 MHz nuclear magnetic resonance spectrometer with a TMS internal standard. Spin-lattice, or  $T_1$ , relaxation was determined by inversion recovery experiments Bruker method “t1ir1d”. Delay time (d7) between 180° inversion pulse (23.18  $\mu\text{s}$ ) and the 90° measurement pulse (11.59  $\mu\text{s}$ ) was increased at increasing intervals between 0.1 ms and 5 seconds. Data analysis and peak deconvolution of NMR spectra was performed using

Spinworks version 3.1.7. Baseline correction and line broadening of 2.0 Hz were employed during spectral analysis.  $^1\text{H}$  signal intensity was plotted versus delay time (d7) and the null time was incorporated into the ideal solution equation to estimate  $T_1$ .

### **3. DISTRIBUTION OF QAS-POMS IN POLYURETHANES**

#### **3.1. Overview**

Surface segregation of additives in polymer matrices has been recently demonstrated with amphiphilic quaternary ammonium salts. In the previous chapter, these were coordinated to POM species in order to facilitate their surface segregation in polyurethane coatings. In this chapter, the polymeric distribution of QAS-POMs in hydrophilic and hydrophobic polyurethane matrices was investigated. It was found that the chemical composition of QAS exhibits a major effect on the polymer distribution behavior of additives. Solvophobic interactions between the QAS-POM additive and polymeric matrix were found to be most significant in determining the dispersion and segregation of the additives. The effects of the relative proportions of QAS-POMs, their loading concentrations, and also the solvent evaporation rate of the polymer solution on surface domain formation are reported.

#### **3.2. Prologue**

The development of multifunctional materials is progressing due to continual advancements in the fields of nanoscience and materials chemistry. Numerous approaches have been utilized to create a broad range of materials that possess functionalities that compliment and supplement those of the primary purpose.<sup>129</sup> One class of materials that have recently been functionalized is polymeric coatings, i.e. paint. While many approaches exist to impart additional functionality, incorporation of

additives into preexisting coating formulations offers potential to result in an active material while maintaining desired properties. In addition to the primary purpose to protect an underlying substrate and to impart aesthetic appeal, the imparting of functionalities such as water repellency, self-healing capability, antimicrobial activity,<sup>72,103</sup> and chemical agent decontamination<sup>74,116</sup> into coatings through the additive approach have been investigated. Despite the breadth of work in the field, numerous additives remain that offer promise to imbue chemical decontamination into polyurethane coatings.

Polyoxometalates (POMs) are a broad class of metal oxide polyhedra that exhibit unique reduction-oxidation capabilities for applications in catalysis.<sup>93,130</sup> Due to their complex metal oxide polyhedral composition, polyoxometalates afford oxidative catalysis of a range of molecules through a variety of reactions.<sup>131</sup> Oxidation is the preferred degradation pathway for the decontamination of chemical warfare agents, as it results in the least toxic by-products for the widest range of agents.<sup>1,2</sup> As such, polyoxometalates are promising candidates as additives for incorporation into polymeric coatings to impart self-decontaminating behavior. Specifically, Dawson type polyoxotungstates have demonstrated oxidative capability of chemical warfare agent simulants.<sup>111,132</sup> However, polyoxometalates are ionic molecules that are soluble in aqueous solutions and are thus incompatible with organic solvent based polyurethane coatings, which are often employed in industrial and military applications due to their robust physical, chemical, and thermal properties.<sup>133</sup>

Chemical modification of polyoxometalates can improve their compatibility as additives with a wide range of materials, including solvent based polyurethane coatings. The ionic surface of polyoxometalates allow for encapsulation with a variety of compounds through facile cation exchange reactions.<sup>134</sup> The cation exchange reaction affords a facile route to encapsulation of polyoxometalates with quaternary ammonium salts (QAS). Amphiphilic QAS have recently been synthesized that automatically segregate to the surface when mixed into coating formulations.<sup>49</sup> As described in the previous chapter, Dawson type polyoxotungstates containing Ni heterometal have been encapsulated with the series of amphiphilic QAS and their coordination has been fully investigated to elucidate that the ionic polyoxometalate core was bound to quaternary nitrogen and ethylene oxide moieties, while exposing an alkyl tail exterior.

The distribution of molecular additives in solution and polymers, such as polyurethane, has been extensively studied.<sup>45,135</sup> Dispersion of additives, such as nanoparticles, in polymeric matrices has been the focus of a very recent study.<sup>136</sup> Various factors affect the distribution of nanoparticles, or additives, in polymer matrices include energetic interactions between the additive and polymer, as well as entropic effects.<sup>137</sup> It has been proposed that particle dispersion in polymers is dominated by the relative dimensions of the radius of the particle and the radius of gyration of the polymer, such that dispersion of particle was favored when the radius of particle is less than the polymer radius of gyration.<sup>138</sup> Polyoxometalates encapsulated with fluorinated groups were found to segregate to the surface in epoxy resins.<sup>139</sup> Another investigation observed the formation of spherical vesicles upon the incorporation of amphiphilic polyoxometalate in

polystyrene.<sup>140</sup> Despite the breadth of research that has been performed, questions remain with regard to the polymeric distribution of additives resulting from the complex modification of polyoxometalates with amphiphilic QAS.

### **3.3. Results and Discussion**

A wide range of analyses were performed on Hydrothane and Tecoflex films containing QAS-POM additives at a variety of loading concentrations in order to determine the factors which affect their distribution behavior in polymer matrices. While both Hydrothane and Tecoflex are commercial polymers, they differ in their chemical structure and thus their inherent chemical characteristics (Figure 3.1). Hydrothane was a hydrophilic polyurethane resin, while Tecoflex exhibited a greater degree of hydrophobicity resulting from the butane diol chain extender that linked two 4,4'-methylenebis(cyclohexyl isocyanate) units by a relatively short segment. This created a larger hydrophobic segment in the polyurethane, thereby increasing its overall hydrophobicity. By comparing their behavior between both resin systems, the effects of polymer properties on additive distribution were elucidated.

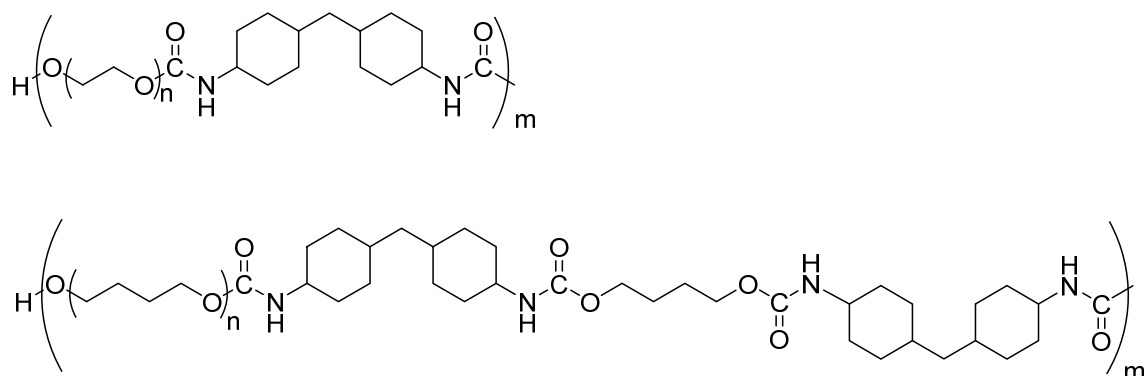


**Figure 3.1.** General chemical structures of Hydrothane (top) and Tecoflex (bottom).

### 3.3.1. Distribution in Hydrothane

In order to ascertain initial behavior of additive in polymers,  $\text{C}_{16}\text{EO}_1$ -POM was first incorporated into Hydrothane polymer formulations at concentrations ranging from 3 – 21 wt%. Neat  $\text{C}_{16}\text{EO}_1$  and neat POM3 were also incorporated into Hydrothane at comparable loading levels in order to discern the distribution behavior of  $\text{C}_{16}\text{EO}_1$ -POM3. Figure 3.2 presents SEM micrographs of the three formulations at loading concentrations from 3 – 21 wt%. Incorporation of  $\text{C}_{16}\text{EO}_1$ -POM3 into Hydrothane resulted in a surface covered in circular surface domains. These domains were not observed following the incorporation of neat  $\text{C}_{16}\text{EO}_1$  or neat POM3 into Hydrothane films. Therefore, the coordination of  $\text{C}_{16}\text{EO}_1$  to POM3 caused a unique distribution behavior circular resulting in domains on the surface.

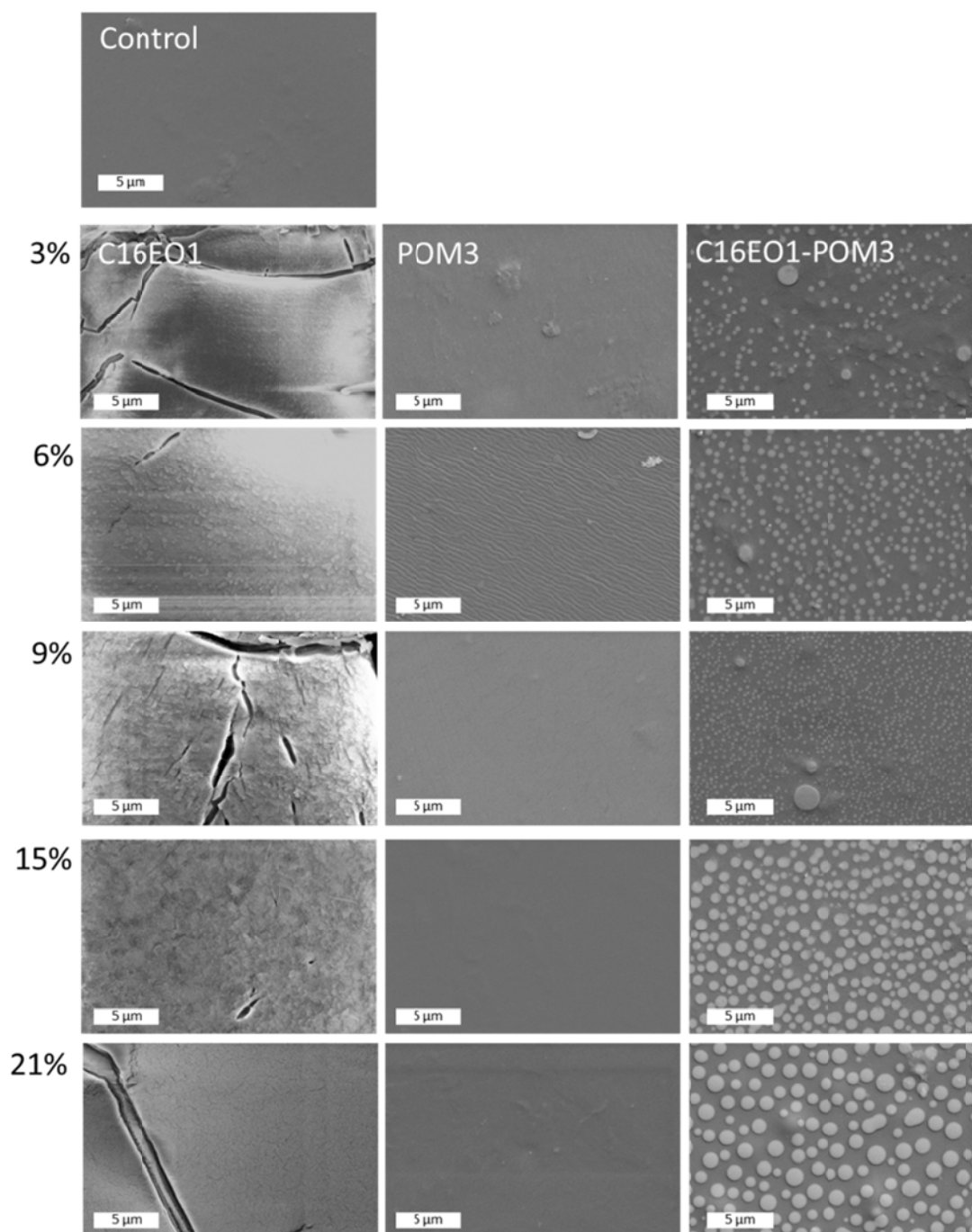


**Figure 3.2.** SEM micrographs of Hydrothane films loaded at increasing wt% concentration of C<sub>16</sub>EO<sub>1</sub> (left column), POM3 (center), and C<sub>16</sub>EO<sub>1</sub>-POM3.



The dimensions of the domains in Hydrothane films containing  $C_{16}EO_1$ -POM3 were also dependent on  $C_{16}EO_1$ -POM3 loading concentration. The diameters of the domains were plotted against loading concentration (Figure 3.3). A linear correlation was observed between loading concentration and average domain diameter. The observed relationship of increasing domain size with increasing  $C_{16}EO_1$ -POM3 concentrations suggests that the surface domains are composed of  $C_{16}EO_1$ -POM3.

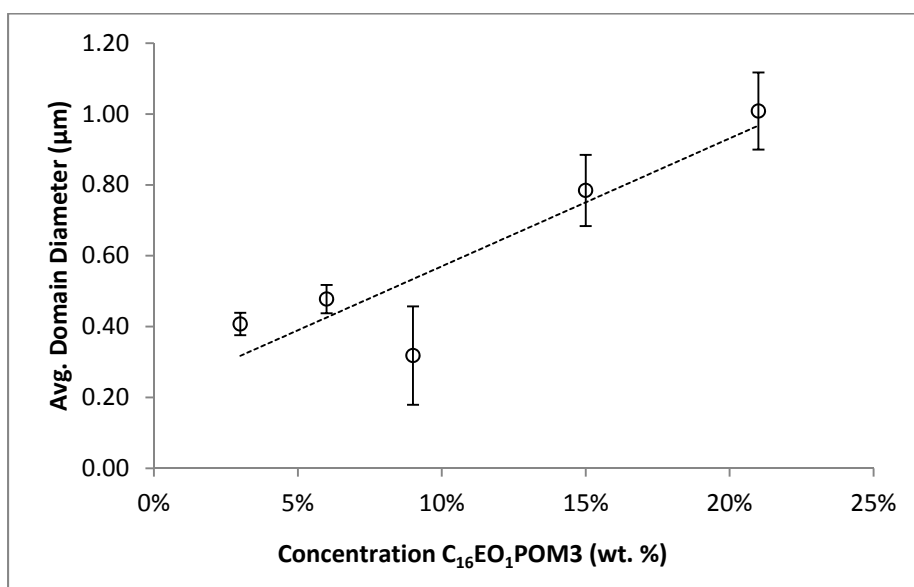


**Figure 3.3.** Average domain diameter vs. wt% loading of  $C_{16}EO_1$ POM3 in Hydrothane films.

An estimation of the physical dimensions of the surface domains were determined by comparing the measured domain diameters to loading. When the measured diameters were employed to calculate the area of a two dimensional circle, the increase in circular

area was found to scale approximately to the same degree as the increase in loading concentration (Figure 3.4). The 21 wt% loading was 7-fold greater loading than 3 wt%, and correspondingly, the calculated area of a circle from the diameter of the 21 wt% loading was 6.1-fold greater than the 3 wt%. In contrast, employment of the diameters in a calculation of volume for a sphere yielded ratios that were greater than the actual increase in loading concentration. Therefore, by this initial SEM analysis of C<sub>16</sub>EO<sub>1</sub>-POM3 in Hydrothane coatings, it has been determined that the coordination of QAS to POM resulted in unique flat disc shaped domains of additive in a polymer film, the diameters of which are dependent on the loading concentration.

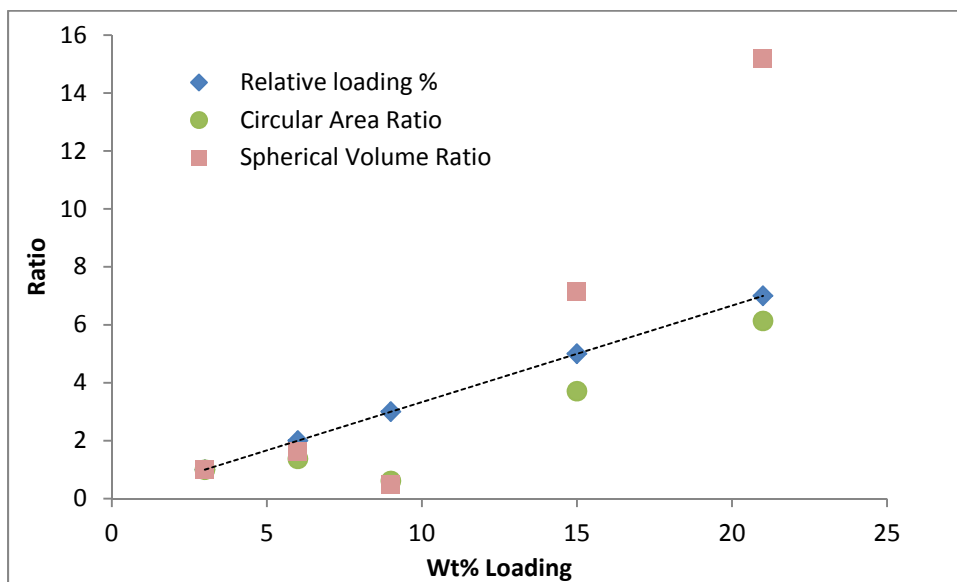


**Figure 3.4.** Loading wt% relative to 3 wt% loading compared to circular areas and spherical volumes calculated from domain diameters.

### **Effect of Drying Time on Domain Formation in Hydrothane**

Domain diameters were compared between 10 wt% C<sub>16</sub>EO<sub>1</sub>-POM3 Hydrothane polymer solutions cast under relatively slow (1 h), intermediate (30 min), and fast (5 min) solvent evaporation conditions. It was found that domain size increased with amount of time allowed for solvent evaporation (Figure 3.5). Two complimentary explanations likely explain these findings. The first is that increased evaporation time afforded the QAS in polymer solution to reach thermodynamic equilibrium. In the previous chapter, it was demonstrated that QAS-POM3 coordination occurs with the quaternary ammonium nitrogen and ethylene oxide units electrostatically bound in close proximity to the POM center and the longer alkyl tails away directed outwards. As such, C<sub>16</sub>EO<sub>1</sub>-POM3 effectively behaved as a hydrophobic molecule. Given a greater amount of time, minimization of QAS-POM and hydrophilic Hydrothane polymer interaction drove the QAS to accumulate into larger domains through diffusion through the polymer solution. This reduced the total contact area between C<sub>16</sub>EO<sub>1</sub>-POM3 and Hydrothane, which was a solvophobic (high energy) intermolecular interaction.

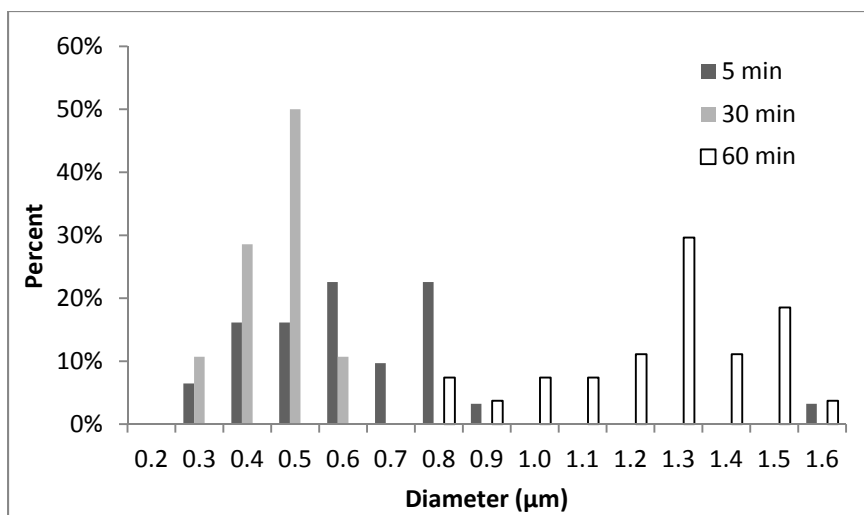


**Figure 3.5.** Histogram of domain diameters on 10 wt% C<sub>16</sub>EO<sub>1</sub>-POM3 Hydrothane films dried at various rates.

The second contributing factor to the increase in domain size as a function of decreased evaporation rates relates to the solvent vapor concentration directly above the cast polymer film. In order to reduce the evaporation rate, a glass Petri dish was inverted over the drying polymer. In addition to reducing the rate of evaporation, this also had the effect to increase the solvent vapor concentration in the atmosphere above the polymer and at the polymer-air interface compared to an uncovered film. Therefore, the polymer-air interface was effectively an interface between the hydrophilic Hydrothane and the organic, or hydrophobic, solvent saturated atmosphere. This facilitated the segregation of C<sub>16</sub>EO<sub>1</sub>-POM3 to the surface, in order to minimize the high energy interaction resulting from the solvophobic effect occurring between C<sub>16</sub>EO<sub>1</sub>-POM3 and Hydrothane and maximize the interaction between C<sub>16</sub>EO<sub>1</sub>-POM3 and air, which exhibits relatively high concentration of organic solvent. Overall, the increase in drying time demonstrated the

thermodynamic phase separation of C<sub>16</sub>EO<sub>1</sub>-POM3 into aggregates at the surface of a Hydrothane polymer solution.

In addition to C<sub>16</sub>EO<sub>1</sub>-POM3, a range of QAS-POM molecules of differing QAS composition were incorporated into Hydrothane to investigate the effect of QAS alkyl tail and ethoxy tail lengths on the distribution of additive in hydrophilic polyurethane. The selection of QAS-POMs comprised C<sub>8</sub>EO<sub>1</sub>POM3, C<sub>8</sub>EO<sub>2</sub>POM3, C<sub>8</sub>EO<sub>3</sub>POM3, C<sub>8</sub>EO<sub>4</sub>POM3, C<sub>10</sub>EO<sub>1</sub>POM3, C<sub>12</sub>EO<sub>1</sub>POM3, C<sub>12</sub>EO<sub>2</sub>POM3, C<sub>16</sub>EO<sub>1</sub>POM3, and C<sub>16</sub>EO<sub>2</sub>POM3.

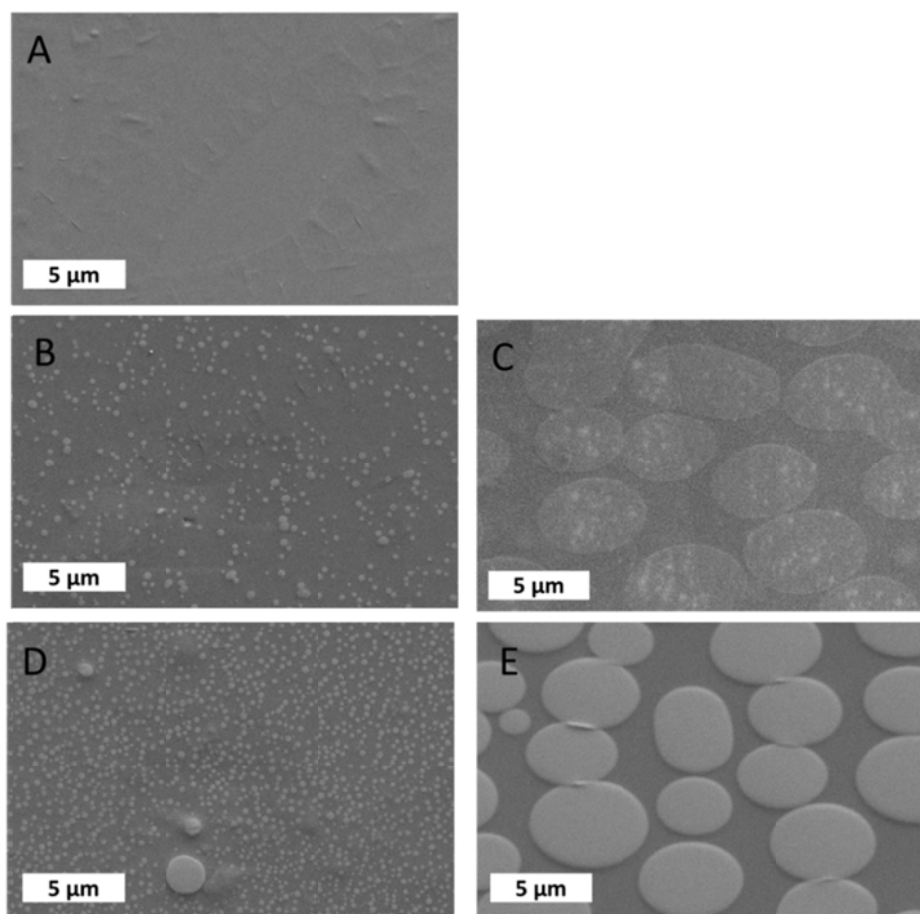


**Figure 3.6.** SEM micrographs of Hydrothane films loaded with 6 wt% of POM3 coordinated with A)  $C_{10}EO_1$ , B)  $C_{12}EO_1$ , C)  $C_{12}EO_2$ , D)  $C_{16}EO_1$ , and E)  $C_{16}EO_2$

The SEM micrographs in Figure 3.6 clearly demonstrated a strong effect of QAS composition on the distribution of QAS-POM3 in Hydrothane. An increase in alkyl tail length from 12 to 16 resulted in an increased quantity of surface domains for  $EO_1$ , yet the average domain diameter remained similar. Increase of the ethylene oxide tail length by a single unit, from  $C_{12}EO_1POM3$  to  $C_{12}EO_2POM3$  and from  $C_{16}EO_1POM3$  to  $C_{16}EO_2POM3$ , resulted in a significant increase in surface domain diameter. Therefore, both the alkyl and ethoxy tail lengths exhibited the ability to effect formation of surface

domains upon incorporation of QAS-POMs in Hydrothane. These data suggest polar-nonpolar repulsive interactions between the QAS-POM and Hydrothane polymer were causing the formation of surface domains since QAS-POM of alkyl tail length less than 12 carbons in length (more hydrophilic) did not result in domains. These shorter alkyl chain QAS-POMs were more hydrophilic, and thus more compatible with the Hydrophilic polymer matrix. Thus, an increase in nonpolar character from an increased alkyl tail length resulted in aggregation of QAS-POM out of the hydrophilic Hydrothane matrix and the formation of surface domains.

The effect of ethoxy tail length on surface domain formation was investigated further by the incorporation of mixtures at varying ratios of C<sub>16</sub>EO<sub>1</sub>POM3 and C<sub>16</sub>EO<sub>2</sub>POM3 into Hydrothane to total 10 wt% loading. A linear relationship between surface domain diameter and the ratio of C<sub>16</sub>EO<sub>2</sub>POM3:C<sub>16</sub>EO<sub>1</sub>POM3 was observed (Figure 3.7). T<sub>1</sub> relaxation experiments of the previous chapter demonstrated that the ethylene oxide tail was in close proximity, perhaps coordinated, to the POM center. Therefore, the hydrophilic ethylene oxide tail was not exposed to the surrounding solvent and polymer matrix. As such, lengthening of the ethylene oxide tail did not increase the hydrophilic character of the QAS-POM molecule, but did increase the molecular weight and physical dimensions of the QAS-POM which resulted in reduced solubility that facilitated the aggregation of QAS-POM out of the polymer matrix solution. The linear equation shown in Figure 3.7, in which  $x$  denotes the ratio of C<sub>16</sub>EO<sub>2</sub>POM3 to C<sub>16</sub>EO<sub>1</sub>POM3 and the variable  $y$  corresponds to the average domain diameter, can be employed to explain the relationship between domain diameter and relatively QAS-POM

loading. The line equation in Figure 3.7 can be used to estimate domain diameter when the ratio of C<sub>16</sub>EO<sub>2</sub>POM3 to C<sub>16</sub>EO<sub>1</sub>POM3 is known at a total loading concentration of 10 wt%. The linear relationship suggests an additive effect in which C<sub>16</sub>EO<sub>1</sub>POM and C<sub>16</sub>EO<sub>2</sub>POM equally contributed in the formation of each domain, as opposed to the separation of the two to form separate domains. Therefore, the QAS-POM3 species of different ethylene oxide tail lengths were compatible with each other and aggregated together to minimize additive-polymer interactions.

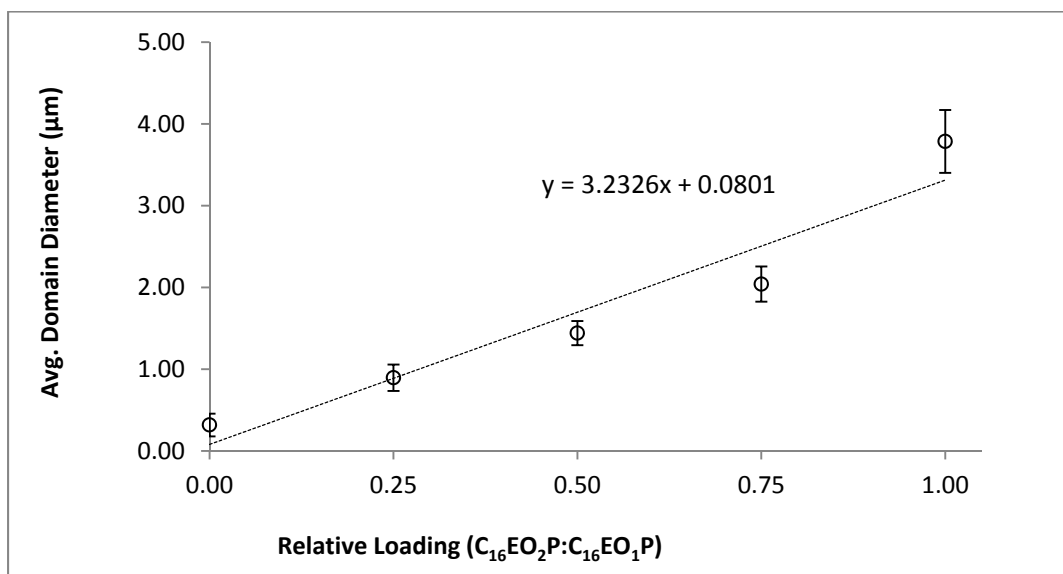


**Figure 3.7.** Effect of ratio of C<sub>16</sub>EO<sub>2</sub>P and C<sub>16</sub>EO<sub>1</sub>P on domain diameter when incorporated into Hydrothane films at a total loading concentration of 10 wt%.

### Surface Segregation of QAS-POM in Hydrothane

Energy dispersive spectroscopy (EDS) was utilized to investigate the elemental composition of the surface domains. Tungsten (W) was an element unique to the QAS-



POM species, which was utilized to discriminate QAS-POM from the polymer matrix in EDS analysis. Overlays of W signal (purple dots) with SEM micrographs of Hydrothane films containing mixtures of  $C_{16}EO_1POM:C_{16}EO_2POM$  are shown in Figure 3.8. A greater concentration of W signal was observed to overlay with the surface domains in the SEM micrograph than in the area of the Hydrothane polymer. This indicated that, indeed, the surface domains contain W and were composed of concentrated QAS-POM.

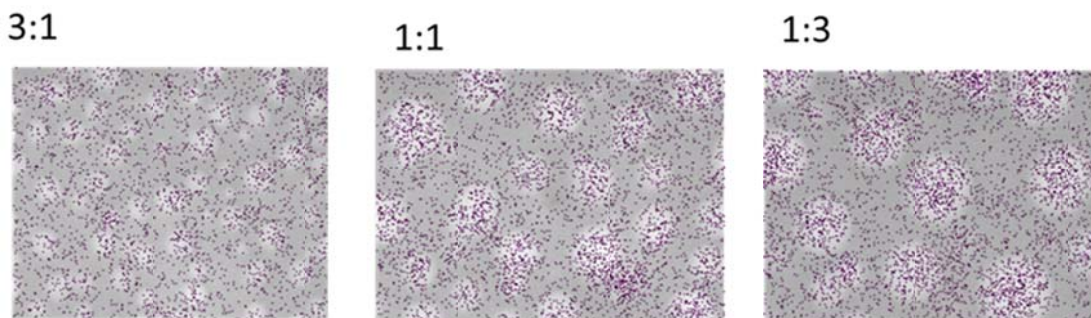


**Figure 3.8.** EDS mapping mode of W signal (purple) overlaid onto SEM micrograph of mixtures of  $C_{16}EO_1POM:C_{16}EO_2POM$ .

XPS analysis afforded chemical composition of to a depth of approximately 10 nm of the surface. The element W and the ion  $N^+$  were unique to the QAS-POM species and therefore were utilized in XPS analysis to determine the presence of QAS-POM at the surface. Figure 3.9 presents the W 4f<sub>7/2</sub>, 4f<sub>5/2</sub>, and 5p<sub>3/2</sub> XPS signals from each Hydrothane film loaded with QAS-POM at 10 wt%. The control and  $C_8EO_2POM_3$  Hydrothane films did not exhibit a W 4f signal which denoted an absence of QAS-POM at the surface. XPS analysis of Hydrothane films containing  $C_{12}EO_1POM$ ,  $C_{16}EO_1POM$ ,

and C<sub>16</sub>EO<sub>2</sub>POM indicated a progressive increase in W surface concentration. This result corresponded with the increase in size of surface domains that were observed with SEM.

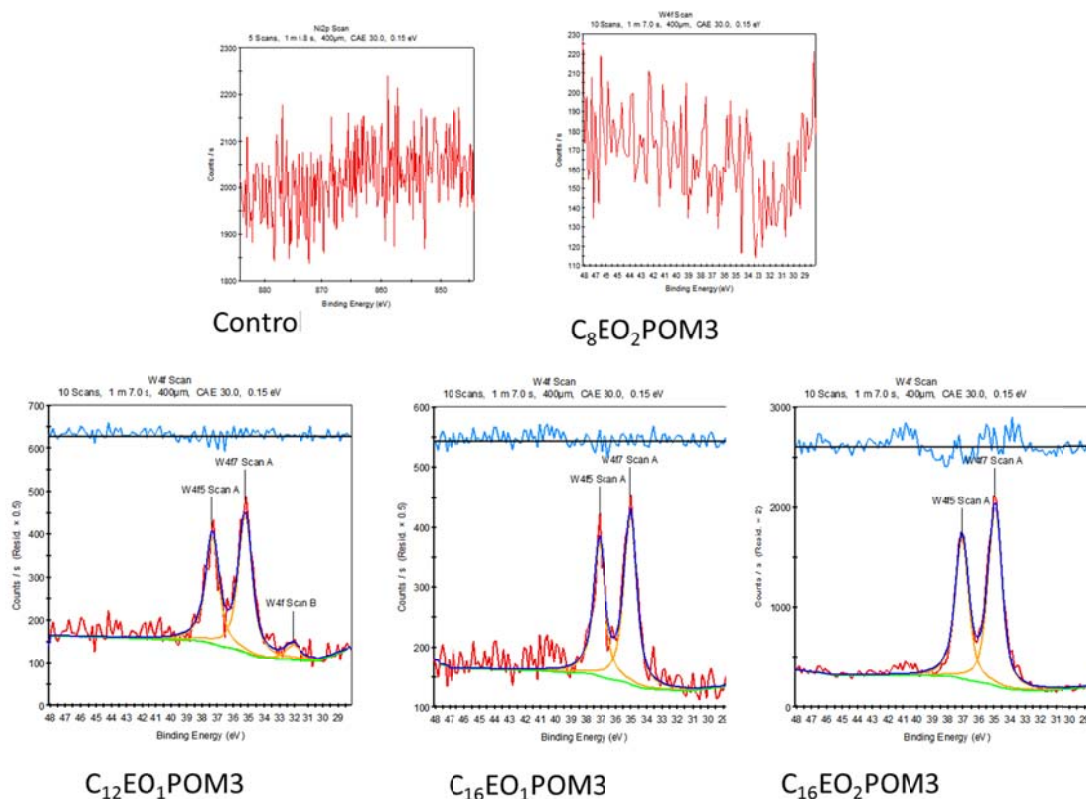


**Figure 3.9.** XPS W 4f signal from Hydrothane films loaded at 6 wt% QAS-POM3

XPS analysis coupled with electron gun sputtering resulted in the ability to probe and compare the chemical composition of the polymer film surface and bulk. As the QAS-POM additives were designed to be amphiphilic, it was expected that the additives segregate and concentrate at the polymer-air interface, or surface, of the film as opposed to buried within the bulk. Nitrogen 1s signal was measured at the surface and after a 10 s electron beam sputter which ablated away surface and allowed the bulk of the polymer to

be investigated (Figure 3.10). Surface segregation was indicated by the presence of a peak for  $N^+$  (402 eV) at the surface, which was absent in the bulk. The combination of lateral resolution provided by EDS analysis and the chemical depth profiling provided by XPS has elucidated that the circular domains were composed of QAS-POM and only present at the surface of the polymer.

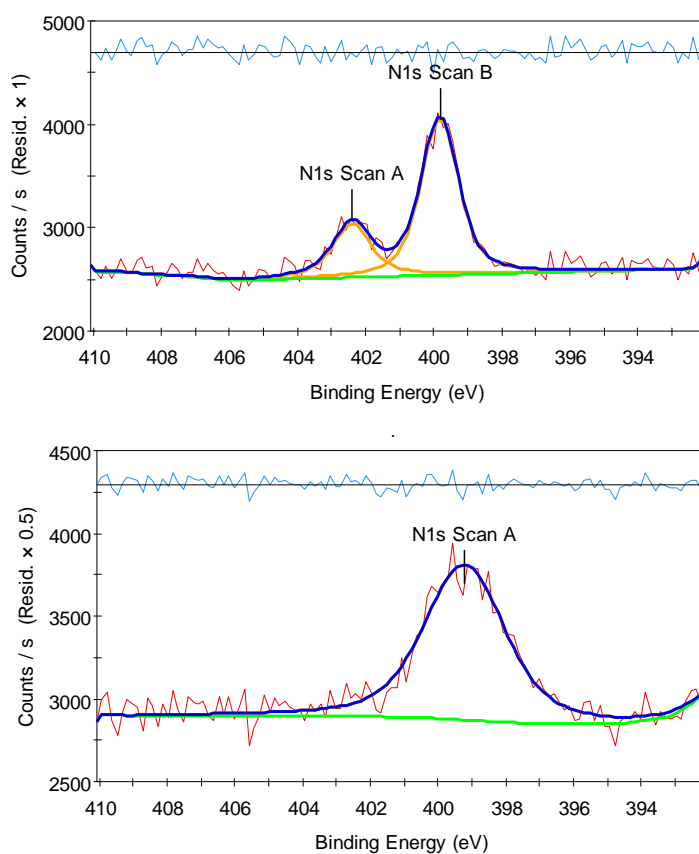


**Figure 3.10.** XPS nitrogen elemental scan of surface (top) and bulk (bottom) of 6 wt%  $C_{16}EO_1POM$  Hydrothane film.

### 3.3.2. QAS-POM Distribution in Tecoflex

The series of QAS-POMs were incorporated into the commercial polymer Tecoflex in order to investigate the behavior of the additives in a more hydrophobic polymer matrix than Hydrothane. In addition to the QAS-POMs, neat C<sub>16</sub>EO<sub>1</sub> and neat POM3 were each formulated into separate Tecoflex films at comparable wt% loadings for comparison. Additives were loaded at 10 wt% in Tecoflex for initial measurement of water contact angle of the Tecoflex film surfaces (Figure 3.11). Incorporation of QAS-POMs was found to generally result in a contact angle approximately 10° greater than the control. However, loading of C<sub>16</sub>EO<sub>2</sub>-POM deviated from the trend by resulting in a water contact angle 10° less than that of the control. Furthermore, incorporation of neat C<sub>16</sub>EO<sub>1</sub> resulted in a contact angle 60° less than the control, while POM3 incorporation had no effect. It is worth noting that comparison between Tecoflex and Hydrothane could not be performed since water contact angle was not measured for Hydrothane films as Hydrothane absorbs water, thus invalidating any water contact angle measurement.

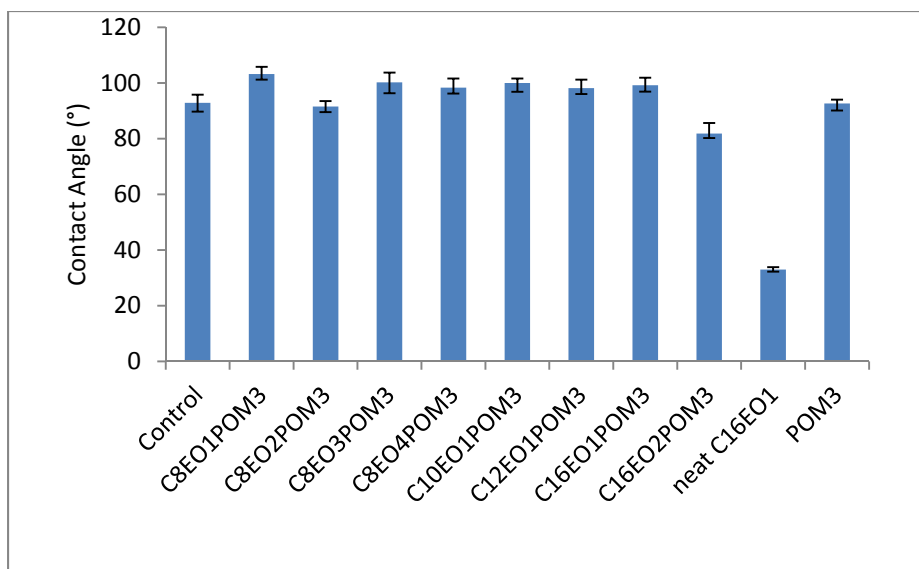


**Figure 3.11.** Contact angle of Tecoflex films containing QAS-POM3s loaded at 10 wt%.

SEM was utilized for further investigation of Tecoflex films containing QAS-POMs (Figure 3.12). Similar to Hydrothane, loadings of QAS-POMs with carbon tail lengths of 8 did not result in any observed surface features. However, in Tecoflex, surface features were only observed upon loading of QAS-POMs of the longest alkyl tail lengths, C<sub>12</sub> and C<sub>16</sub>. Furthermore, C<sub>16</sub>EO<sub>2</sub>POM resulted in surface domains of 4.10  $\mu\text{m}$  average diameter whereas C<sub>16</sub>EO<sub>1</sub>POM3 exhibited primarily 1.15  $\mu\text{m}$  diameter surface domains in Tecoflex. A similar trend was observed on the surfaces of Tecoflex films loaded with C<sub>12</sub>EO<sub>1</sub>POM and C<sub>12</sub>EO<sub>2</sub>POM. Increase in the length of ethylene oxide tail length from EO<sub>1</sub> to EO<sub>2</sub> resulted in significantly greater domain diameters. A similar result was observed in Hydrothane films loaded with QAS-POM additives.

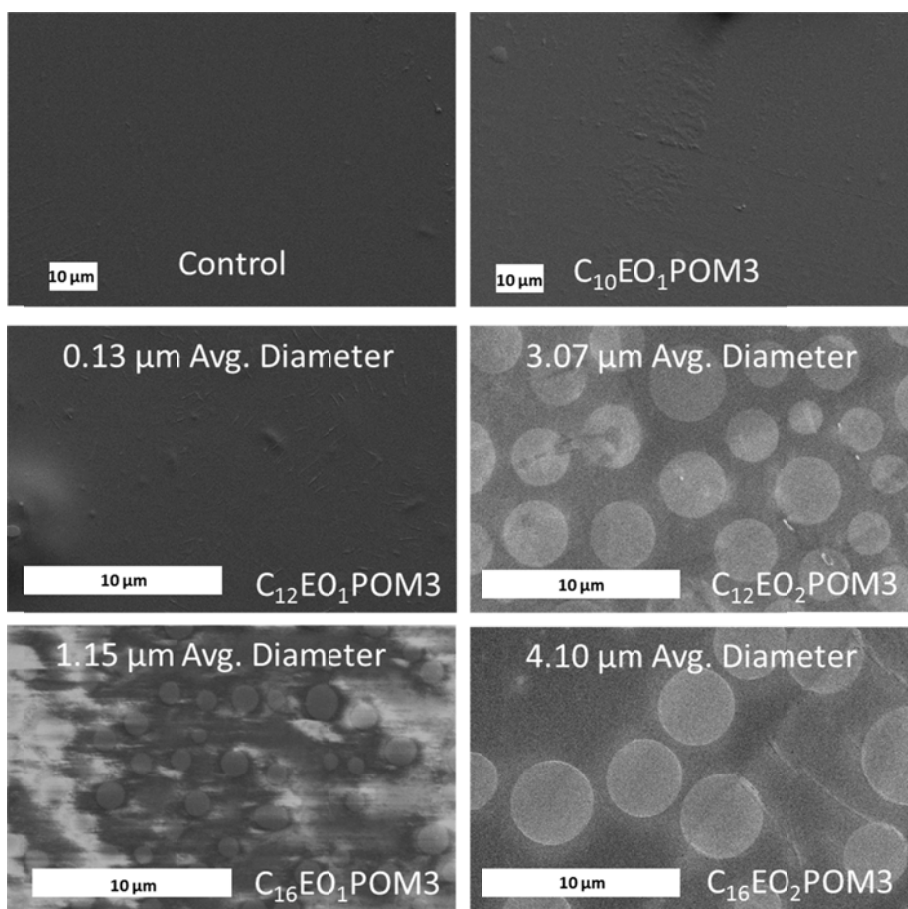


**Figure 3.12.** SEM images of Tecoflex films loaded at 10 wt% QASPOM3.

### **Effect of QAS-POM Concentration on Domain Formation in Tecoflex**

The unique behavior exhibited by  $C_{16}EO_2POM3$  in Tecoflex at 10 wt% prompted a more detailed investigation by its loading at additional 5, 15, and 20 wt% concentrations. Initial ATR-IR analysis of the films were performed, the spectra of which are shown in Figure 3.13. Increasing concentration of  $C_{16}EO_2POM$  in Tecoflex resulted in increased absorbance intensity from the W-O vibrational modes at 979, 931, and 900  $cm^{-1}$ . These data provide confirmation of  $C_{16}EO_2$ -POM incorporation into Tecoflex at increasing wt% loading concentrations.

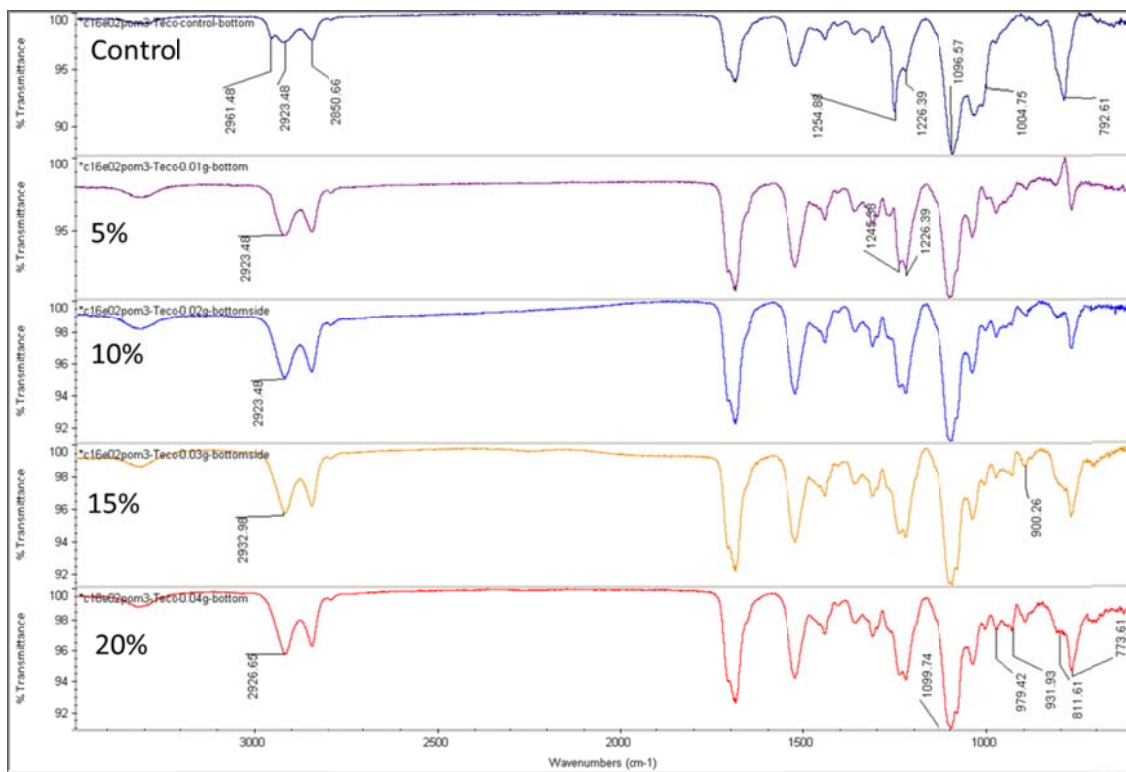


**Figure 3.13.** ATR-IR Spectra of Tecoflex films loaded with C<sub>16</sub>EO<sub>2</sub>-POM3.

TGA analysis and water contact angle for C<sub>16</sub>EO<sub>2</sub>-POM3 Tecoflex films are presented in Table 3.1. The mass percent remaining of the Tecoflex films after the completion of the TGA temperature ramp to 600 °C confirmed to the actual loading wt% of C<sub>16</sub>EO<sub>2</sub>-POM. Since approximately 40 % of the molecular weight of the C<sub>16</sub>EO<sub>2</sub>-POM was composed of thermally unstable C<sub>16</sub>EO<sub>2</sub>, only the temperature stable POM core remained at high temperatures, resulting in an ultimate mass percent remaining of Tecoflex films of approximately half of the loading concentration.

**Table 3.1.** TGA analysis of Tecoflex loaded with increasing concentration of C<sub>16</sub>EO<sub>2</sub>-POM3.

	<b>Final Mass (%)*</b>	<b>Water contact (°)</b>
Control Tecoflex	0.624	92.18
5 % C <sub>16</sub> EO <sub>2</sub> -POM3 Tecoflex	3.644	87.25
10 % C <sub>16</sub> EO <sub>2</sub> -POM3 Tecoflex	5.928	87.70
15 % C <sub>16</sub> EO <sub>2</sub> -POM3 Tecoflex	8.041	88.35
20 % C <sub>16</sub> EO <sub>2</sub> -POM3 Tecoflex	9.233	85.15

\*At 600 °C

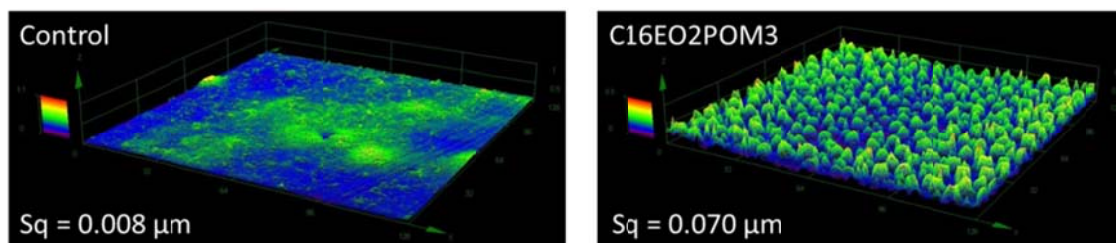
The interface of a solid, as well as a liquid, is unique from the interior bulk, resulting in a higher energy at the interface, or surface, than in the bulk. The process to determine surface energy is relatively simple for liquids, as a liquid's surface energy has implications in boiling point, which is evident by the high boiling point for water considering its molecular weight. Furthermore, surface tension of a liquid can be determined by capillary force experiments and asymmetric drop shape analysis.<sup>141</sup> However, determination of the surface energy of solid surface presents more difficulty, yet is critically important for understanding how a material will interact within a given environment.

A well-established method for determining surface energy of a solid involves measurement of the angle created at the edge of liquid droplet resting on a solid surface. Specifically, the angle is measured at the triple line where solid, liquid, and gas phases interact. Each phase has both cohesive and repulsive forces acting between the molecules of which it is composed. The surface tension of an individual phase is a function of those



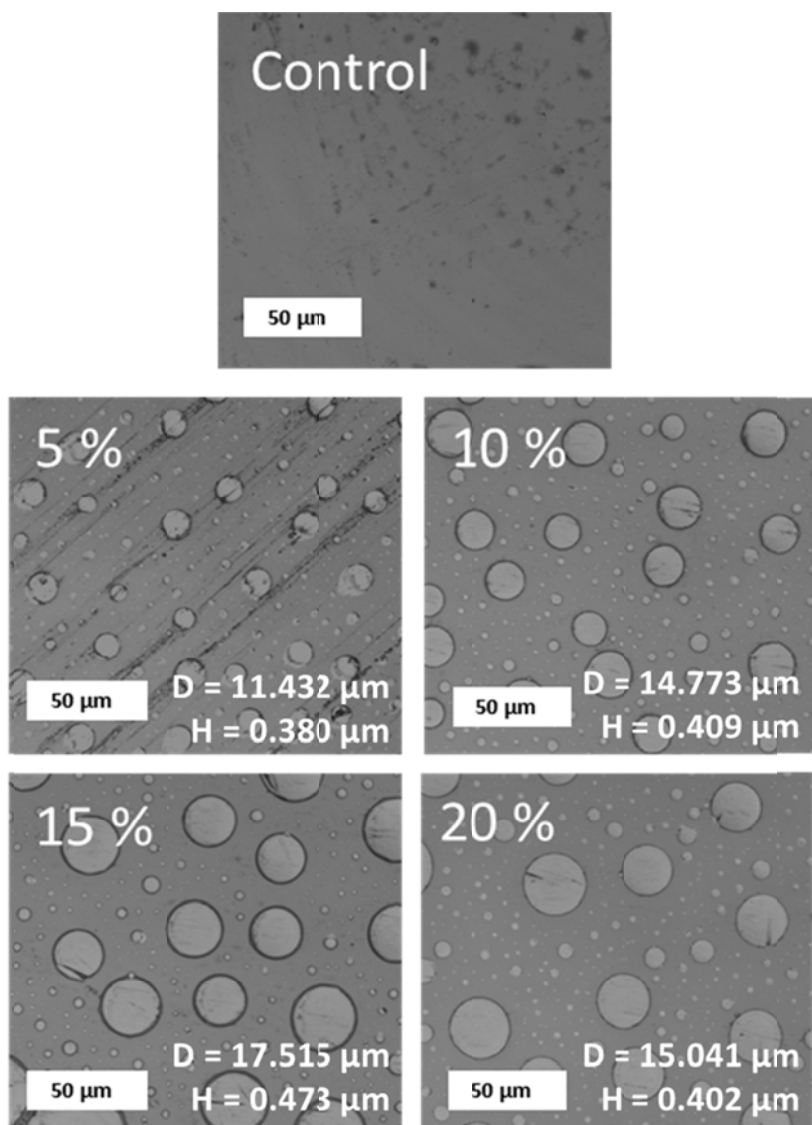
forces. The angle formed represents equilibrium of the cumulative interactions of all intermolecular forces within and between each phase.<sup>142</sup> Additionally, cohesive and repulsive interactions occur between separate phases at every interface. In the three phase system described above, a phase with unknown surface tensions can be determined by its interaction with phases with known surface tensions.<sup>143–145</sup> Determination of surface energy via liquid contact angle measurements is based on such concepts.

Table 3.1 presents water contact angles that were measured on Tecoflex films containing increasing concentration of C<sub>16</sub>EO<sub>2</sub>-POM. Water contact angle decreased with increasing C<sub>16</sub>EO<sub>2</sub>-POM loading concentration. This result indicated that increased concentration of C<sub>16</sub>EO<sub>2</sub>-POM increased the hydrophilicity of the polymer surface, despite the previous conclusions which demonstrated that the QAS-POMs exhibited hydrophobic exteriors and were located at the surface of Hydrothane films. However, water contact angle is dependent on both solid surface tension and surface roughness. Furthermore, it has been demonstrated that for a surface with a water contact angle around 90°, increased surface roughness will decrease the water contact angle.<sup>146</sup> Therefore, the decrease in contact angle was likely due to imparted surface roughness of C<sub>16</sub>EO<sub>2</sub>-POM3. Indeed, the increased surface roughness of Tecoflex containing C<sub>16</sub>EO<sub>2</sub>-POM3 compared to control Tecoflex film was confirmed by three-dimensional confocal laser microscopy (Figure 3.14).



**Figure 3.14.** 3D Confocal microscopy images of control Tecoflex (left) and 10 wt% C<sub>16</sub>EO<sub>2</sub>-POM Tecoflex. Note the image dimensions in the z-axis are magnified 25X in order to highlight roughness.

Confocal microscopy was utilized further to compare the surface domain dimensions (diameter and height) of Tecoflex films loaded at various concentrations of C<sub>16</sub>EO<sub>2</sub>-POM (Figure 3.15). The average diameters and heights of surface domains increased with increasing loading of C<sub>16</sub>EO<sub>2</sub>-POM in Tecoflex films up to 15 wt% loading. The ratio of height to diameter decreased with increasing concentration. The height of the surface domains did not increase with increasing loading concentration, while the surface domain diameters increased. The fact that the height of surface domains did not increase proportionally with diameter supports the previous assertion that the three dimensional shape of the surface domains resemble that of a flattened disc, as opposed to spherical.



**Figure 3.15.** Laser confocal microscope images of  $C_{16}EO_2$ -POM3 loaded Tecoflex including surface domain dimensions, diameter (D) and height (H).

In addition to surface domain height, confocal microscopy afforded the ability to measure the depth of the surface domains. This was accomplished by the application and removal of an adhesive strip on the surface, which was found to also remove portions of the surface domains. The surface was then analyzed with laser confocal microscopy and

the depths of the areas where the surface domain had resided were measured (Figure 3.16a). The surface domains were found to exhibit an average depth to diameter ratio of 0.05. It was demonstrated previously that the height to diameter ratio was approximately 0.03. Therefore, the surface domains projected into the polymer film more than they protruded above its surface. This allowed for the estimation of a cross sectional dimension of the average surface domains (Figure 3.16b). Clearly, the domains were flattened disc shaped as was predicted previously by the calculation of increase in diameter with increasing loading concentration. Additionally, the fact that an adhesive strip was able to remove the surface domains intact from the polymer surface demonstrated that the surface domains were separate from the polymer bulk.

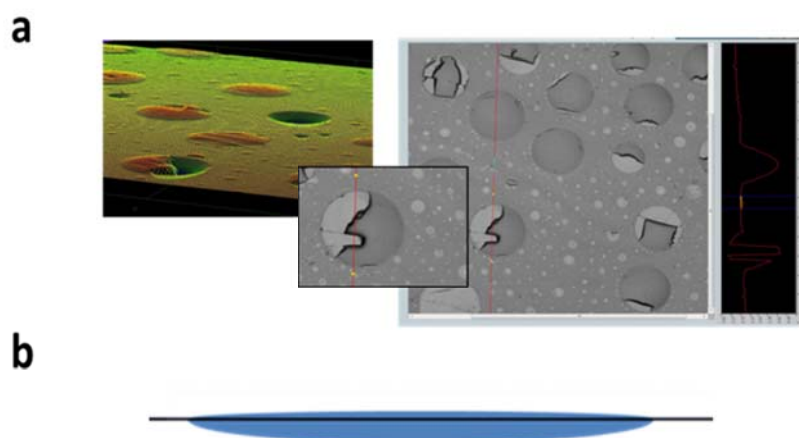


**Figure 3.16.** a) Example of confocal microscope image of  $C_{16}EO_2$ -POM3 Tecoflex film after adhesive removal and b) proposed dimensions of an average surface domain.

### **Effect of Film Drying Time on Domain Formation in Tecoflex**

The effect of solvent evaporation rate on the distribution of additive in Tecoflex was investigated between fast (5 min), intermediate (30 min), and slow (1 h) drying times, just as in Hydrothane. However, C<sub>16</sub>EO<sub>2</sub>-POM3 was employed for Tecoflex instead of C<sub>16</sub>EO<sub>1</sub>-POM3 which was investigated in Hydrothane. The diameters of surface domains from incorporation of C<sub>16</sub>EO<sub>2</sub>-POM3 into Tecoflex decreased with increasing drying time (Figure 3.17). Therefore, the mixture and dispersion of C<sub>16</sub>EO<sub>2</sub>-POM3 into the Tecoflex film increased when afforded more time, in direct contradiction to the behavior that was observed of C<sub>16</sub>EO<sub>1</sub>-POM3 in Hydrothane. As stated earlier, increased time for evaporation allows the additive and polymer to achieve thermodynamic equilibrium. Surface domain morphology at thermodynamic equilibrium of QAS-POM in Tecoflex was opposite to that observed in Hydrothane. Therefore, equilibrium of additive was determined by the chemical composition (hydrophilicity) of the polymer. In the previous chapter it was demonstrated that the exterior of the QAS-POM conjugate was effectively composed of alkyl moieties, and resulting from such increased drying time afforded minimization of interfacial energy which resulted in the dispersion of QAS-POM in hydrophobic Tecoflex matrix. Therefore, intermolecular interactions between Tecoflex polymer and C<sub>16</sub>EO<sub>2</sub>-POM3 were of lower energy and thus favored at room temperature compared to the intermolecular additive-additive interactions between C<sub>16</sub>EO<sub>2</sub>-POM3 molecules. In contrast, the intermolecular additive-additive interactions were favored over polymer-additive interactions in Hydrothane, a hydrophilic polymer.

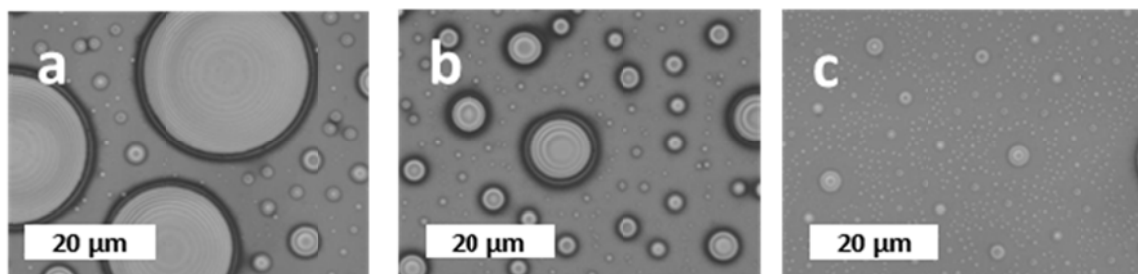


**Figure 3.17.** Microscope images of Tecfolex surfaces containing  $C_{16}EO_2$ -POM after a) fast, b) intermediate, and c) slow solvent evaporation rates.

ATR-IR was employed to investigate the surface segregation behavior of QAS-POM additives in Tecoflex polymers. Comparative analyses of the top and bottom surfaces of a Tecoflex film containing 10 wt%  $C_{16}EO_2$ POM were performed to investigate vertical distribution of the additive (Figure 3.18). The IR spectrum of the top surface of the film exhibited vibrational absorbances corresponding to the tungsten oxide-POM and the ether stretching of the ethylene oxide tail. The IR absorbances unique to  $C_{16}EO_2$ -POM were not observed in the ATR-IR spectrum of the bottom of the film. These data demonstrated a concentration of  $C_{16}EO_2$ POM only at the top surface, which suggests that the QAS-POM additive automatically segregated to the surface of the film upon drying.

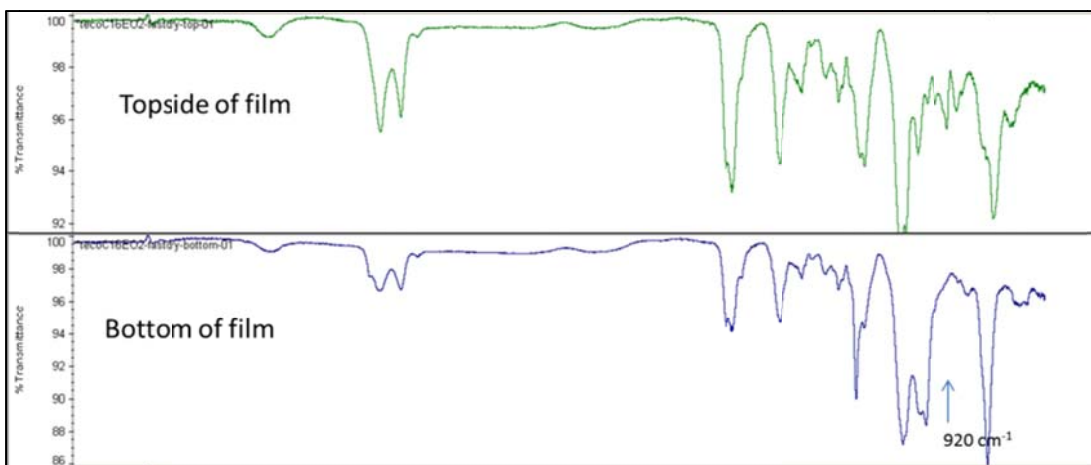


**Figure 3.18.** ATR-IR comparison of the top and bottom of 10 wt% C<sub>16</sub>EO<sub>2</sub>-POM Tecoflex film.

XPS analysis of N 1s signal and sputter depth profile were performed on Tecoflex films containing 10 wt% C<sub>16</sub>EO<sub>2</sub>POM to further investigate surface segregation. The quaternary ammonium nitrogen peak (402 eV) that was observed at the top surface (Figure 3.19a) was absent in the bulk (Figure 3.19b). Additionally, the quaternary ammonium nitrogen signal was absent in XPS analysis of the bottom of the film, including depth sputter profiling (Figure 3.19c & d, respectively). These results that indicated the presence of QAS-POM only at the top surface of Tecoflex film, in combination with the ATR-IR comparative analysis, provided evidence of surface segregation.

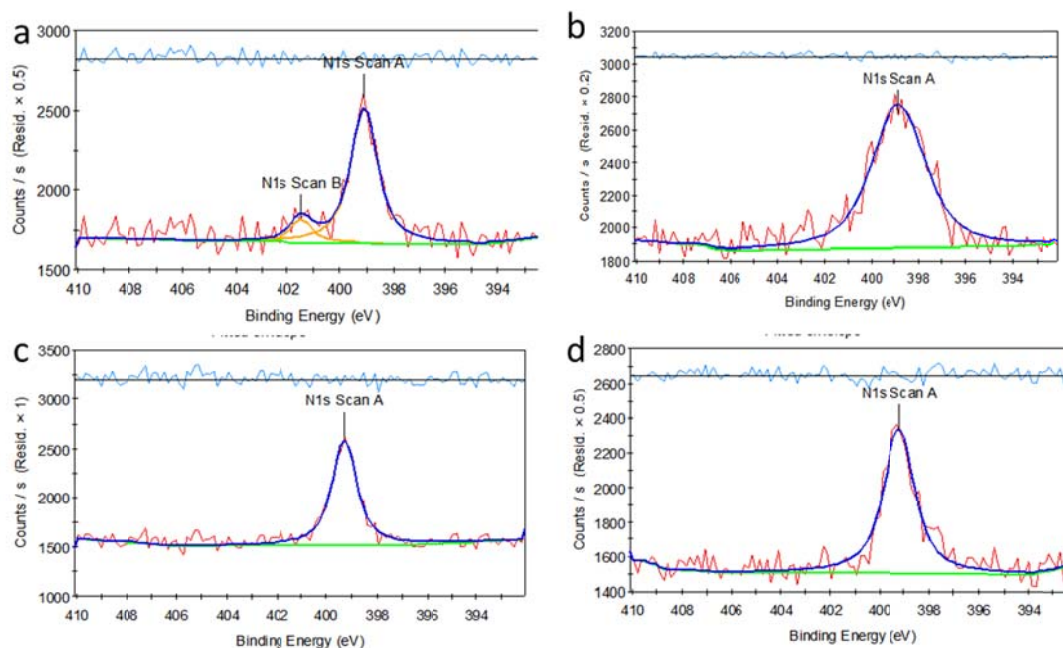


**Figure 3.19.** XPS nitrogen 1s signal of 10 wt% C<sub>16</sub>EO<sub>2</sub>POM in Tecoflex a) top surface, b) sputtered top bulk, c) bottom surface, and d) sputtered bottom bulk.

### 3.3.3. Antimicrobial Activity of Films Containing QAS-POMs

Due to the fact that QAS exhibit antimicrobial activity, Hydrothane and Tecoflex films containing QAS-POM additives were subjected to antimicrobial challenges. Figure 3.20 presents the efficacy of film surfaces against challenges of *S. aureus* (Gram +) and *E. coli* (Gram -). Hydrothane films loaded with C<sub>16</sub>EO<sub>1</sub>POM did not exhibit statistically significant reduction of bacteria at QAS-POM loading levels less than 15 wt%. Furthermore, the 15 and 21 wt% C<sub>16</sub>EO<sub>1</sub>POM coatings exhibited 6 log reduction of *S. aureus* and minor 1-2 log reduction of *E. coli*. These results afforded insights into the coordination of QAS to POM, which supplemented investigations performed in the previous chapter.



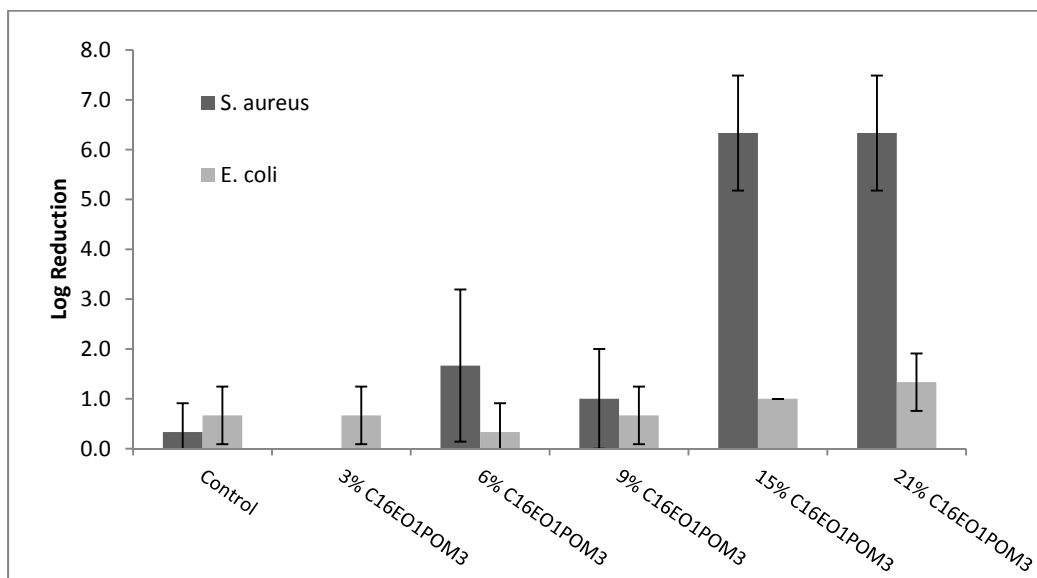


**Figure 3.20.** Antimicrobial activity of Hydrothane films loaded at increasing concentration of C<sub>16</sub>EO<sub>1</sub>POM<sub>3</sub>.

Tecoflex films containing QAS-POM additives at 10 wt% loading exhibited similar antimicrobial activity as the Hydrothane films of comparable loading. In addition to the QAS-POMs, neat C<sub>16</sub>EO<sub>1</sub> and neat POM were incorporated into Tecoflex for comparison. As expected, Tecoflex films containing neat C<sub>16</sub>EO<sub>1</sub> exhibited potent antimicrobial activity against both Gram-positive and Gram-negative bacteria, while incorporation of POM<sub>3</sub> imparted insignificant activity.

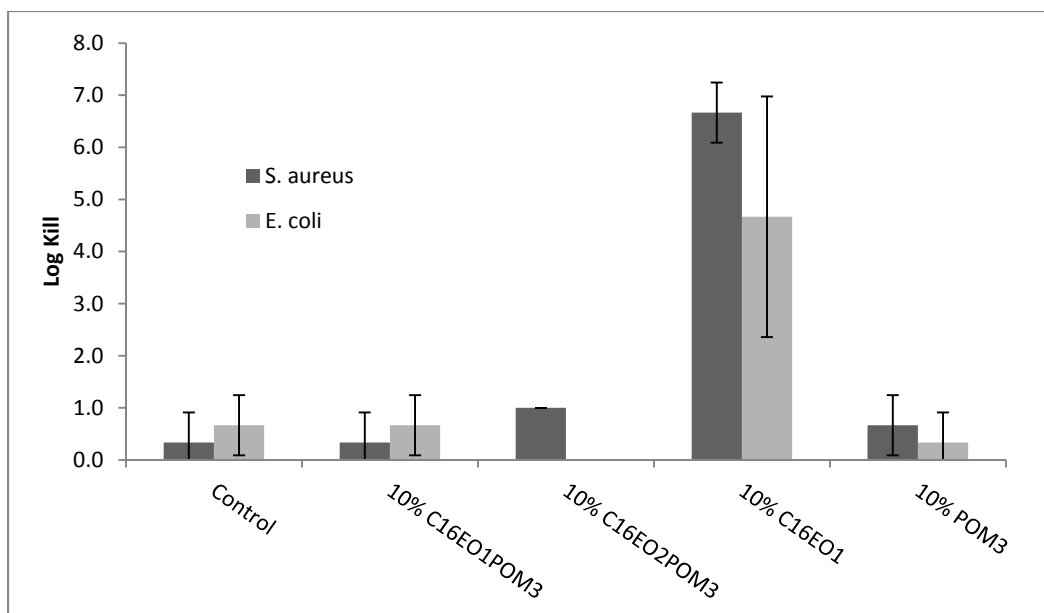


**Figure 3.21.** Antimicrobial activity of Tecoflex films loaded with a range of additives.

The lack of significant antimicrobial activity of films containing QAS-POMs at loadings less than 10 wt% confirmed the previous assertion that the quaternary ammonium nitrogen atom was coordinated in close proximity to the POM counter anion. One mechanism explaining the antimicrobial activity of QAS is that the quaternary ammonium ion facilitated ionic disruption and lysis of the bacterial cell membrane.<sup>147</sup> Therefore, coordination of the ammonium ion of the QAS to the POM core effectively shielded biocidal interaction with bacteria, thus reducing antimicrobial activity.

### 3.4. Summary

The data presented herein presented clear evidence of phase segregation of QAS-POM in polyurethane matrices. Recent publications have succinctly summarized the numerous models and theories of phase segregation.<sup>135,148</sup> The additive, QAS-POM, exhibited hydrophobic alkyl tail exteriors, which resulted in a relatively hydrophobic

molecule. A series of QAS-POM were synthesized; however, as the coordination of QAS to POM effectively buried the polar moieties (ammonium and ethylene oxide tail) the variability in QAS composition had a primary effect to increase particle size and resultant solubility. An increase in particle size contributed to decreased particle solubility, therefore resulted in larger surface diameters.

The hydrophilic character of polyurethane was found to play a significant role in the distribution of additive. A decrease in solvent evaporation rate of QAS-POM in Tecoflex films resulted in greater additive dispersion instead of aggregation that was observed in Hydrothane. Furthermore, QAS-POM aggregated into surface domains of smaller diameter in Tecoflex than in Hydrothane of comparable wt% loadings. These results indicated that intermolecular interactions between additive and polymer were the most significant factors in the additive distribution for this system.

Since it was demonstrated by XPS sputter depth analysis that the QAS-POM additives were primarily present at the surface, it was proposed that during film drying that the additives separated from the bulk polymer solution and segregated to the polymer solution-air interface forming a surface layer. The aggregation of the additives occurred in order to reduce surface tension resulting from increased additive concentration at the surface during drying. This proposed mechanism of additive dispersion in Hydrothane corresponds to the observed increase in surface domain diameter that resulted from decreased solvent evaporation rate. The additive, QAS-POM, exhibited a core-shell structure in which hydrophobic alkyl tail exteriors were exposed, which resulted in a relatively hydrophobic molecule. Therefore, the surface segregation of QAS-POMs in

polyurethane solutions was not surfactant driven, but driven by solvophobic interactions between additive and polymer.

Overall, QAS-POM additives exhibited distribution behavior in polyurethane matrices that was dependent on the alkyl tail length of QAS, ethoxy tail length of QAS, concentration of QAS-POM in polymer solution, relative concentration of QAS-POM in polymer solution, the hydrophilic character of the polymer, the concentration of polymer solution, and the amount of time required for the polymer solution to dry into a film. Incorporation of QAS-POM into polymer solutions and cast into films resulted in the formation of surface domains on the surface of the polymer film. XPS analyses confidently demonstrated that these occur only at the surface of the film and were not distributed throughout the bulk of the polymer, thus suggesting surface segregation. The research presented here contributes a greater understanding of the distribution of QAS encapsulated POMs in polyurethane coatings.

### **3.5. Experimental Methods**

#### **Materials**

All solvents were reagent grade and used without additional purification. Purchased starting materials were used without further purification.

#### **Synthesis of QAS-POM conjugates**

The quaternary ammonium salt utilized in this study was synthesized following a previously reported procedure.<sup>49</sup> Nickel containing polyoxometalates (POM3) were

synthesized by the application of procedures modified from two previous reports.<sup>100,128</sup> Their full characterizations were reported in the previous chapter.

### **Film preparation**

Films were prepared by dissolving 5 g of Hydrothane (Cardiotech LTD, UK) in 50 mL of chloroform with a Teflon stir bar over 24 h to ensure complete dissolution. Hydrothane is a commercial polyurethane that exhibits improved purity relative to comparable resin systems. To a scintillation vial containing QAS-POM3, 2 mL of Hydrothane solution was added and vortexed until additive was completely dissolved in the solution. The solution was then solvent caste into an aluminum pan covered with a weigh boat and allowed to dry.

Effect of solvent evaporation rate was evaluated by comparing three identical polymer solution formulations drying under different conditions: uncovered, partially covered with a plastic weight boat, and completely covered by a glass Petri dish lid. These three conditions correspond to respective drying times of 5, 30, and 60 minutes.

### **Contact angle**

Surface contact angle measurements were performed using a VCA Optima video contact angle system by AST Products, Inc. (Billerica, MA) employing the sessile drop technique. Three replicate measurements were made of 4  $\mu$ L of triple distilled water at 20 °C.

### **Laser Confocal Microscopy**

Surface texture, morphology, and roughness were investigated employing an Olympus Lext 3D measuring laser microscope OLS 4000. 128  $\mu\text{m}$  x 128  $\mu\text{m}$  images were acquired at 2012x magnification with z-axis steps of 60 nm. Root mean square height surface roughness (Sq) was calculated by OLS software employing an 80  $\mu\text{m}$  cutoff filter.

### **SEM**

Prior to SEM analysis, the Hydrothane<sup>TM</sup> samples were coated with a 5 nm layer of gold using a Cressington 108 auto sputter coater equipped with a Cressington MTM-20 thickness controller. A Carl Zeiss SMT Supra55 scanning electron microscope (SEM) was utilized to analyze morphology of the prepared films. Accelerating voltage was set between 3 and 5 kV. Dimensions of surface features were measured using Image J analysis software calibrated to the image scale bar.

### **XPS analysis**

XPS analysis was performed using a Thermo Scientific K-Alpha XPS spectrometer. A 400  $\mu\text{m}$  spot size was analyzed with the flood gun on for each. For each sample, a low resolution survey was performed with a pass energy of 200 eV and step size of 1.0 eV. High resolution region scans were performed for all samples, each with a pass energy of 30 eV and a step size of 0.15 eV. XPS emission angle was 54.7°. XPS depth profiling was performed with a 3000 eV ion gun set to low current. An ion sputter

cycle of 10 sec was performed, followed by survey and elemental scans. High resolution region scans during depth profiling were performed in multichannel snapshot mode employing a 150 eV pass energy, 10 frames, 1 sec/frame, over 128 channels. Peak fitting was performed with Advantage computer software, specifically smart fitting algorithm.

### **Energy dispersive X-ray spectroscopy (EDS)**

A Carl Zeiss SMT Supra55 SEM equipped with energy dispersive X-ray detector with an accelerating voltage set to 10 KeV was utilized to perform EDS. Data was collected and analyzed on Spirit Software.

### **ATR-IR**

Attenuated total reflectance infrared (ATR-IR) spectra were measured utilizing a Nicolet 6700 FT-IR with ATR attachment equipped with a Ge crystal from Thermo Scientific (Waltham, MA). 64 scans were compiled for each spectrum.

### **Thermal Analysis**

A TA Instruments Q50 TGA was utilized to perform thermogravimetric analysis at a heating rate of 10 °C/min under nitrogen from room temperature to 600 °C.

### **Anti-microbial testing**

*Staphylococcus aureus* (*S. aureus*, ATCC 25923) was utilized in bacterial challenges for the polymer films. Bacteria were grown at 37 °C. Log phase cells were

harvested by centrifugation, counted on a hemocytometer using phase contrast microscopy, pelleted by centrifugation at 4,000 xg for 10 min, and resuspended in phosphate buffered saline (PBS) at a concentration of  $1 \times 10^9$  CFU/mL. To prevent desiccation of the bacteria during testing, a hydration chamber was prepared consisting of a sterile 76 x 76 mm gauze pad placed in the bottom of a sterile 150 x 15 mm Petri dish. The gauze pad was saturated with 5 mL of sterile water and the test samples placed on top. A 10  $\mu$ L aliquot containing  $1 \times 10^7$  bacteria was added to each test film (approximately 188 mm<sup>2</sup>), and then placed in a hydration chamber at room temperature. After 2 h of incubation, bacteria were recovered by placing the film in a tube containing 5 mL sterile Lethen media, followed by 30 sec of vortexing. Serial dilutions were carried out, and incubated for 18 h at 37 °C with agitation. Following incubation, the cultures were examined for the presence of turbidity, indicating bacterial growth. Each film was tested in triplicate. Log kill was determined by the following: Log kill = 7 - highest dilution exhibiting bacterial growth. All bacterial challenge procedures were conducted using standard aseptic techniques in a BSL-2 hood.



## **4. AMPHIPHILIC C<sub>60</sub> FULLERENE – DISTRIBUTION AND ACTIVITY**

### **4.1. Overview**

Release of toxic chemicals, such as pesticides and chemical warfare agents, often results in large-scale contamination of surrounding material surfaces. These surfaces have the potential to remain contaminated for an extended duration as many contaminants are persistent and resistant to environmental degradation. Furthermore, limitations of contaminant detection and decontamination solutions result in increased risk of exposure to humans. Surfaces are often coated with paint for improved aesthetics and protection; however, additional functionalities that impart continuous self-decontaminating and self-cleaning properties would be extremely advantageous. In this study, photochemical additives based on C<sub>60</sub> fullerene were incorporated into polyurethane coatings to investigate their coating compatibility and ability to impart chemical decontaminating capability to the coating surface. C<sub>60</sub> exhibits unique photophysical properties, including the capability to generate singlet oxygen upon exposure to visible light; however, C<sub>60</sub> fullerene exhibits poor solubility in solvents commonly employed in coating applications. A modified C<sub>60</sub>, containing a hydrophilic moiety, was synthesized to improve polyurethane compatibility and facilitate its segregation to the polymer-air interface. Bulk properties of the polyurethane films were analyzed to investigate additive-coating compatibility. The polymeric coatings containing photoactive additives were subjected

to self-decontamination challenges against representative chemical contaminants and the effects of additive loading concentration, light exposure, and time on chemical decontamination are reported. The degradation pathways deduced from contaminant challenge by-product analyses are detailed. These new continuously active self-decontaminating systems have the potential for significantly reducing the exposure of toxic substances to civilian population.

#### **4.2. Prologue**

Chemical toxicants, such as pesticides and toxic industrial chemicals, have the potential to contaminate material surfaces for extended periods of time. Often the natural attenuation of toxic substances through evaporation and degradation in ambient environments occurs slowly due to low vapor pressure, poor solubility, and resistance to hydrolysis.<sup>149</sup> Due to this persistence, surfaces on which toxic chemicals reside pose human exposure risks that require application of decontamination solutions to completely render a surface safe. However, decontamination solutions and procedures are cumbersome, expensive, and often damaging to the contaminated substrate.<sup>74</sup>

Polymeric coatings are applied to many surfaces to improve aesthetics and provide corrosion or weathering protection; therefore, they provide an ideal substrate to incorporate coating additives to impart continuous self-decontaminating behavior at the surface and reduce subsequent contamination. A minimal loading concentration of additive is ideal so that the properties beneficial for the originally intended purpose of the polymer coating are maintained. Specifically, polyurethanes are of broadest interest owing to their properties such as chemical resistance and durability.<sup>43</sup>

Several recent research developments have investigated the incorporation of novel reactive additives into various urethane coating formulations in attempts to create coatings that self-decontaminate. Antimicrobial coatings have been successfully created by imparting additives such as nonionic biocides,<sup>71</sup> quaternary ammonium biocides,<sup>51,70</sup> surface concentrating biocides,<sup>49</sup> functionalized coatings,<sup>68,69</sup> and antimicrobial peptides.<sup>50</sup> While these are successful biocidal additives, less success has been achieved in chemical decontaminating coatings. One reason is that additives for chemical decontamination are limited to only a few modes of action such as absorption, hydrolysis, and oxidation. Of these, oxidation offers the greatest potential to completely detoxify a broad spectrum of chemical contaminants.<sup>2</sup>

C<sub>60</sub> fullerene molecules have also been observed to exhibit intriguing photochemical properties, including oxidative capabilities, which hold exciting potential for development of a self-decontaminating coating.<sup>78–81</sup> Upon exposure to visible light, C<sub>60</sub> fullerene is first excited to its singlet state C<sub>60</sub> (<sup>1</sup>C<sub>60</sub>), which then through intersystem crossing (ISC), forms the triplet state species of C<sub>60</sub> (<sup>3</sup>C<sub>60</sub>). <sup>3</sup>C<sub>60</sub> has a lifetime on the order of μs whereas <sup>1</sup>C<sub>60</sub> exhibits a lifetime of several ns.<sup>78,86–88</sup> This triplet state species of fullerene has the ability to convert ground state triplet oxygen (<sup>3</sup>Σ<sub>g</sub><sup>-</sup>) into singlet oxygen (<sup>1</sup>Δ<sub>g</sub>), a reactive oxygen species (ROS).<sup>79,84</sup> The combination of a high quantum yield<sup>79</sup> and low rate of degradation of C<sub>60</sub> fullerene by ROS<sup>78</sup> make this molecule extremely attractive as a photo-active coating additive.

Extensive studies have been conducted to analyze and characterize the photosensitivity of C<sub>60</sub> in solution with varying degrees of success.<sup>84,86,89–92,150</sup> Various

photosensitizers have been shown to exhibit antimicrobial activity when incorporated into polyurethane coating systems under specific conditions.<sup>151–153</sup> Similarly, antiviral systems have successfully been developed with the incorporation of fullerene as a solid-phase photosensitizer into biological fluid.<sup>154</sup> Recently, fullerenes modified with intercalated constituents have displayed remarkable ability to produce singlet oxygen as well as antimicrobial activity in polymeric adhesive films.<sup>73</sup> However, insertion of intercalated constituents into fullerenes introduces additional cost and complexity that may be avoided by utilizing neat C<sub>60</sub>.

Incorporation of C<sub>60</sub> fullerene into polymer matrices has been investigated for applications ranging from photovoltaics<sup>155</sup> to augmentation of polymer mechanical properties.<sup>156</sup> Covalent incorporation of C<sub>60</sub> fullerene into polymers offers controlled distribution and reduced leaching, however often at the sacrifice of photoactivity.<sup>157,158</sup> In contrast, non-covalent incorporation of C<sub>60</sub> fullerene offers simplified formulation and unaffected photophysical properties.<sup>159</sup> Furthermore, non-covalent incorporation of an amphiphilic fullerene species affords the potential for surface segregating photoactive additives. While synthetic modification of C<sub>60</sub> into an amphiphilic species most likely will affect the photophysical properties of C<sub>60</sub>, increased concentration of photoactive additive at the surface of a polymer due to amphiphilic character should improve decomposition of surface residing chemical contaminants.

It can be assumed that when incorporated into a polymer matrix, the photoactivity of fullerene may be reduced due to a lack of molecular oxygen available to the fullerene molecule if it is encapsulated into the bulk of the polymeric coating. However, if one is

able to overcome this limitation, significant activity should remain at the coating-air interface, then one should expect that the production of ROS would result and subsequently react with any contamination that may be on the surface. Furthermore, an amphiphilic additive that automatically segregates to the polymer-air interface during film cure would improve decontaminating efficiency. The hypothesis proposed herein is that the fullerene contained in the coating produces singlet oxygen from the atmosphere by the aforementioned mechanism, which subsequently reacts with undesired contamination analytes that are present on the surface. If such analytes are hazardous, such as the case of pesticides or chemical warfare agents, then the action of the additive in the coating should reduce the hazard and subsequently present a surface free from contamination.

### **4.3. Results and Discussion**

#### **4.3.1. Additive-Polymer Compatibility**

Additive-polymer compatibility and the effects of photoactive additive incorporation on Tecoflex film properties were investigated with a variety of methods. ATR-IR analysis was performed to investigate the effect of C<sub>60</sub> incorporation on infrared signature and probe the chemical composition of the polymer film. ATR-IR analysis confirmed that the low loading concentrations employed in this study allowed the chemical signature of polymer film to be maintained despite increasing concentrations of C<sub>60</sub> and EO<sub>3</sub>-C<sub>60</sub> (Figure 4.1).

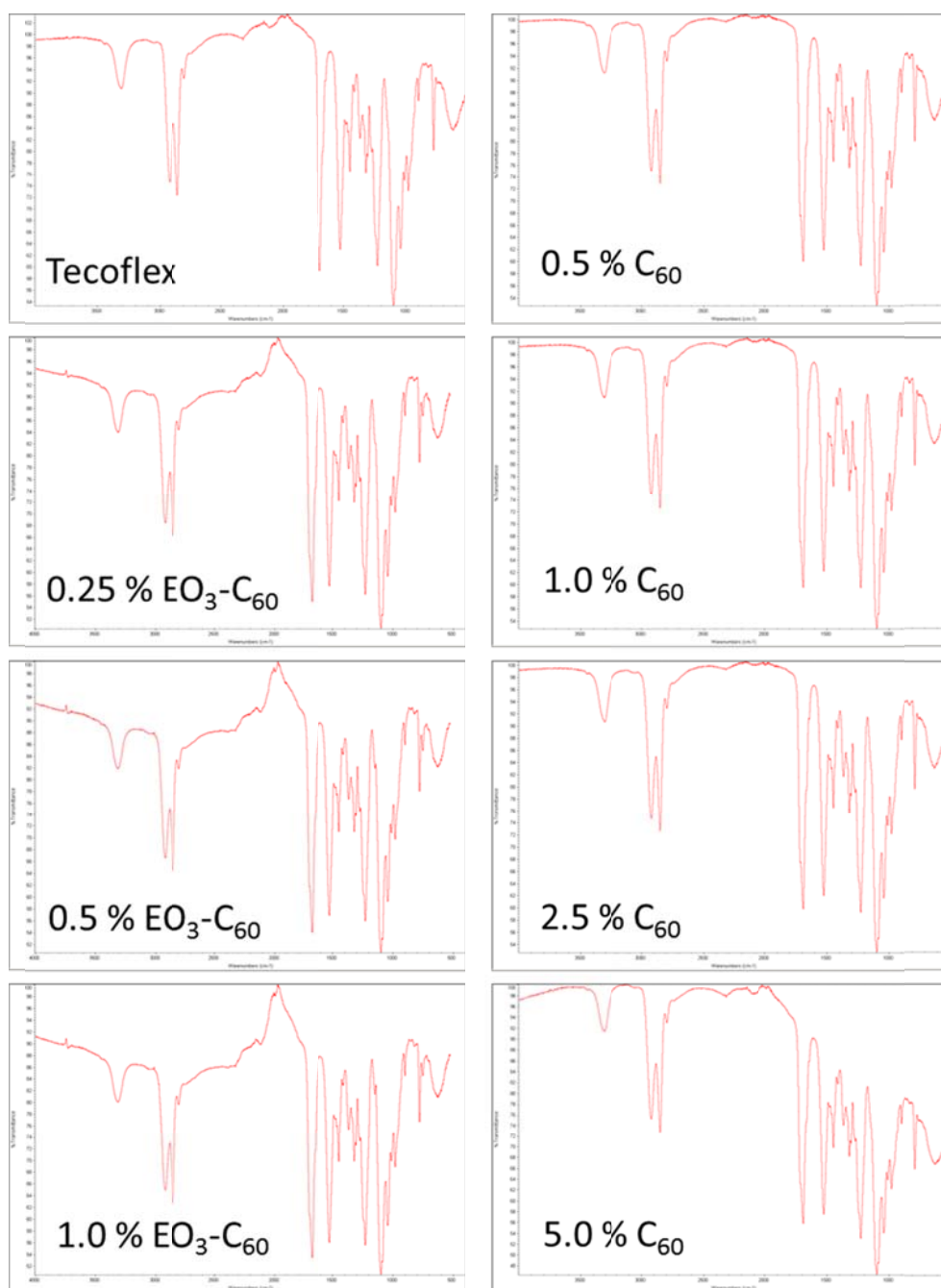


**Figure 4.1.** ATR-IR spectra of Tecoflex films containing  $C_{60}$  and  $EO_3-C_{60}$  additives.

Effects of additive incorporation on thermal stability of Tecoflex films were investigated with TGA. The incorporation of  $C_{60}$  and  $EO_3-C_{60}$  into Tecoflex films each

resulted in an increased thermal stability (Table 4.1). The incorporation of EO<sub>3</sub>-C<sub>60</sub> in Tecoflex resulted in increased thermal stability (temperature at 10 % loss) that scaled linearly with loading concentration. The increase in initial thermal stability suggests that stabilizing intermolecular interactions were occurring between EO<sub>3</sub>-C<sub>60</sub> and Tecoflex polymer. Generally, the incorporation of C<sub>60</sub> into Tecoflex demonstrated a moderate increase in thermal stability. A weak inverse relationship was observed with increased loading of C<sub>60</sub> and thermal stability, as opposed to the direct relationship of EO<sub>3</sub>-C<sub>60</sub> loading. This suggested that with increased loading concentration, additional C<sub>60</sub> aggregated to other C<sub>60</sub> instead of interacting with polymer matrix. Additionally, the lessened effect on thermal stability upon C<sub>60</sub> incorporation compared to EO<sub>3</sub>-C<sub>60</sub> indicated that EO<sub>3</sub>-C<sub>60</sub> interacted more strongly than C<sub>60</sub> with Tecoflex polymer matrix. The greater favorable interactions between EO<sub>3</sub>-C<sub>60</sub> and Tecoflex resulted from compatibility between the ethylene oxide tail of EO<sub>3</sub>-C<sub>60</sub> and the ether regions of the butane diol constituents of the Tecoflex monomer.

**Table 4.1.** TGA data of Tecoflex films.

<b>Tecoflex Film</b>	<b>10% loss (°C)</b>	<b>Final Mass (%)*</b>
Control	300.55	0.2727
0.5% C <sub>60</sub>	314.99	1.463
1.0% C <sub>60</sub>	311.07	2.561
2.5% C <sub>60</sub>	307.38	6.574
5.0% C <sub>60</sub>	309.86	11.25
0.25% EO <sub>3</sub> -C <sub>60</sub>	312.61	0.6591
0.5% EO <sub>3</sub> -C <sub>60</sub>	319.44	0.7918
1.0% EO <sub>3</sub> -C <sub>60</sub>	325.63	1.513

\*At 600 °C in N<sub>2</sub>

TGA analysis also indicated that incorporation of C<sub>60</sub> into Tecoflex resulted in greater ultimate mass remaining than those loaded with EO<sub>3</sub>-C<sub>60</sub>. The ethoxy moiety of the EO<sub>3</sub>-C<sub>60</sub> was susceptible to thermal degradation at a greater temperature than the fullerene cage of C<sub>60</sub>. Therefore, each comparable loading concentration of C<sub>60</sub> (720 g/mol) and EO<sub>3</sub>-C<sub>60</sub> (881 g/mol) contained a 1.22 fold molar excess of C<sub>60</sub> to EO<sub>3</sub>-C<sub>60</sub>. Thus, the thermal degradation of the alkoxy tail of EO<sub>3</sub>-C<sub>60</sub> below 600 °C resulted in only 82 % remaining of the total loaded EO<sub>3</sub>-C<sub>60</sub>. Considering this, at 600 °C there should have been approximately a 1.5x excess remaining mass % of C<sub>60</sub> relative to EO<sub>3</sub>-C<sub>60</sub> at comparable loading concentrations. Indeed, such an excess was observed upon comparison of the 1 wt% loadings.

Interestingly, the ultimate wt% for each Tecoflex film containing additives was greater than the additive wt% loading concentration (Table 4.1). The amount of mass remaining from the thermal degradation of Tecoflex films containing C<sub>60</sub> at 600 °C corresponded to approximately double the C<sub>60</sub> loading concentration. This indicated one



of two possibilities: a quantity of Tecoflex polymer was strongly adhered to the surface of  $C_{60}$  fullerene through intermolecular forces that required greater than 600 °C to dissociate or aggregation of  $C_{60}$  resulted in thermally stabilized Tecoflex polymer trapped within the aggregate. However, the lower thermal degradation onset temperature of Tecoflex films containing  $C_{60}$  than  $EO_3-C_{60}$  revealed that intermolecular interactions were stronger for  $EO_3-C_{60}$ . The difference between the final mass remaining and loading concentration decreased with increased additive loading concentration of both  $C_{60}$  and  $EO_3-C_{60}$ , which suggested that with increased loading concentration, additional intermolecular  $C_{60}$  aggregation occurred instead of  $C_{60}$ -polymer matrix interactions. The deviation was greater for  $C_{60}$  than it was for  $EO_3-C_{60}$ , indicating that aggregation is more prominent in  $C_{60}$  than  $EO_3-C_{60}$ .

DSC was performed on all Tecoflex films to investigate effects of additive incorporation on glass transition temperature ( $T_g$ ). The way in which additive incorporation affects  $T_g$  can afford insight into intermolecular interactions between the additive and polymer. Increase in  $T_g$  resulting from additive incorporation would indicate increased intermolecular interactions that limit polymer mobility.<sup>160</sup> Unmodified Tecoflex exhibits a glass transition that spans a broad temperature range. Minor and insignificant effects on  $T_g$  resulted from the incorporation of both additives,  $C_{60}$  and  $EO_3-C_{60}$ , which indicated that the integrity of the coatings were preserved.

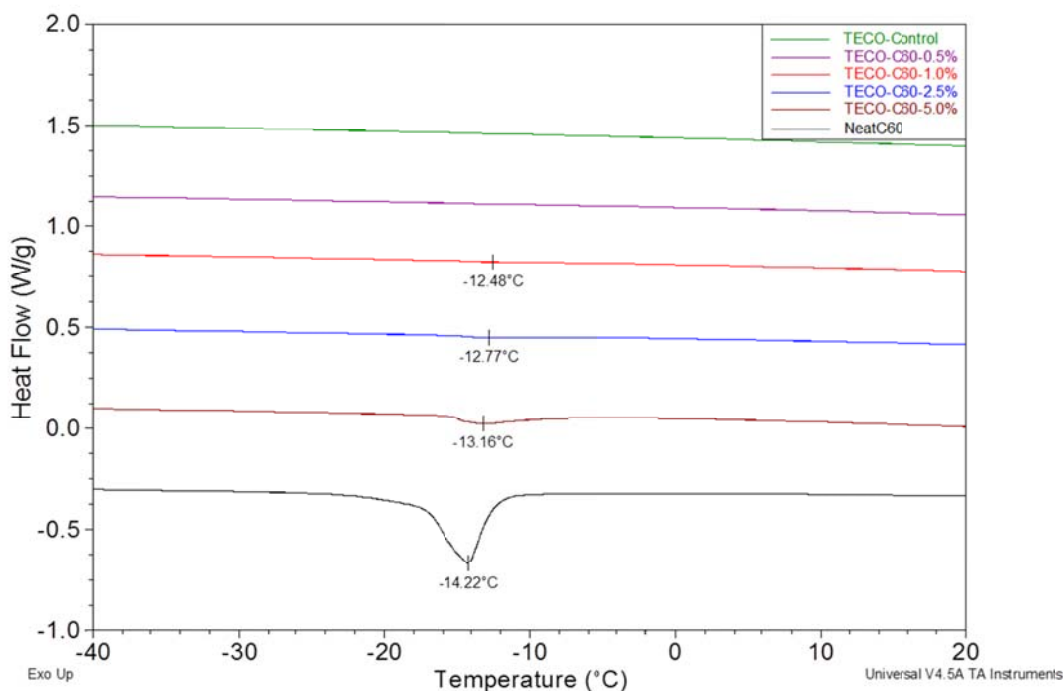


**Figure 4.2.** Comparison of DSC thermograms for Tecoflex films containing  $C_{60}$  and neat  $C_{60}$ .

For both neat  $C_{60}$  and Tecoflex films containing higher concentrations of  $C_{60}$ , an endothermic transition was observed in the DSC thermograms at approximately  $-14^{\circ}\text{C}$ . The magnitude of the endothermic peak increased corresponding to  $C_{60}$  concentration (Figure 4.2). This endotherm corresponded to the phase transition of  $C_{60}$  crystals from simple cubic orientation ordering to face centered cubic structure upon heating through the transition temperature.<sup>161,162</sup> The presence of this transition from Tecoflex films indicated a crystalline phase of  $C_{60}$  fullerene.  $C_{60}$  can only be in a crystalline phase when multiple fullerene molecules are in contact with one another, or aggregated, in a regular, repeated order. A polymeric film in which  $C_{60}$  fullerene was completely dispersed would not exhibit such crystalline phase transition. Furthermore, endotherm corresponding to

the simple cubic to face centered cubic phase transition was absent in the DSC analysis of neat EO<sub>3</sub>-C<sub>60</sub> and the Tecoflex films containing EO<sub>3</sub>-C<sub>60</sub>. Therefore, aggregation, or at least the formation of crystallites, of C<sub>60</sub> was inhibited by the covalent modification of C<sub>60</sub> with ethylene oxide tails. Further, the amphiphilic character of the EO<sub>3</sub>-C<sub>60</sub> improved solubility of the additive in the Tecoflex solution and facilitated increased molecular dispersion of the additive throughout the polymer matrix.

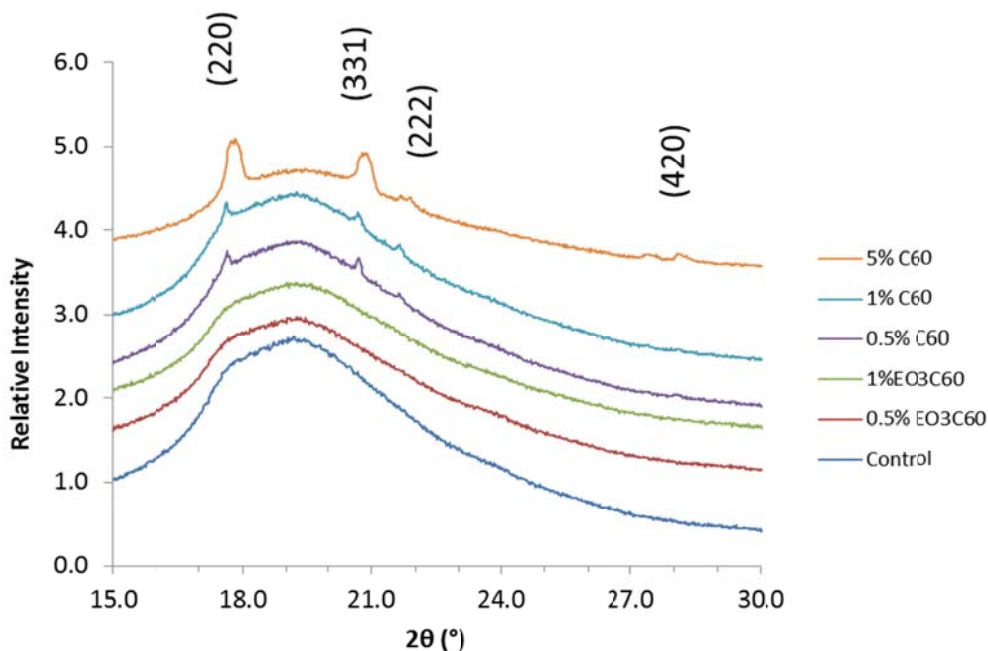


**Figure 4.3.** XRD patterns of Tecoflex films containing additives.

X-Ray diffraction analysis (Figure 4.3) confirmed crystallinity observed via DSC. Diffraction peaks corresponding to the (220), (331), (222), and (420) peaks of crystallized C<sub>60</sub> were observed in the Tecoflex films containing unmodified C<sub>60</sub> additive.

The intensity of diffraction peaks increased with increased loading of  $C_{60}$  from 0.5 to 5.0 wt%. In contrast, control Tecoflex and Tecoflex loaded with  $EO_3-C_{60}$  displayed only a broad peak resulting from the amorphous polymer. Therefore,  $C_{60}$  aggregated into crystals in Tecoflex matrix, while  $EO_3-C_{60}$  was well dispersed.

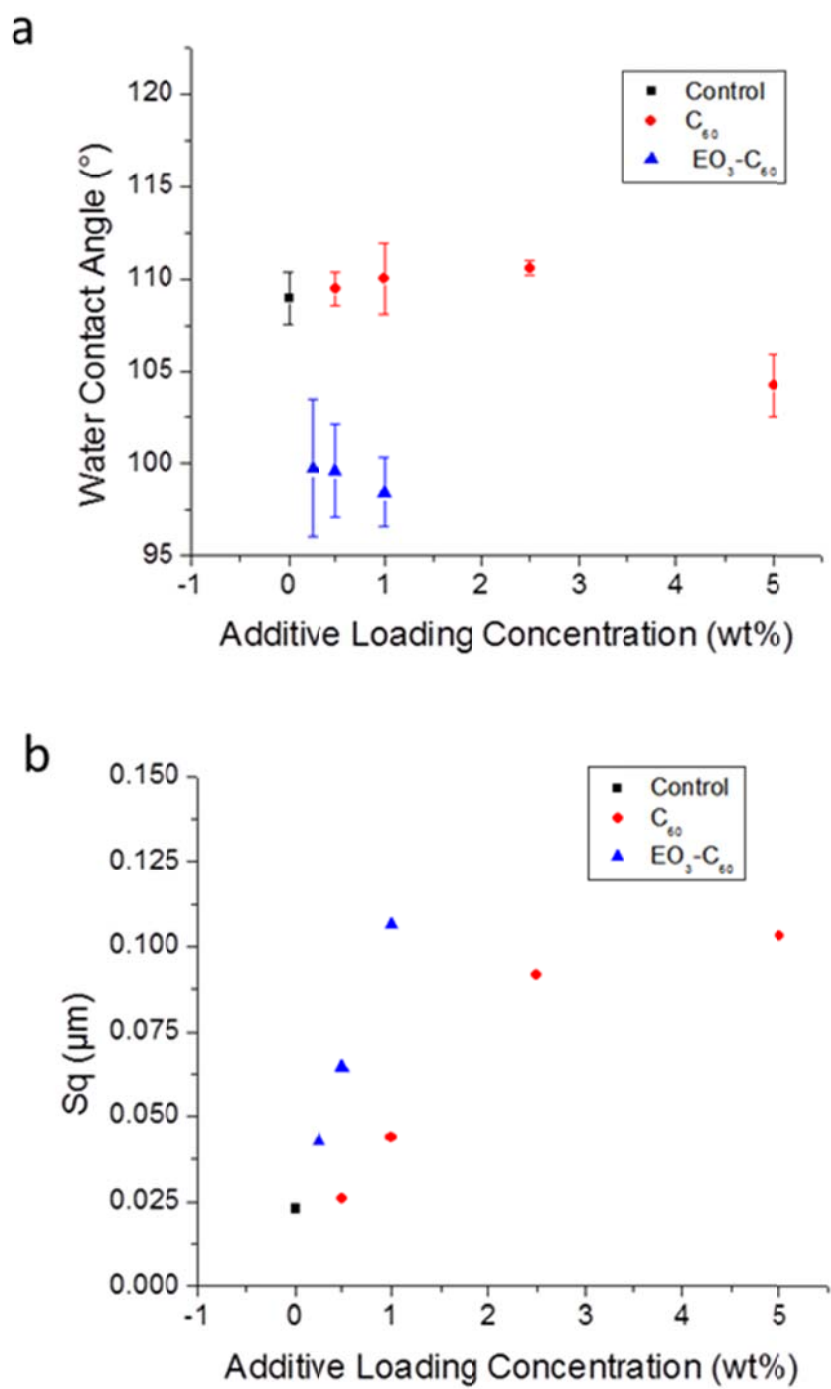


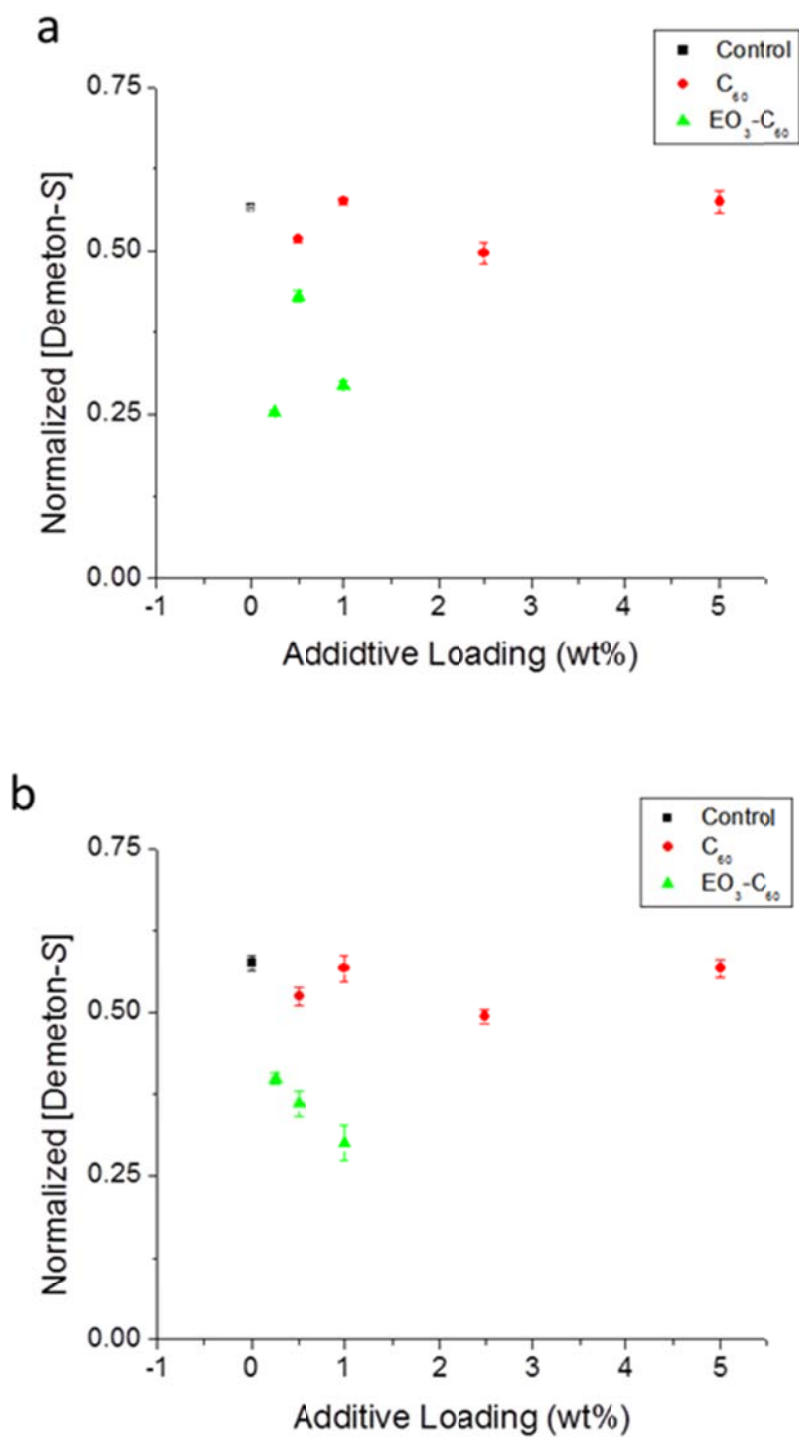
**Figure 4.4.** a) Water contact angle and b) surface roughness (Sq) of Tecoflex films loaded with  $C_{60}$  and  $EO_3-C_{60}$ .

Water contact angle measurements were performed on Tecoflex films containing  $C_{60}$  and  $EO_3-C_{60}$ , the results of which are shown in Figure 4.4. Addition of  $C_{60}$  in Tecoflex resulted in minor increases in water contact angle in loadings up to 2.5 wt% and ultimately a minor decrease at 5 wt%  $C_{60}$  loading. Correspondingly, the surface roughness of Tecoflex films increased with increased  $C_{60}$  loading (Figure 4.4b). On the other hand, loading of  $EO_3-C_{60}$  in Tecoflex resulted in a significant decrease in water contact angle accompanied with a linear increase surface roughness to a greater degree than  $C_{60}$ . Therefore, comparison of contact angle and surface roughness indicated that surface roughness played an insignificant role in the water contact angle, despite previous evidence to the contrary.<sup>163</sup> Thus the change in water contact angle must result from the additive's effect on the surface energy of Tecoflex, instead of imparted surface roughness.

The covalent attachment of ethylene glycol moiety to  $C_{60}$  resulted in a molecule with amphiphilic character, i.e. a surfactant. When incorporated into a solution of hydrophobic Tecoflex, the amphiphilic  $EO_3-C_{60}$  has the potential to orient its hydrophilic moiety at the polymer-air interface in order to minimize solvophobic interactions between hydrophilic ethylene oxide and hydrophobic Tecoflex matrix. Indeed, a linear decrease in contact angle was observed between 0.25 and 1.0 wt% loadings of  $EO_3-C_{60}$ . Considering that the highest loading (5 %) of  $C_{60}$  in Tecoflex resulted in decrease in water contact angle of only  $4^\circ$ , the significant decrease in water contact angle (increase in hydrophilicity) of  $10^\circ$  at only 1 wt% loading of  $EO_3-C_{60}$  indicated that the additive was concentrated at surface of the polyurethane film.

#### **4.3.2. Decontamination Challenges**

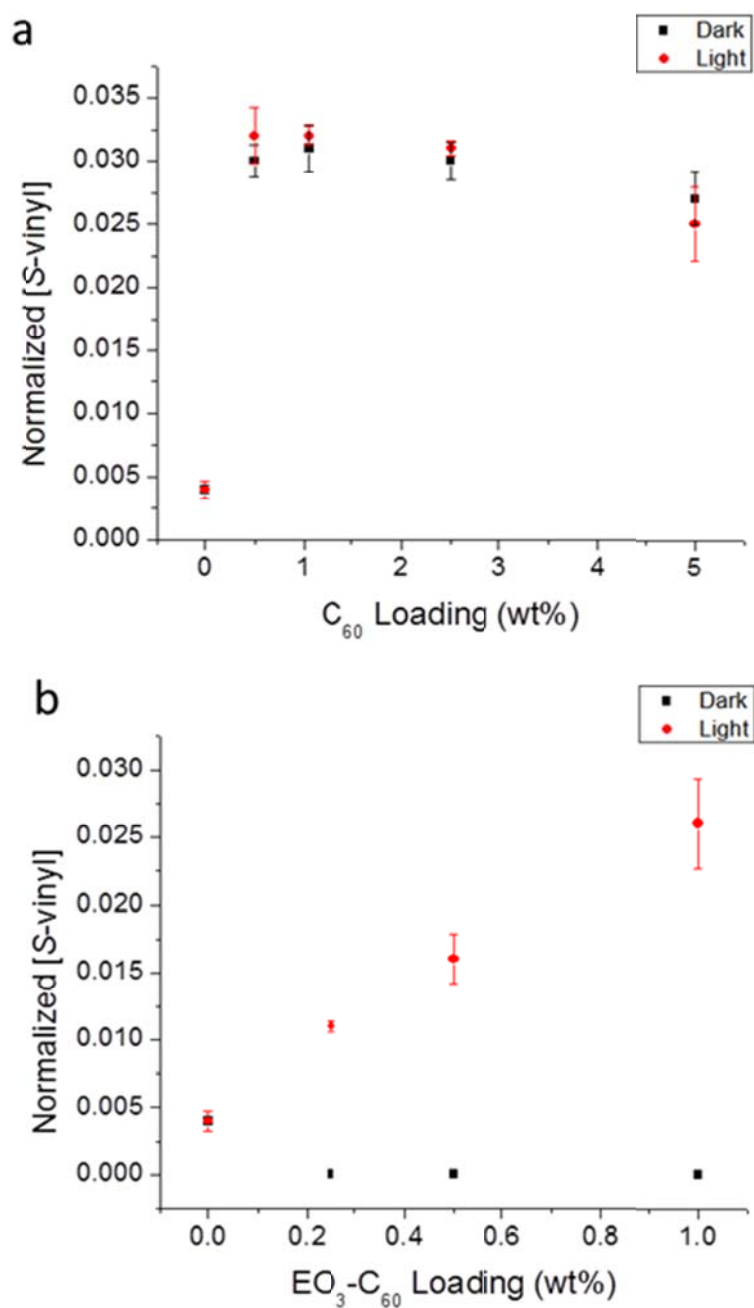
Decontamination challenges were employed to investigate the capability imparted by photoactive additives  $C_{60}$  and  $EO_3-C_{60}$  onto Tecoflex films to automatically decompose surface residing contaminants. Two chemical compounds, Demeton-*S* and CEPS, were employed as representative contaminants. The prepared films were first subjected to decontamination challenges consisting of 18 hour contaminant residence time.



**Figure 4.5.** Demeton-S recovered from Tecoflex films after 18 hour residence in dark (a) and daylight (b) conditions.

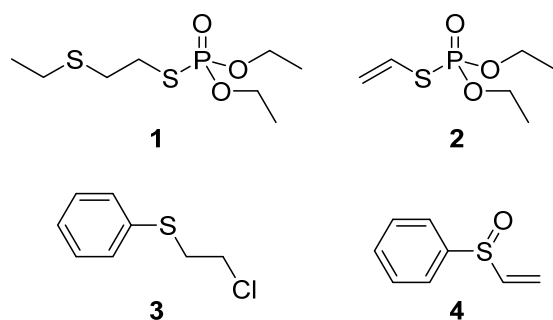


Figure 4.5 presents results from a 4 g/m<sup>2</sup> Demeton-*S* decontamination challenge in which extracted Demeton-*S* (normalized by the tetralin internal standard) is plotted against additive loading concentration. No correlation was observed between C<sub>60</sub> loading concentration in Tecoflex films and Demeton-*S* reduction. Furthermore, reduction of Demeton-*S* on C<sub>60</sub> exhibited similar trends in both dark and light conditions. Tecoflex films containing EO<sub>3</sub>-C<sub>60</sub> exhibited increased reduction of Demeton-*S* compared to films containing C<sub>60</sub> in dark conditions; however, decomposition of Demeton-*S* did not directly correlate with additive loading. Tecoflex films exposed to light that contained EO<sub>3</sub>-C<sub>60</sub> exhibited a direct correlation between the reduction of Demeton-*S* and EO<sub>3</sub>-C<sub>60</sub> loading concentration. From this, it was proposed that different modes of action for Demeton-*S* degradation were occurring between Tecoflex films containing C<sub>60</sub> and EO<sub>3</sub>-C<sub>60</sub>, thus necessitating additional decomposition by-products analysis.



**Figure 4.6.** Detected *S*-vinyl product (shown as normalized ratio of *S*-vinyl peak area to tetralin peak area) from Tecoflex films loaded with a) C<sub>60</sub> and b) EO<sub>3</sub>-C<sub>60</sub> over an 18 h Demeton-*S* challenge.

By-product analysis of the 18 h Demeton-*S* decontamination challenges were performed for further insight into possible modes of action. In addition to reduction in Demeton-*S*, significant by-products were detected at a retention time of 4.1 min, which corresponded to vinyl oxidation product (*S*-vinyl) (**2**). By-product concentration, normalized with the internal standard, is plotted against loading concentration in Figure 4.6. It was apparent that increased C<sub>60</sub> loading led to decreased production of **2** in both dark and light conditions, whereas increased concentration of EO<sub>3</sub>-C<sub>60</sub> loading resulted in increased production of **2**. Unmodified C<sub>60</sub> was more reactive than EO<sub>3</sub>-C<sub>60</sub>, especially at low concentrations; however, increased concentration of C<sub>60</sub> did not result in increased decomposition, most likely due to self-quenching resulting from high C<sub>60</sub> proximity from aggregation in the polymer matrix. Qualitative observation indicated that poor solubility of C<sub>60</sub> in chloroform facilitated the formation of C<sub>60</sub> aggregates, in which the probability of self-quenching between C<sub>60</sub> molecules was increased.



**Figure 4.7.** Demeton-*S* (**1**), *S*-vinyl degradation product (**2**), CEPS (**3**), and vinyl phenyl sulfoxide (**4**).

For Tecoflex films containing C<sub>60</sub>, comparable amounts of **2** were detected from decomposition of Demeton-*S* on films that resided in dark and light conditions for 18 h (Figure 4.6a). From this, it appeared that photoactivity against Demeton-*S* was not occurring in the Tecoflex films containing unmodified C<sub>60</sub>. If photoactivity was occurring, then a greater amount of **2** would be observed on the films exposed to light than in darkness. It has been previously demonstrated that C<sub>60</sub> fullerene can behave as an electron acceptor (Lewis acid) toward sulfides.<sup>164</sup> Thus, the electron acceptor behavior of C<sub>60</sub> in Tecoflex may have facilitated the cleavage of the S-C bond (Figure 4.8) that resulted in the elimination product **2**.

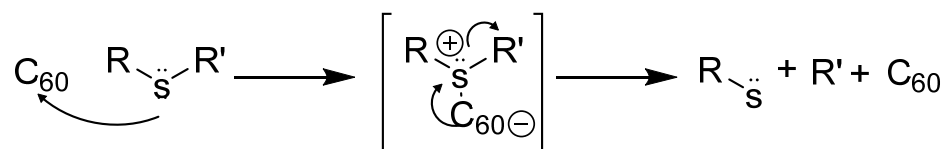


**Figure 4.8.** Hypothesized Lewis acid catalyzed sulfide elimination.

Photoactivity was apparent from by-product analysis in the films loaded with EO<sub>3</sub>-C<sub>60</sub> (Figure 4.6b). In fact, the photoactivity of EO<sub>3</sub>-C<sub>60</sub> continued to increase with increasing concentration, which indicated that the ethylene oxide moieties helped to diminish aggregate facilitated self-quenching by improved solubility. In contrast to the films containing C<sub>60</sub>, an absence of Demeton-*S* decomposition on Tecoflex films containing EO<sub>3</sub>-C<sub>60</sub> in dark conditions was observed. This was likely the result of

decreased Lewis acid character upon the covalent attachment of the ethylene oxide moiety.

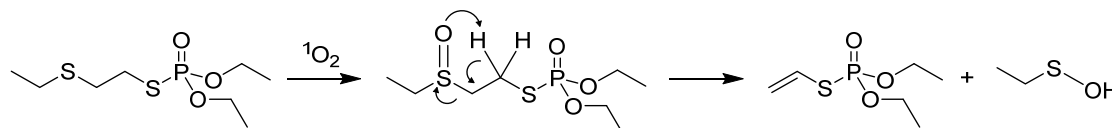


**Figure 4.9.** Proposed oxidation mechanism of Demeton-S and the formation of elimination product from photogenerated singlet oxygen.

The combination of photoactivity and oxidation products detected from Tecoflex films containing EO<sub>3</sub>-C<sub>60</sub>, and documented capability of fullerene species to photogenerate singlet oxygen<sup>165</sup> has led to the proposed mode of action for Demeton-S decomposition on films containing EO<sub>3</sub>-C<sub>60</sub> exposed to visible light presented in Figure 4.9. The photoactive species embedded in the polymer matrix was first photosensitized upon the absorption of visible light. Subsequent transfer of energy from photosensitized EO<sub>3</sub>-C<sub>60</sub> to ambient atmospheric oxygen resulted in the formation of singlet oxygen (<sup>1</sup>O<sub>2</sub>). The photogenerated singlet oxygen, a ROS, then oxidized the peripheral sulfur of Demeton-S that was residing on the coating surface in proximity to the photosensitized additive. The sulfoxide then underwent  $\alpha$  elimination to result in the Demeton-S vinyl degradation product (**2**) and unstable sulfenic acid, which quickly self-condenses to form the corresponding thiosulfinate.

In addition to decontamination challenges against Demeton-S, Tecoflex films loaded with photoactives were also subjected to CEPS decontamination challenges. An 18 hour decontamination challenge was initially performed for each sample in both dark

and light conditions. Despite minor differences in the amount of CEPS decomposed, significant differences in by-product formation were observed to be dependent on the conditions in which the sample resided.

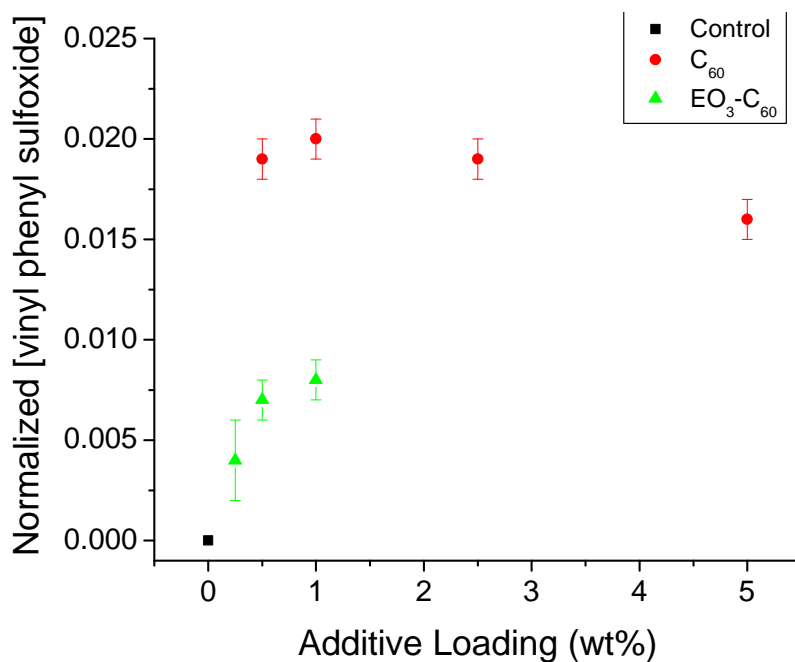


**Figure 4.10.** CEPS by-product resulting from residence on Tecoflex films of several additive concentrations following exposure to daylight conditions for 18 hrs.

GC-MS analysis afforded the detection of a notable degradation product of CEPS from the Tecoflex films containing photoactives which resided in daylight conditions. Mass spectra analysis determined that the degradation product was vinyl phenyl sulfoxide (**4**), an oxidation by-product of CEPS (Figure 4.7). Furthermore, **4** was not detected from coatings that resided in dark conditions. Figure 4.10 presents normalized concentrations of **4** detected in the reaction extract from Tecoflex films loaded with C<sub>60</sub> and EO<sub>3</sub>-C<sub>60</sub>

after an 18 hour residence time of CEPS. Production of **4** from Tecoflex films decreased with increased  $C_{60}$  loading concentration. This was attributed to increasing  $C_{60}$  aggregation with increased  $C_{60}$  loading concentration due to poor solubility and incompatibility with the polyurethane matrix, as previously demonstrated via DSC and XRD. The increase in aggregation effectively limited the available surface area of  $C_{60}$  available for both singlet oxygen generation and contact with the contaminant. Additionally, singlet oxygen quenching is known to occur between proximal  $C_{60}$  molecules in high concentration, such as in aggregates and crystallites.<sup>166</sup>

In contrast to the effects observed resulting from  $C_{60}$  loading concentration, the generation of **4** increased with increasing  $EO_3$ - $C_{60}$  concentration in Tecoflex from 0.25 to 1.0 wt%. This direct correlation of  $EO_3$ - $C_{60}$  loading and generation of **4** can only result from minimized self-quenching due to good dispersion of  $EO_3$ - $C_{60}$ . These trends support those that were observed in the Demeton-*S* decontamination challenge.

From the above 18 h study, 1 wt% loadings of  $C_{60}$  and  $EO_3$ - $C_{60}$  were down-selected for an expanded time dependent CEPS decontamination challenge over the course of 165 h in daylight conditions (Figure 4.11). Figure 4.11 a displays concentration of CEPS extracted from samples over 165 h residence time period. Each of the films subjected to the challenge exhibited rapid decrease in CEPS concentration over the first 48 h. This was attributed to inherent attenuation of CEPS as this behavior was observed on the two controls, a Teflon film and unmodified Tecoflex.  $C_{60}$  and  $EO_3$ - $C_{60}$  films differentiated from the controls at time points beyond 48 h, after which the degradation rates of CEPS on the controls decreased drastically. In contrast, the  $C_{60}$  and  $EO_3$ - $C_{60}$

Tecoflex films exhibited continued linear degradation of CEPS beyond 48 h. This behavior was explained by two separate degradation mechanisms occurring simultaneously. First, the attenuation mechanism dominated the first 48 h of degradation, which was initially at a high rate. Beyond 48 h, attenuation rate slowed to an extent such that the secondary mechanism, photo-oxidation, dominated the overall reaction rate and thus becomes apparent.

By-product analysis (Figure 4.11b) confirmed a linear increase of oxidation product (**4**) over time on films containing photoactive additives. Tecoflex films containing  $C_{60}$  and  $EO_3-C_{60}$  each exhibited a linear relationship between production of oxidation product and residence time, while oxidation was not detected from the controls. The detection of oxidation products only from samples that were exposed to light, that contain either  $C_{60}$  or  $EO_3-C_{60}$ , and dependent on the concentration of  $C_{60}$  and  $EO_3-C_{60}$  indicated that a photo mediated oxidation process was facilitating the oxidation of CEPS.



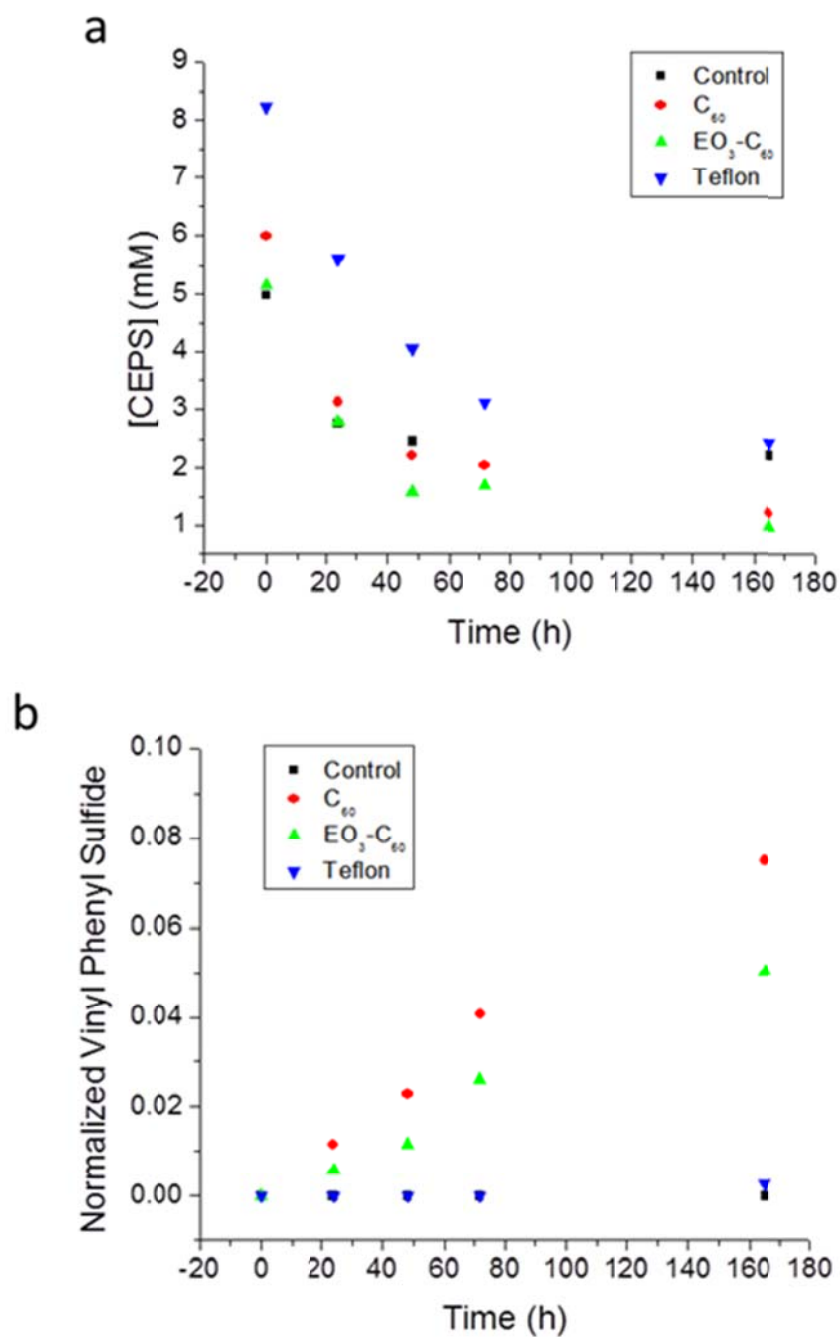


**Figure 4.11.** Concentration of CEPS recovered from samples over 165 hour residence (a) and normalized vinyl phenyl sulfoxide degradation product (b).

In consideration of the data presented herein and the known singlet oxygen generation potential of C<sub>60</sub> fullerene, a proposed mode of action for CEPS oxidation is presented in Figure 4.12. Similar to the mechanism proposed for the oxidation of Demeton-S, the photoactive in Tecoflex generated singlet oxygen upon exposure to light. Singlet oxygen oxidized the S atom to sulfoxide, which then through an elimination mechanism a vinyl sulfoxide was produced with HCl as a by-product. In contrast to the mechanism proposed for Demeton-S, the oxygen remained on the same by-product molecule as sulfur. This was due to the stability of the sulfenic acid leaving group in Demeton-S decomposition compared to the instability of the potential hypochlorite by-product in CEPS oxidation.

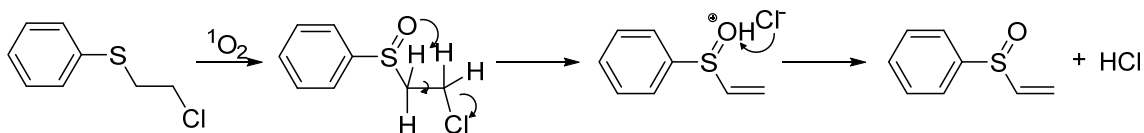


**Figure 4.12.** Potential pathway of sulfide oxidation followed by dehydrohalogenation of CEPS.

#### 4.4. Summary

Several insights were gained upon the incorporation of C<sub>60</sub> and EO<sub>3</sub>-C<sub>60</sub> into Tecoflex films. The detection of the phase transition from simple cubic to face centered cubic structure at approximately -14 °C, subsequent confirmation with XRD, and the decreased reactivity against simulants at increased C<sub>60</sub> loading concentrations provide evidence of C<sub>60</sub> aggregation in Tecoflex films. Conversely, no such evidence was

observed to indicate that EO<sub>3</sub>-C<sub>60</sub> was aggregating in Tecoflex films. Therefore, the covalent attachment of ethylene glycol tail to C<sub>60</sub> resulted in an additive that exhibited improved solubility and dispersion in the hydrophobic polyurethane matrix of Tecoflex.

Surface decontamination challenges demonstrated the self-cleaning capability of Tecoflex films containing C<sub>60</sub> and EO<sub>3</sub>-C<sub>60</sub> additives. Decomposition products resulting from oxidation were observed in addition to a direct correlation between additive loading concentration and decomposition of surface residing contaminants. Through correlation of trends observed from Demeton-*S* and CEPS decontamination challenges and by-product analysis, modes of action were proposed for the decomposition pathways of both contaminants on the surface of polyurethane films.

#### **4.5. Experimental Methods**

##### **Materials**

All purchased chemicals were reagent grade and were used without further purification. The purchase of 2-chloroethyl phenyl sulfide was made at Sigma–Aldrich (St. Louis, MO, USA). Demeton-*S* was purchased from Chem Service (West Chester, PA, USA). Refined C<sub>60</sub> fullerene was purchased from MER Corporation (Tucson, AZ, USA).

##### **Synthesis of EO<sub>3</sub>-C<sub>60</sub>**

Covalent attachment of triethylene glycol monomethyl ether to C<sub>60</sub> fullerene through azide addition was performed following a previously described method.<sup>167</sup> Product was confirmed by <sup>1</sup>H NMR performed in CDCl<sub>3</sub> on a Bruker 300 MHz nuclear

magnetic resonance spectrometer with a TMS internal standard. Characterization data were consistent with that previously reported.<sup>167</sup>

Covalent incorporation of a hydrophilic tail to C<sub>60</sub> fullerene was performed to result in an amphiphilic additive with the potential to concentrate at the air/coating interface, similar to what has previously been demonstrated with amphiphilic antimicrobial coating additives.<sup>49</sup>

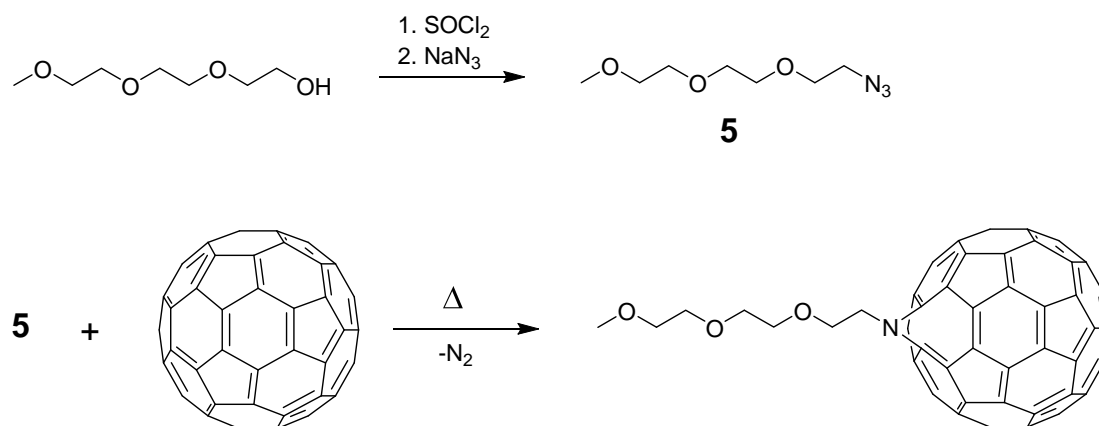


**Figure 4.13.** Reaction scheme for the synthesis of an amphiphilic fullerene additive.

Overall, the synthetic procedure covalently attached triethylene glycol monomethyl ether (**2**) to C<sub>60</sub> fullerene through azide addition (Figure 4.13). The first two steps in the procedure converted triethylene glycol monomethyl ether (**2**) to the azide terminated derivative (**3**). Component **3** was then covalently bound to C<sub>60</sub> fullerene (**4**) through azide addition resulting in the final product EO<sub>3</sub>-C<sub>60</sub> (**1**). Successful isolation of

the product was confirmed with  $^1\text{H}$  and  $^{13}\text{C}$  NMR. Synthesis of  $\text{EO}_3\text{-C}_{60}$  was confirmed via  $^1\text{H}$  NMR analysis by the downfield shift of protons proximal to the N (Figure 4.14).

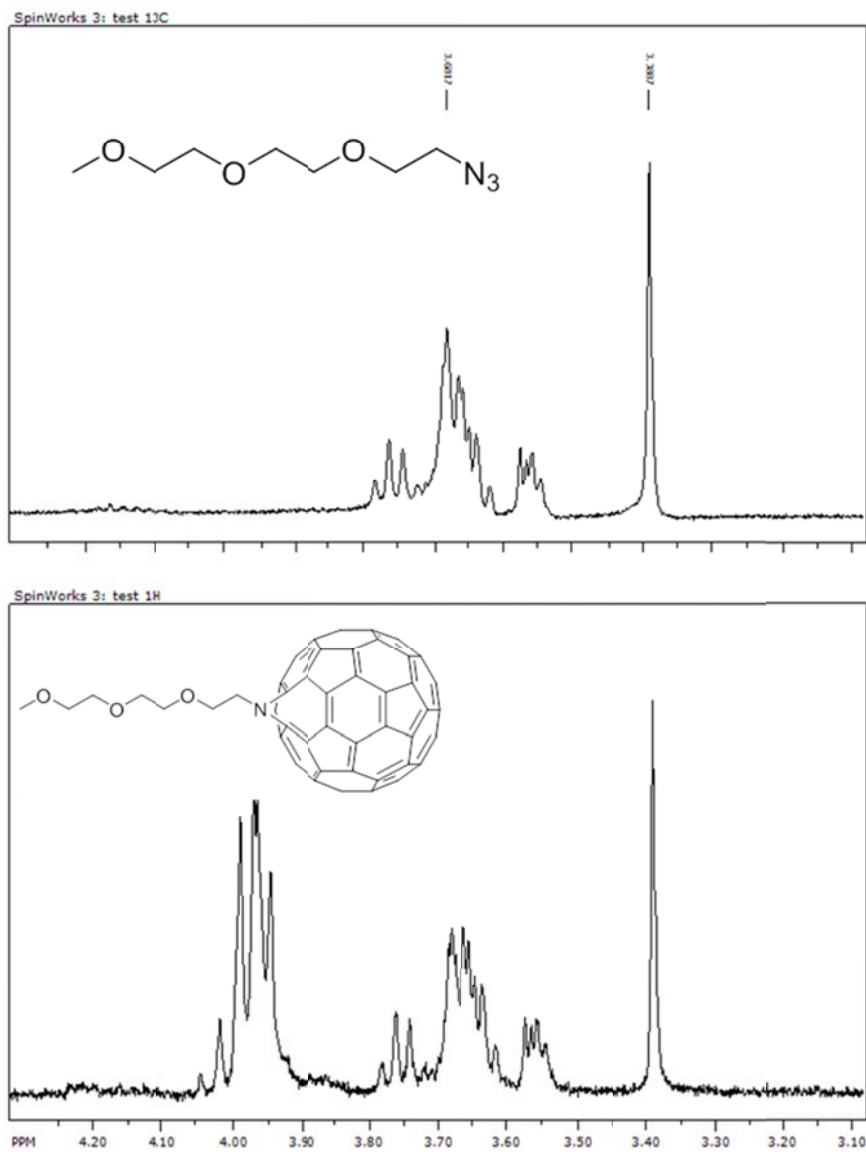


**Figure 4.14.**  $^1\text{H}$  NMR spectra of azide reactant (top) and  $\text{EO}_3\text{-C}_{60}$  product (bottom).

## Polymer Preparation

A commercial polyurethane resin, Tecoflex EG-100A (Lubrizol Advanced Materials, Inc., Gastonia, NC, USA), was employed to investigate behavior of additives in controlled polymer solutions. Polymer solutions were prepared (0.1 g polymer in 1 mL chloroform), to which photoactive additives, C<sub>60</sub> and EO<sub>3</sub>-C<sub>60</sub>, were incorporated. The solutions were vigorously vortexed to ensure complete mixing after addition of additives. After allowing for air bubbles to escape, polymer solutions were poured out into aluminum pans, loosely covered, and allowed to dry. Films with final additive concentrations of 0.25, 0.5, 1.0, 2.5, and 5.0 wt% were prepared.

## Coating Characterization

Free coatings were peeled from aluminum backing and weighed prior to analysis on a TA Instruments (New Castle, DE, USA) DSC Q20 differential scanning calorimeter. Under a nitrogen flow of 50 mL/min, the DSC was first equilibrated to -70 °C. The temperature was then ramped from -70 °C to 170 °C at a rate of 20 °C/min. The procedure was repeated for a second scan with a ramp rate of 10 °C/min. Glass transition temperature ( $T_g$ ) measurements were calculated based on the second scan using Universal Analysis 2000 software. The second scan was used for this value to eliminate any contamination of entrapped volatile and low molecular weight byproducts, as well as demonstrate hysteresis. Thermogravimetric analysis (TGA) was performed on a TA Instruments Q50 TGA employing heating rates of 10 °C/min under a N<sub>2</sub> atmosphere. A Thermo Scientific Nicolet 6700 FTIR (Thermo Scientific, Waltham, MA, USA) equipped

with a diamond crystal ATR attachment was utilized for film analysis. Diffuse reflectance was utilized in the characterization of neat C<sub>60</sub> and EO<sub>3</sub>-C<sub>60</sub>. X-ray diffraction measurements were performed using a Rigaku SmartLab X-ray Diffractometer (XRD, Rigaku, Tokyo, Japan). The SmartLab XRD was equipped with a Cu anode operating at 3 kW generating Cu K $\alpha$  radiation. Measurements were taken with Bragg-Brentano Optics and a D/Tex Detector for 2-Theta measurements from 15° to 40°.

Contact angle measurements were performed using a VCA Optima by AST Products, Inc. (Billerica, MA, USA) employing the sessile drop technique on the surface of the polymer films. Triple-distilled water was employed as a probe liquid, of which at least three replicate measurements were made for each sample. 3D laser confocal microscopy was performed on an Olympus LEXT 3D measuring laser microscope OLS4000. Surface roughness measurements were performed employing an 80  $\mu$ m cutoff wavelength ( $\lambda_c$ ).

### **CWA Simulant Selection**

Because it is impractical to work with real chemical warfare agents in a research environment, CWA decontamination research typically incorporates less harmful substances with which to mimic and simulate the incredibly toxic CWA.<sup>149</sup> These compounds, which share similar chemical and physical properties with CWA, but also exhibit reduced toxicity, are referred to as simulants. There are several criteria which must be considered prior to selection of such compounds. First, the simulant compound must exhibit similar stereochemical interactions, acid-base relationships, and reduction-

oxidation potential as the CWA. The second criterion is that the simulant must exhibit similar physical properties, the most important of which are vapor pressure and polarity. These most significantly affect interactions of the simulants with surfaces. Finally and most importantly, the simulant must be much less toxic than the CWA. CWAs are incredibly potent and dangerous, therefore the toxicity of the simulants must be minimal in order to create a safe and practical laboratory working environment.<sup>23,168</sup>

There are numerous compounds which are similar in chemical structure to *bis*(2-chloroethyl) sulfide (HD). The most important functional group which must be present in an effective HD simulant is the  $\text{RSCH}_2\text{CH}_2\text{Cl}$  moiety. The terminal Cl affects reactivity of the sulfide center, which is the target of oxidation. The sulfur in HD is less reactive towards both hydrolysis and oxidation than a sulfur in alkyl sulfides due to the electron withdrawing effects of the terminal chlorines.<sup>169</sup> It has been mutually agreed upon in the literature that no single simulant is sufficient to cover all aspects of decontamination and consequently, as in other studies, this research utilizes two simulants for HD, 2-chloroethyl ethyl sulfide (2-CEES) and 2-chloroethyl phenyl sulfide (2-CEPS), as depicted in Figure 4.15.



**Figure 4.15.** Structures of HD simulants 2-chloroethyl ethyl sulfide and 2-chloroethyl phenyl sulfide.



2-CEES is structurally very similar to HD and offers similar chemical reactivity, yet exhibits a higher vapor pressure.<sup>149</sup> 2-CEPS contains a bulky phenyl group, which affects the steric interactions and reactivity of the central sulfur relative to HD. However, the vapor pressure and persistence of 2-CEPS are closely related to those of HD.<sup>170</sup> The non-bonding electron pair of the central sulfur in 2-CEPS is stabilized via conjugation to the adjacent aromatic phenyl group. Numerous other groups have successfully utilized these compounds as simulants for research in decontamination methods of HD.<sup>30,66,170–178</sup> Several of the important physical properties of HD and the simulants are compared in Table 4.2.

**Table 4.2.** Physical properties of HD compared with simulants.

	<b>HD</b>	<b>2-CEES</b>	<b>2-CEPS</b>
Molecular Weight (g-mol <sup>-1</sup> )	159	125	173
Liquid Density (g-cm <sup>-3</sup> @ 20 °C)	1.27	1.07	1.17
Boiling Point (°C) (@ 750 mm Hg)	227	156	246
Vapor Pressure (mm Hg @ 20 °C)	7.2 x 10 <sup>-2</sup>	3.79	1.86 x 10 <sup>-2</sup>

There are numerous compounds capable of simulating VX in a laboratory environment. The most important aspects of VX simulants are reduced toxicity and the presence of the phosphonothioate moiety. This region is the target for effective destruction of VX (i.e. oxidation) and therefore needs to be included in the simulant molecules.<sup>1</sup> Additional properties which need to be considered are vapor pressure, persistency and polarity. Taking into account all of the requirements for an appropriate simulant, Demeton-S (Dem) and Malathion (Mal) were selected. These simulants are

known commercial pesticides, which is consistent, as this class of CWAs was derived from pesticides. Figure 1.6 presents the chemical structures of VX and selected simulants. Dem and Mal are both commercial pesticides which previous research efforts have utilized as simulants for VX.<sup>66</sup> Dem shares a similarity to VX in that it has a central phosphorous bound to a divalent sulfur, an ethoxy group, and a double bond to an oxygen atom. Dem is an excellent simulant because the relative reactivity of the P-O bonds and the P-S bonds can be observed through GC/MS product analysis. Degradation pathways and the resulting products of Dem degradation have been identified by previous research.<sup>179</sup> Additionally, the *S*-alkyl group is of similar molecular geometry as the *S*-alkyl bound group in VX, affording similar leaving potential. The *O*-ethyl groups are comparable to the *O*-ethyl group bound to the central phosphorous in VX. The combination of these factors leads to a simulant selection which can effectively mimic the target bonds. Mal exhibits a similar vapor pressure as VX,<sup>149</sup> has minimal toxicity and is commonly applied for insect control.<sup>180</sup>

### **Contaminant Challenge**

The prepared films were subjected to surface decontamination challenges against the chemical analytes presented in Figure 1, Demeton-*S* (**1**) and 2-chloroethyl phenyl sulfide (CEPS) (**2**), across a range of simulated environmental conditions. In general, a 2.0  $\mu\text{L}$  micropipette was used to apply 1.0  $\mu\text{L}$  of analyte to each sample (2  $\text{cm}^2$ ) placed in a transparent Eppendorf tube. Each Eppendorf tube was then sealed and allowed to incubate for determined period of time in controlled conditions (darkness or simulated

daylight). For photochemical reactions, a custom-built temperature controlled photochemical reactor equipped with five F8T5D fluorescent bulbs emitting broad spectrum visible light (Figure 4.16) at 10,000 lux intensity was employed, which simulates overcast daylight exposure. All contaminant challenges, including photochemical challenges, were performed at 20 °C, after which residual analyte and degradation byproducts were extracted from polymer films with 1 mL of acetonitrile solution containing 12.1 mM tetrahydronaphthalene as an internal standard. Samples were then placed into a 1.5 mL GC auto-sample vial with PTFE septa top and analyzed immediately. In addition to simulant work being performed in a fume hood, personal protective equipment consisting of nitrile gloves, lab coat, chemical safety goggles were employed at all times during handling of chemical simulants.

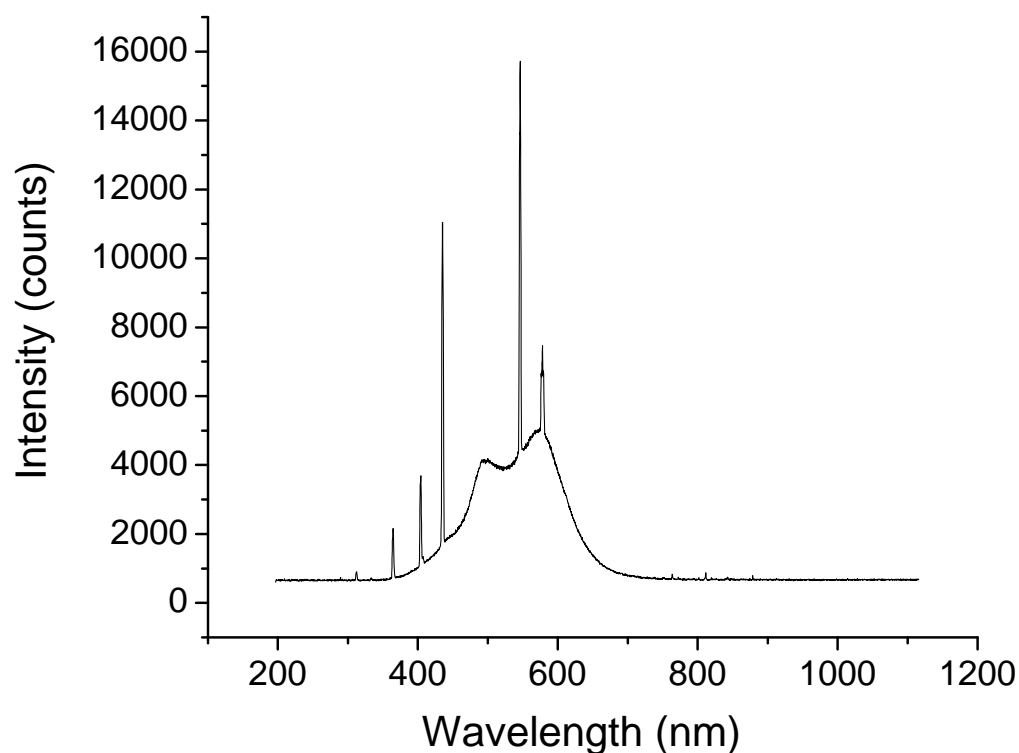


**Figure 4.16.** Emission spectrum of custom-built photochemical reactor.

Gas chromatography/mass spectroscopy (GC/MS) was employed to quantify analyte degradation. The GC/MS system consisted of an Agilent 7890A gas chromatograph equipped with an Agilent 5975C mass selective detector operating in electron ionization mode and an Agilent 7693A autoinjector. The column utilized was an Agilent HP-5MS (5% phenyl) methylpolysiloxane film. The carrier gas was helium with a flow rate of  $1 \text{ mL} \cdot \text{min}^{-1}$ . The injection volume was  $1 \text{ } \mu\text{L}$  with a split injection ratio of 20:1. The temperature program has an initial temperature of  $100 \text{ }^{\circ}\text{C}$  for one minute, then  $25 \text{ }^{\circ}\text{C}$  per min ramp to  $130 \text{ }^{\circ}\text{C}$  followed by a  $15 \text{ }^{\circ}\text{C}$  per min ramp to  $250 \text{ }^{\circ}\text{C}$  with a one minute post run hold at  $300 \text{ }^{\circ}\text{C}$ . The injection temperature, MS quad temperature, and source temperature were  $300$ ,  $150$  and  $230 \text{ }^{\circ}\text{C}$ , respectively. The solvent delay was set at

1.5 min and detector was set to scan a mass range of 20 to 350 m/z. Prior to comparison, GC/MS results were normalized by dividing the analyte peak area by the peak area of the internal standard, tetrahydronaphthalene.

## **5. INCORPORATION OF AMPHIPHILIC ADDITIVES INTO ELECTROSPUN FIBERS**

### **5.1. Overview**

Electrospinning was utilized to generate antimicrobial Nylon and polycarbonate fibers for potential applications including self-decontaminating fabrics, wound dressings, and filtration media. The effects of quaternary ammonium salt concentration on fiber morphology, diameter, and antimicrobial activity of the resulting fiber mats were investigated. Fibers were characterized utilizing scanning electron microscopy and X-ray photoelectron spectroscopy, while antimicrobial activity was evaluated against *Staphylococcus aureus*. The co-electrospinning of soluble quaternary ammonium biocides within polymeric solutions generated uniform fibers with diameters ranging from 91 to 278 nm for Nylon and 0.55 to 2.34  $\mu\text{m}$  for polycarbonate. Fiber morphology and diameter of the resulting fibers were shown to be dependent on polymer type and biocide concentration. A positive correlation between surface concentration of quaternary ammonium salts and antimicrobial activity was observed as fibers loaded with biocides exhibited up to a 7 log reduction of viable bacteria.

### **5.2. Prologue**

Bacterial contamination of clothing, air filters, and other assets is of constant concern, particularly due to the emergence of antibiotic resistant bacteria. Personnel in hospitals, health care clinics, and military settings are at particular risk.<sup>181</sup> Common

routes of exposure to infectious microbes occur through contact with clothing, bed sheets, and other fabrics contaminated with harmful bacteria, all of which would be greatly mitigated by the development of antimicrobial fabrics and materials.

In addition to the extensive research in the development of biocidal coatings and polymers,<sup>182</sup> there has been considerable work devoted to the creation of antimicrobial fibers with nano-scale diameters.<sup>104,183</sup> Fibers with nano-scale diameters exhibit extremely high surface area to volume ratios, which are highly desirable for antimicrobial surfaces since bacterial killing only occurs when bacteria come in physical contact with the surface.

Electrospinning has recently emerged as a promising method through which to develop novel polymeric fiber and fabric formulations for biological threat protection.<sup>105,106</sup> Electrospinning is an intricate process which utilizes electrostatic forces to create polymeric, ceramic, and sol-gel fibers with nano-scale diameters.<sup>104</sup> Numerous critical parameters must be controlled for the optimal production of fibers by electrospinning including but not limited to solvent selection, polymer concentration, applied voltage, and collection distance.<sup>184,185</sup> However, incorporation of additives, and particularly ionic molecules, into the electrospinning solution significantly affects fiber morphology and diameter.<sup>186–188</sup> As such, incorporation of ionic salts and additives into electrospinning solutions requires thorough investigation.

Contrasting approaches have been employed to create antimicrobial electrospun fibers, including fibers which leach biocide and fibers with persistent biocidal activity. Leaching biocidal materials comprised of antimicrobial nanofibers have been developed

that release biocidal molecules and compounds. Electrospun fibers which release nitric oxide over time have been developed with the aim to reduce infection resulting from implantable materials.<sup>189</sup> Chlorhexidine, a biocide, has also been incorporated into electrospun cellulose acetate fibers resulting in an antibacterial material which leached biocide and produced a notable zone of inhibition.<sup>190</sup> However, leaching biocides present opportunities for biocidal compounds to accumulate in environmental matrices and exhibit reduced antimicrobial activity over the lifetime of the material. On the other hand, antimicrobial activity does not diminish over time in persistent biocidal polymeric materials.

Many polymers have previously been utilized to create fibers through electrospinning and successful functionalization with biocidal additives has the potential to afford benefits for various applications due to the robust physical properties, safety and cost of the polymer systems. The focus of much electrospinning research has centered on Nylon and the effects of electrospinning conditions on the properties of resultant fibers.<sup>191</sup> Much work has also been performed in regard to optimal conditions for electrospinning polycarbonate due its attractive structural properties.<sup>192,193</sup> Recent literature has documented conditions by which to electrospin uniform fibers with micro- to nano-scale diameters for both Nylon and PC.<sup>192–195</sup>

Many approaches have been taken to develop antimicrobial polymer surfaces, of which, several can be tailored to electrospinning. Polymeric surfaces have been functionalized post application and successfully resulted in antibacterial surfaces.<sup>196,197</sup> Nylon 6,6 electrospun fibers exhibiting antimicrobial properties have likewise been



created through incorporation of *N*-halamine additives.<sup>195,198</sup> Benzyl triethylammonium chloride has been incorporated into electrospun polycarbonate fibers and found to improve antimicrobial activity.<sup>192</sup> Another post-treatment approach, while effective, requires continual recharging of a halamine biocide with dilute chlorine bleach in order to maintain antimicrobial behavior.<sup>199</sup> While these approaches can result in highly functionalized surfaces, each also requires additional processing steps thereby increasing application time, limiting practicality and increasing cost.

Alternatively, covalent incorporation of biocides in the polymer backbone has resulted in polymers exhibiting very promising antibacterial properties.<sup>200,201</sup> However, in doing so there is an alteration in the physical properties of the polymer in addition to a likelihood that a large proportion of the biocide will be buried within the bulk of the polymer, as opposed to at the surface where microbial interaction is likely to occur. Therefore, the most suitable approach for electrospinning investigations involves direct incorporation of a biocide into the polymer solution prior to application.

A solution-based additive approach is beneficial in that it allows one to maintain electrospinning conditions, of which there are numerous variables to optimize, from those developed for the unmodified polymer solution. Biocidal additive dispersion and distribution in the polymer matrix play integral roles in antimicrobial activity. An additive that is dispersed throughout the bulk of the coating is unlikely to be able to interact with surface residing microbes, resulting in reduced biocidal activity. Particular additives have the ability to preferentially orient at the polymer interface, and potentially increase antimicrobial activity per amount added.

Quaternary ammonium salts (QAS) are reported to mediate broad-spectrum bacterial killing through a cationic interaction with the cell membrane.<sup>147</sup> While numerous QAS are effective antimicrobial agents, the specific QAS available for selection in this study were greatly limited due to constraints resulting from incorporation of QAS into a polymer matrix for materials applications. The constraints result from several materials considerations such as ultimate polymer appearance, stability, adhesion and workability. Additionally, antibacterial activity of a surface is dependent on the relative concentration of biocide at the polymer-air interface, where interactions between bacteria and polymer occur.<sup>51</sup> Therefore, the interaction of the QAS with the polymer matrix must be considered. Recently, biocidal additives consisting of amphiphilic QAS have been developed which segregate to the air-polymer interface of polymeric coatings during curing when added directly to a polymer solution.<sup>49,50</sup> Furthermore, amphiphilic QAS have been effective in a variety of polymer matrices, including polyurethane and latex coatings.<sup>48,72</sup> In addition to surface segregation, QAS have also been used in combination with a unique germinant package as polymer additive and exhibited effective activity against *Bacillus anthracis*.<sup>103</sup>

Therefore, the incorporation of additives into the polymer solution for subsequent electrospinning is a logical approach to create functionalized electrospun fibers. Furthermore, the incorporation of surface segregating biocides into polymer solutions to create electrospun fibers has the potential to result in fibrous mats with high biocide surface concentration and high surface area material; however, surface segregation of biocidal additives in electrospun fibers has not been investigated. Herein, surface

segregating and biocidal capabilities of an amphiphilic QAS are compared to a less amphiphilic QAS in electrospun nylon 6, 6 (Nylon) and poly(Bisphenol A carbonate) (PC) fibers at various QAS loading concentrations. Increased amphiphilicity of QAS is expected to increase the surface concentration of QAS in electrospun fibers and improve biocidal activity.

### **5.3. Results and Discussion**

Numerous iterative formulations were required to optimize the electrospinning process for both PC and Nylon. It was qualitatively observed that incorporation of QAS into polymer solutions resulted in significant effects on the creation of electrospun fibrous mats. Consequently, more detailed investigations into the role of QAS in the formation of electrospun fibers were performed.

#### **5.3.1. Effect of QAS on Fiber Morphology and Fiber Diameter**

Fiber diameters of electrospun PC fibers were determined from SEM micrographs (Figure 5.2). Mean fiber diameters of electrospun polymer formulations are presented in Table 5.1. Control PC fibers which did not contain QAS exhibited an average fiber diameter of 2.34  $\mu\text{m}$ . A negative correlation was observed upon addition of QAS into the electrospinning solution as fiber diameter decreased with increasing QAS concentration. These results are in agreement with those presented in a recent work by Kim et al.,<sup>192</sup> in which the effects of benzyl triethylammonium chloride on PC fibers were examined. Herein, the incorporation of CTAB into PC solution at 1 wt% resulted in electrospun fibers with average diameters of 0.86  $\mu\text{m}$ . PC fibers loaded 5 and 10 wt% CTAB averaged diameters of 0.71 and 0.78  $\mu\text{m}$ , respectively. Loading of PC polymer solution

with 1 wt% C<sub>16</sub>EO<sub>1</sub> resulted in fibers with average diameter of 1.18  $\mu\text{m}$ . At 5 and 10 wt% C<sub>16</sub>EO<sub>1</sub>, the fiber diameters continued to decrease to 0.68 and 0.55  $\mu\text{m}$ , respectively. On comparison of the effects of the two QAS, 1 wt% loading of CTAB reduced PC fiber diameter to a greater extent than 1 wt% loading with C<sub>16</sub>EO<sub>1</sub>. However, further loading of C<sub>16</sub>EO<sub>1</sub> to 5 and 10 wt% in PC polymer solution resulted in fibers with diameters that decreased to a greater extent than comparable 5 and 10 wt% loadings of CTAB. It appears that while CTAB reaches a maximum influence on fiber diameter between 1 and 5 wt%, increasing incorporation of C<sub>16</sub>EO<sub>1</sub> resulted in decreased PC fiber diameter up to, and perhaps beyond, 10 wt% loading. This observation is due to the difference in molecular weight between CTAB (364 g/mol) and C<sub>16</sub>EO<sub>1</sub> (408 g/mol) and the resultant differences in molar concentration of additives. There is a 1.12 relative molar excess of CTAB to C<sub>16</sub>EO<sub>1</sub> for each comparable wt.% loading. Therefore, the saturation concentration of CTAB is reached at an apparently lower wt.% than the saturation concentration of C<sub>16</sub>EO<sub>1</sub>. The effects of fiber diameter for both QASs are thereby limited by their molar solubility.

**Table 5.1.** Average diameter of PC and Nylon fibers with increasing QAS concentrations.

<b>Polymer Sol.</b>	<b>Additive</b>	<b>Mean Fiber Diameter</b>
25 % PC	-	$2.34 \pm 0.64 \mu\text{m}$
25 % PC	1 wt% CTAB	$0.86 \pm 0.33$
25 % PC	5 wt% CTAB	$0.71 \pm 0.18$
25 % PC	10 wt% CTAB	$0.78 \pm 0.14$
25 % PC	1 wt% C <sub>16</sub> EO <sub>1</sub>	$1.18 \pm 0.37$
25 % PC	5 wt% C <sub>16</sub> EO <sub>1</sub>	$0.68 \pm 0.22$
25 % PC	10 wt% C <sub>16</sub> EO <sub>1</sub>	$0.55 \pm 0.19$
15 % Nylon	-	$91 \pm 16 \text{ nm}$
15 % Nylon	1 wt% CTAB	$193 \pm 50$
15 % Nylon	5 wt% CTAB	$234 \pm 54$
15 % Nylon	10 wt% CTAB	$278 \pm 89$
15 % Nylon	1 wt% C <sub>16</sub> EO <sub>1</sub>	$203 \pm 40$
15 % Nylon	5 wt% C <sub>16</sub> EO <sub>1</sub>	$175 \pm 37$
15 % Nylon	10 wt% C <sub>16</sub> EO <sub>1</sub>	$253 \pm 67$

The diameter of PC nanofibers created by electrospinning depend on a variety of factors,<sup>202</sup> of which solution properties are variables. Of the solution properties, an electrospinning model has determined that solution conductivity and viscosity exhibit strong roles in determining the final fiber diameter, while surface tension plays a minor role.<sup>203</sup> The addition of QAS additives to a polymer solution does not alter each of these solution properties to the same degree. For the electrospinning of polystyrene fibers, the addition of both dodecyltrimethylammonium bromide and tetrabutylammonium chloride were found to significantly increase the solution conductivity, result in only minor decreases in surface tension at the highest loading concentrations, and have no effect on viscosity.<sup>204</sup> Other studies provide supplemental evidence that incorporation of ionic

salts, triethylbenzylammonium chloride, into electrospinning polymer solution increase solution conductivity, while negligibly affecting surface tension and viscosity.<sup>187,188,205</sup> The negligible role of surface tension found in the literature is confirmed for the PC solutions employed herein as surface tension of the polymer solutions did not correlate with fiber diameter (Figure 5.1).

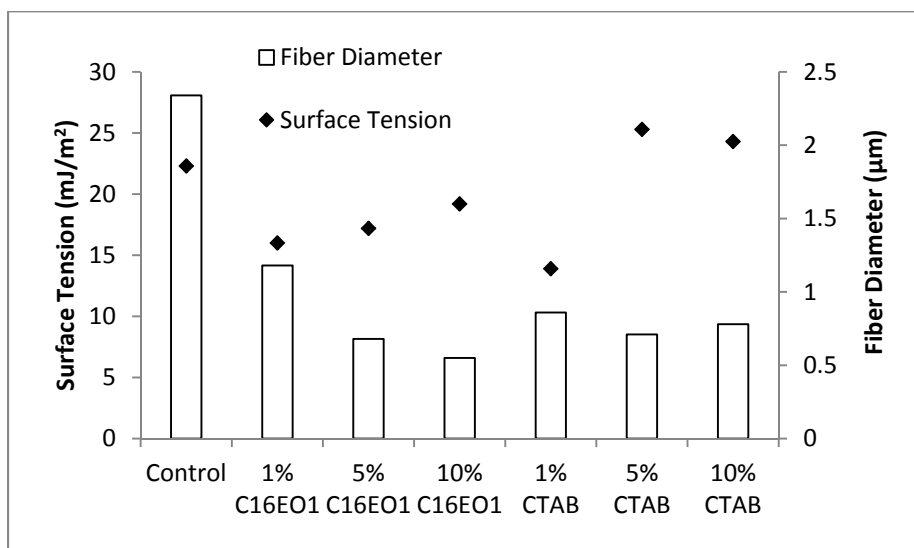


**Figure 5.1.** Comparison of average surface tension and average fiber diameter of PC/QAS solutions.

Therefore, the only significant solution property affecting fiber diameter upon QAS incorporation into polymer solutions must be the solution conductivity. This is supported by trends observed in a previous work that incorporated benzyltriethylammonium chloride, a QAS, into polycarbonate solution in chloroform.<sup>192</sup> Greater concentration of QAS causes increased solution conductivity, which results in increased charge density on the polymer jet during electrospinning. Greater charge

density increases electrostatic repulsion of the polymer jet, thereby facilitating more whipping and stretching to form fibers with smaller diameters.

Incorporation of QAS was found to contribute to changes in PC fiber morphology. As concentrations of both CTAB (Figure 5.2b-d) and C<sub>16</sub>EO<sub>1</sub> (Figure 5.2e-g) were increased from 1 to 10 wt%, the surface texture of the PC fibers became increasingly smooth relative to the wrinkled texture exhibited by PC fibers formulated without QAS additives (Figure 5.2a). Wrinkled morphology has been observed in electrospun fibers due to continued solvent evaporation following fiber formation and subsequent fiber shrinkage.<sup>206</sup> While electrospun fibers with very small diameters inherently exhibit very high surface area to volume ratios, an increase in surface roughness results in a further increased ratio. The decrease in fiber roughness with increasing concentration of QAS resulted from increased solution conductivity due to the ionic effects of QAS. Increase in solution conductivity has been demonstrated to affect surface morphology.<sup>188</sup> As such, the increase in QAS concentration in PC creates fibers with smoother texture as a side-effect of decreased fiber diameter in that small fibers, which have higher surface area to volume ratios, allow for complete solvent evaporation during jet acceleration and whipping toward the target. Therefore, it is more likely for the PC fiber to form without entrapped solvent when QAS is added, avoiding continued evaporation after solidifying, and thus resulting in a smooth surface.

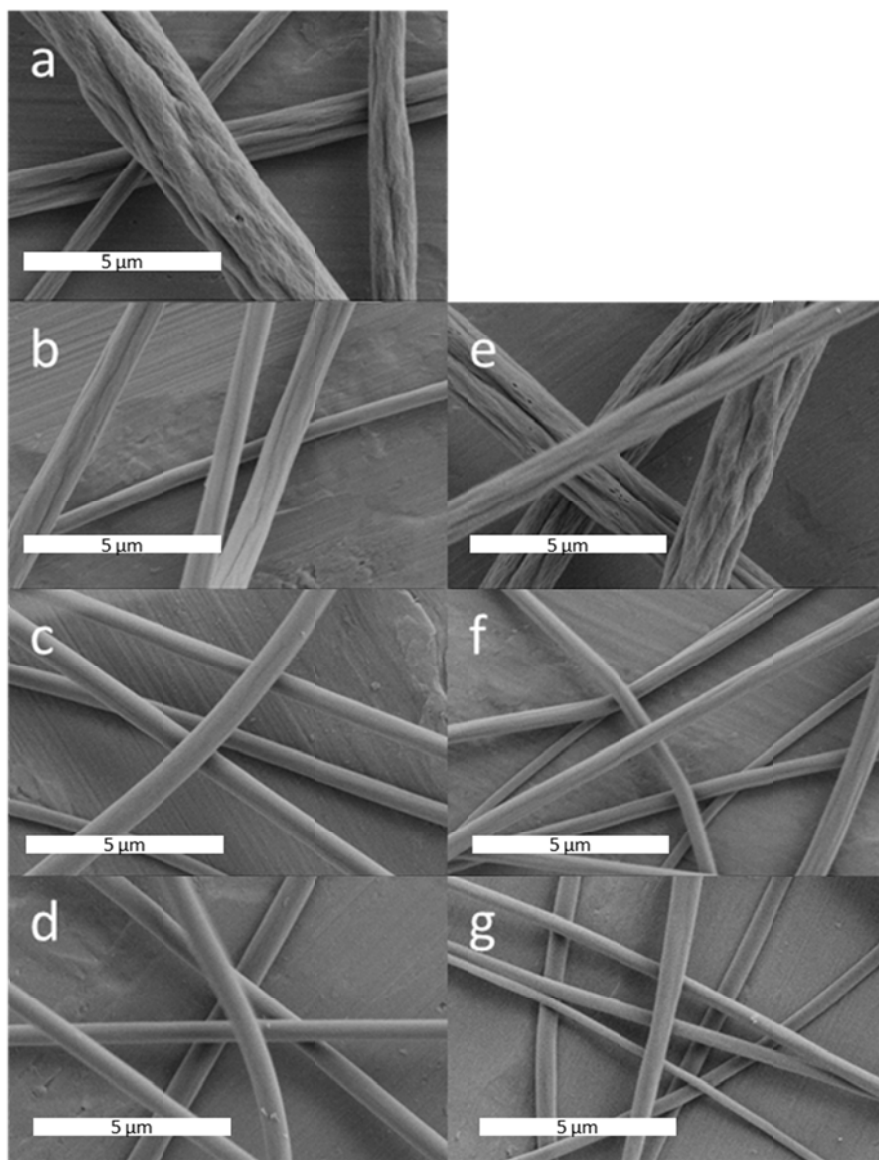


**Figure 5.2.** SEM micrographs (10,000x mag.) of electrospun PC fibers containing no additive (a), 1 wt% CTAB (b), 5 wt% CTAB (c), 10 wt% CTAB (d), 1 wt% C<sub>16</sub>EO<sub>1</sub> (e), 5 wt% C<sub>16</sub>EO<sub>1</sub> (f), and 10 wt% C<sub>16</sub>EO<sub>1</sub> (g).

Nylon polymer solutions were also loaded with QAS, electrospun and subsequently analyzed. Overall, electrospinning of Nylon from a 15% solution produced fibers with very small diameters within a relatively narrow range (Table 5.1). Without



QAS additives, an average fiber diameter of 91 nm was achieved for Nylon fibers. Incorporation of both CTAB and C<sub>16</sub>EO<sub>1</sub> increased electrospun Nylon fiber diameters which can be qualitatively observed in Figure 5.3. Specifically, the incorporation of CTAB at 1, 5, and 10 wt% in Nylon resulted in increasing fiber diameters of 193, 234, and 278 nm, respectively. Incorporation of C<sub>16</sub>EO<sub>1</sub> at 1, 5, and 10 wt% resulted in average fiber diameters of 203, 175, and 253 nm, respectively. For both QAS additives, standard deviation of the fiber diameter measurements increased as average fiber diameter increased, indicating greater fiber diameter dispersity for each respective fibrous mat.

Polyamides dissolved in formic acid are ionized, thus resulting in a polyelectrolyte solution, of which further increases in ionic strength of the solvent, such as through the addition of QAS, diminishes the electrostatic interactions (i.e. increases electrostatic screening).<sup>207</sup> Effects on fiber diameter from increasing solution conductivity are diminished by electrostatic screening in the polyelectrolyte polymer solution. It has been shown that incorporation of a comparable QAS, benzyltrimethylammonium chloride (BTAC), at 1 wt% in a solution of nylon 6,6 in formic acid increased both solution conductivity of nylon 6,6 solutions from 4.1-4.3 mS/cm to 6.5-8.1 mS/cm and fiber diameters.<sup>208</sup> For another electrospinning polymer solution, fiber diameters of electrospun poly( $\epsilon$ -caprolactone)-acetic acid solution increased with increasing pyridine concentration despite increasing solution conductivity.<sup>209</sup> Further, Mit-Uppatham and coworkers<sup>210</sup> demonstrated that increasing concentrations of NaCl, LiCl, and MgCl<sub>2</sub> increased nylon solution viscosity, solution

conductivity, and electrospun fiber diameters. Increasing solution conductivity facilitates decreased fiber diameters while increased solution viscosity contributes to larger fiber diameters.<sup>203</sup> Indeed, viscosity of Nylon solutions increased with increasing concentration of CTAB (Table 5.2). Increased solution viscosity effectively causes the fiber to resist elongation and stretching once the polymer is extruded from the syringe tip. Furthermore, increased solution viscosity causes a greater mass flow of polymer which reduces the electrostatic charge density of the polymer jet since the volume of polymer jet is increased. Charge density plays a prominent role in intra-fiber Coulombic repulsion which causes whipping and stretching. Therefore, if charge density is reduced, less whipping and stretching occur and fiber diameters remain relatively large.<sup>210</sup> Therefore, the increase in nylon fiber diameters upon incorporation of QAS resulted from the combined contributions of increased viscosity and electrostatic screening overcoming the contribution of increased solution conductivity.

**Table 5.2.** Selected solution properties of 15 wt% Nylon in formic acid solution containing CTAB.

CTAB in Nylon (wt%)	Surface Tension (mJ/m <sup>2</sup> )	Viscosity (cP)
0	40.1 ± 0.2	1179 ± 4
1	39.9 ± 0.1	1458 ± 2
5	38.0 ± 0.5	1512 ± 2
10	36.2 ± 0.7	1638 ± 2

The effects of QAS on fiber morphology and surface texture of electrospun Nylon fibers were determined through SEM analysis (Figure 5.3). Nylon fibers electrospun

without QAS (Figure 5.3a) exhibited a cylindrical morphology and smooth texture, both of which were maintained upon incorporation of CTAB at concentrations 1, 5, and 10 wt%. At 10 wt% CTAB loading, a few ribbon shaped fibers were also observed dispersed among the fibrous mat of primarily cylindrical fibers (Figure 5.3d). The ribbon shapes, which can also be described as flat tubes, may result from an initial formation of a solid polymer skin on the electrospun fiber, which accumulates repulsive charges at two opposite points around the cylinder causing lateral stretching. Such behavior has been documented and described previously.<sup>206</sup> The lateral stretching in combination with diffusive solvent escape caused the tube to collapse into an ultimate ribbon shape.<sup>206</sup> Such behavior was only observed in the highest (10 wt%) QAS loaded fibers perhaps because the high concentration of QAS effectively reduces Nylon solubility, thereby accelerating the formation of polymer solid as a skin in the electrospun jet. Similar trends in fiber morphology were observed in Nylon fibers loaded at 10 wt% with either C<sub>16</sub>EO<sub>1</sub> or CTAB into the polymer solution. Nylon fibers loaded with 10 wt% C<sub>16</sub>EO<sub>1</sub> exhibited rough surface features on the order of 5-20 nm (Figure 5.3g). Nylon fibers at 10 wt% CTAB exhibited similar effects, but to a lesser degree than C<sub>16</sub>EO<sub>1</sub> loaded Nylon, and typically the nano-roughness was observed to only occur where two or more fibers are in contact with one another at intersections.

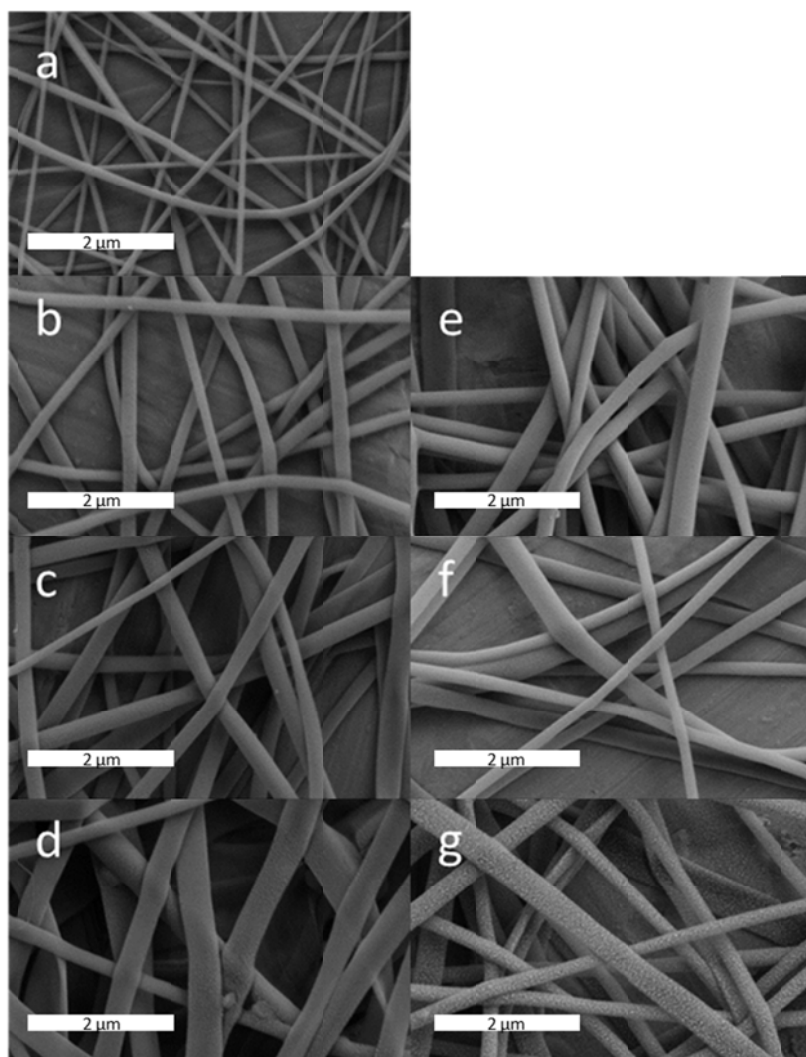


**Figure 5.3.** SEM micrographs (20,000x mag.) of electrospun Nylon fibers containing no additive (a), 1 wt% CTAB (b), 5 wt% CTAB (c), 10 wt% CTAB (d), 1 wt% C<sub>16</sub>EO<sub>1</sub> (e), 5 wt% C<sub>16</sub>EO<sub>1</sub> (f), and 10 wt% C<sub>16</sub>EO<sub>1</sub> (g).

Upon comparison of the two polymer systems, incorporation of QAS in polymer solution resulted in opposite effects on fiber diameter and fiber morphology between PC and Nylon. While Nylon fibers increased in diameter with increasing QAS concentration, the diameters of PC fibers decreased. Electrospun fiber diameters are critically affected by polymer solution electrical conductivity, which in turn, is directly

affected by salt concentration. Incorporation of salts into organic polymer solutions is known to result in decreased electrospun fiber diameters through a combination of increased solution conductivity and screening electrostatic repulsions.<sup>211</sup> Also, incorporation of salts has been demonstrated to affect polymer solution viscosity. Recent literature has also demonstrated that increasing salt concentration in an aqueous electrospinning solution tends to result in slightly larger fiber diameters.<sup>187</sup> Furthermore, increasing QAS concentration in PC fibers caused the fibers to become smoother and less textured. While at the highest QAS loading concentration in Nylon, fibers demonstrated nano-roughness features and ribbon shaped fibers were dispersed throughout the nonwoven mat. Therefore, effects of QAS on solution conductivity were concluded to be responsible for the observed trends in fiber diameter and surface morphology.

The contrasting effects of the incorporation of QAS into polycarbonate and Nylon polymer solutions result from different solution properties dominating fiber formation. In the case of polycarbonate, the change in solution conductivity on the polymer solution dominates the morphological changes observed on the electrospun polymers; while changes in solution viscosity from QAS incorporation dominate the ultimate appearance and size of electrospun fibers of Nylon polymer solutions.

### **5.3.2. Bacterial Challenge**

Electrospun PC and Nylon fibers containing QAS were subjected to bacterial challenges against *S. aureus*. The average log reduction of *S. aureus* for each fiber formulation is presented in Figure 5.4. The control PC fibers did not exhibit any reduction in *S. aureus* and each PC fiber loaded with CTAB demonstrated only minor

antibacterial activity (0.33 log reduction). No bacterial reductions occurred on 1 and 5% C<sub>16</sub>EO<sub>1</sub> PC fibers; however, a significant 7 log reduction of *S. aureus* occurred on 10 wt% C<sub>16</sub>EO<sub>1</sub> PC fibers. Incorporation of QAS in PC did not result in fibers with significant antimicrobial activity, except at the highest loading of amphiphilic QAS suggesting that the QAS do not surface segregate effectively in the PC electrospinning solution.

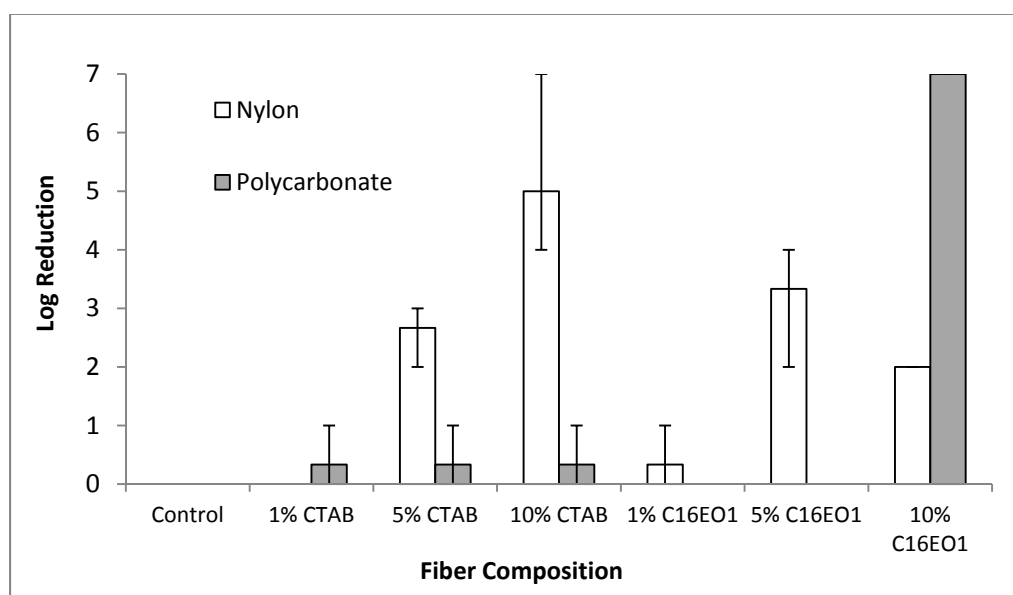


**Figure 5.4.** Average log reduction *S. aureus* on Nylon and PC electrospun fibers containing quaternary ammonium salts.

No relationship between Gram-positive bacterial reduction and fiber diameter of the PC electrospun polymers was observed. The smallest PC fiber diameter occurred in the 10% C<sub>16</sub>EO<sub>1</sub> PC fibers which also demonstrated 7 log reduction of *S. aureus*;

however, the 5% C<sub>16</sub>EO<sub>1</sub> PC and 10 % CTAB PC fibers also exhibited relatively small diameters, yet neither demonstrated significant reduction of *S. aureus*.

Electrospun Nylon fibers containing QAS were also subjected to Gram-positive bacterial challenges against *S. aureus* (Figure 5.4). The control, consisting of unmodified electrospun Nylon, did not exhibit antibacterial activity. Nylon fibers that contained CTAB demonstrated significant log reductions at 5 and 10 wt% loadings and Nylon fibers containing C<sub>16</sub>EO<sub>1</sub> exhibited antimicrobial activity for each loading concentration. Similar to the CTAB loaded Nylon fibers, C<sub>16</sub>EO<sub>1</sub> loaded Nylon fibers demonstrated the greatest activity against *S. aureus* at 5 and 10 wt% QAS with average log reductions of 3.3 and 2, respectively. Increased CTAB concentration in Nylon fibers led to linear improvement in reduction of Gram-positive bacteria, while Nylon fibers loaded with C<sub>16</sub>EO<sub>1</sub> exhibited the greatest bacterial reduction at 5 wt%. Loading of C<sub>16</sub>EO<sub>1</sub> beyond 5 wt% reduces surface concentration of biocide as aggregation may be occurring, resulting in a reduction of antibacterial activity. Additionally, fiber diameter may become a factor with increased C<sub>16</sub>EO<sub>1</sub> loading as the largest fiber diameters of the Nylon based fibers occurred 10 wt% C<sub>16</sub>EO<sub>1</sub> loading. Larger fiber diameters equate to lower surface area per volume of polymer which can cause reduced antimicrobial activity, particularly for a surface active material. Decreased fiber diameter has the potential to increase antimicrobial activity through increased total surface area of polymer. However, no correlation was found between diameter of PC and Nylon fibers and antimicrobial activity when surface area was calculated from the mass and fiber diameter of each fibrous mat and compared to bacteria log kill (Table 5.3).

**Table 5.3.** Comparison of total fiber surface area of fibrous mats on 1.88 cm<sup>2</sup> coupons to bacterial log kill.

Sample	Mat Avg. Mass (mg)	Fibrous Volume (cm <sup>3</sup> ) <sup>a</sup>	Avg. Fiber Diameter (cm)	2/r (cm <sup>-1</sup> ) <sup>b</sup>	Surface Area (cm <sup>2</sup> ) <sup>b</sup>	Log Kill
Nylon Control	1.2	1.10E-03	9.10E-06	4.40E+05	483.92	0
Nylon 1% C <sub>16</sub> EO <sub>1</sub>	0.7	6.42E-04	2.03E-05	1.97E+05	126.54	0.3
Nylon 5% C <sub>16</sub> EO <sub>1</sub>	0.8	7.34E-04	1.75E-05	2.29E+05	167.76	3.3
Nylon 10% C <sub>16</sub> EO <sub>1</sub>	0.7	6.42E-04	2.53E-05	1.58E+05	101.53	2
Nylon 1% CTAB	0.7	6.42E-04	1.93E-05	2.07E+05	133.10	0
Nylon 5% CTAB	0.9	8.26E-04	2.34E-05	1.71E+05	141.14	2.6
Nylon 10% CTAB	0.9	8.26E-04	2.78E-05	1.44E+05	118.80	4.6
PC Control	1.3	1.08E-03	2.34E-04	1.71E+04	18.52	0
PC 1% C <sub>16</sub> EO <sub>1</sub>	1.0	8.33E-04	1.18E-04	3.39E+04	28.25	0
PC 5% C <sub>16</sub> EO <sub>1</sub>	0.9	7.50E-04	6.80E-05	5.88E+04	44.12	0
PC 10% C <sub>16</sub> EO <sub>1</sub>	1.0	8.50E-04	5.50E-05	7.27E+04	61.82	7
PC 1% CTAB	1.4	1.17E-03	8.60E-05	4.65E+04	54.26	0.3
PC 5% CTAB	0.9	7.50E-04	7.10E-05	5.63E+04	42.25	0.3
PC 10% CTAB	0.9	7.50E-04	7.80E-05	5.13E+04	38.46	0.3

<sup>a</sup> Density: nylon = 1.09 g/cm<sup>3</sup>; PC = 1.20 g/cm<sup>3</sup>.

<sup>b</sup>For a cylinder of infinite length (L), the surface area ( $2\pi rL$ ) to volume ( $\pi r^2L$ ) ratio simplifies to  $2/r$ , in which  $r$  is fiber radius. Surface area is then calculated by multiplying fibrous volume by  $2/r$ .

### 5.3.3. Surface Concentration of QAS (XPS)

Surface concentrations of QAS in Nylon fibers were investigated utilizing XPS analysis to elucidate the variation in antibacterial activity with QAS loading. Specifically, the concentration of QAS at the surface was determined by comparing the relative area of the quaternary ammonium N 1s signal at a binding energy of 402 eV for each sample. It has been shown that amphiphilic QAS additives in solvent-cast polyurethane and latex paint matrices spontaneously segregate to the polymer-air interface.<sup>49</sup> Yet, this behavior has not been investigated in electrospun polymer fibers. Table 5.4 compares the observed surface concentration of QAS to expected surface concentration if the QAS were evenly distributed throughout the entire volume of the fiber. Of fibers loaded with CTAB, the maximum surface concentration of QAS occurred in the 10 wt% CTAB. Yet in the C<sub>16</sub>EO<sub>1</sub> loaded fibers, the maximum QAS



concentration occurred in the 5 wt% C<sub>16</sub>EO<sub>1</sub>. The calculated theoretical values (% N calculated) demonstrate that if the QAS were evenly distributed throughout the polymer, an increasing linear trend of % N would result from QAS loading from 1 to 10 wt%. While such a trend was observed for CTAB loaded Nylon fibers, the C<sub>16</sub>EO<sub>1</sub> fibers exhibited different behavior.

**Table 5.4.** Comparison of observed QAS surface concentration with calculated surface concentration assuming even dispersion. Concentration factor was determined by dividing % N observed by % N calculated.

<b>Fibers</b>	<b>% N observed</b>	<b>% N calculated</b>	<b>Conc. Factor</b>
Control	0.00	0	NA
1% CTAB	0.00	0.04	0.00
5% CTAB	0.44	0.22	2.03
10% CTAB	0.76	0.43	1.76
1% C <sub>16</sub> EO <sub>1</sub>	0.00	0.04	0.00
5% C <sub>16</sub> EO <sub>1</sub>	1.33	0.19	6.87
10% C <sub>16</sub> EO <sub>1</sub>	0.55	0.39	1.42

It is clear that C<sub>16</sub>EO<sub>1</sub> does not simply disperse evenly between the bulk and surface of the fibers. In fact, C<sub>16</sub>EO<sub>1</sub> orients at the surface of the fiber as opposed to the bulk. The concentration factor (obsd/calc) clearly demonstrates the degrees to which the QAS preferentially orient at the Nylon-air interface rather than evenly distribute throughout polymer volume in the 5 and 10 wt% QAS (CTAB and C<sub>16</sub>EO<sub>1</sub>) loaded fibers. Nylon fibers loaded with 5 and 10 wt% CTAB demonstrated surface concentration factors of 2.03 and 1.76, respectively. In comparison, 5 and 10 wt% C<sub>16</sub>EO<sub>1</sub> Nylon fibers

exhibited concentration factors 6.87 and 1.42, respectively. For both CTAB and C<sub>16</sub>EO<sub>1</sub>, a loading concentration of 5% resulted in the greatest improvement in surface concentration. Overall, the greatest surface concentration occurred in the 5% C<sub>16</sub>EO<sub>1</sub> Nylon fibers (Figure 5.5).

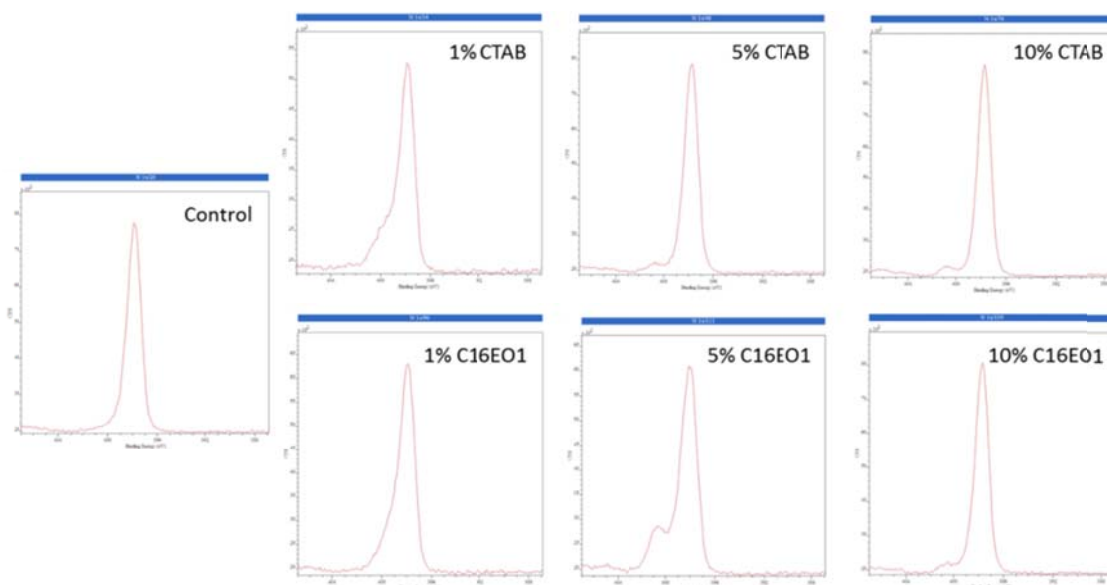


**Figure 5.5.** XPS N1s region scans demonstrating nitrogen (398 eV) and quaternary ammonium nitrogen (402 eV) in Nylon fibers containing QAS.

Therefore, the critical micelle concentration (CMC) of C<sub>16</sub>EO<sub>1</sub> in Nylon polymer solution was exceeded at some point between 5% and 10% loading, as surface segregation of C<sub>16</sub>EO<sub>1</sub> was greater at 5% than at 10%. C<sub>16</sub>EO<sub>1</sub>, as an amphiphilic additive, preferentially forms micelles instead of aligning at the polymer-air interface beyond a certain concentration, the CMC. The formation of micelles inherently minimizes surface energy as well as solvophobic interactions of the additives and

therefore would facilitate reduced surface concentration as amphiphilic additive loading is increased beyond the CMC.

An overlay of *S. aureus* average log reduction and QAS surface concentration in electrospun Nylon fibers is shown in Figure 5.6. The plot clearly demonstrates the relationship between surface concentration of QAS and the antibacterial activity of the Nylon fibers. Overall, antimicrobial activity correlates well with quaternary ammonium nitrogen surface concentration. Considering all the samples together, antimicrobial activity of the 5% C<sub>16</sub>EO<sub>1</sub> Nylon does not scale with surface concentration of QAS to the same degree as Nylon samples containing CTAB. Yet antimicrobial activity does scale with surface concentration relative to other fibers loaded with the same QAS. Fibers loaded with CTAB must be considered independent of C<sub>16</sub>EO<sub>1</sub> in this regard as the QAS do differ in chemical composition and therefore also differ in antimicrobial efficacy. Considering this, surface concentration does correlate with surface concentration. The correlation between surface concentration of quaternary ammonium and anti-bacterial activity occurred in both CTAB and C<sub>16</sub>EO<sub>1</sub> loaded Nylon fibers.

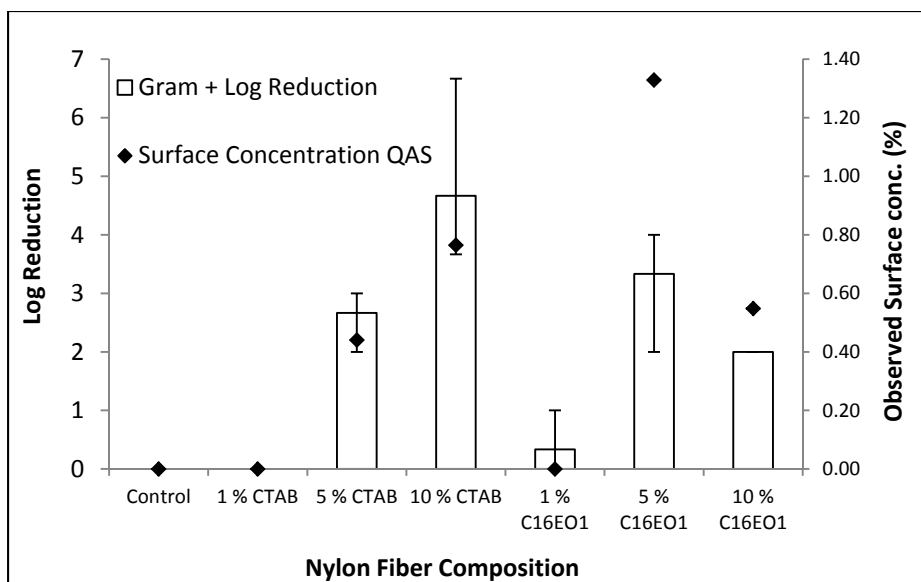


**Figure 5.6.** Comparison of Gram-positive log reduction and surface concentration of QAS in Nylon fibers.

#### 5.4. Summary

This study investigated the difference between CTAB and C<sub>16</sub>EO<sub>1</sub> in Nylon and PC electrospun fibers. In general, both CTAB and C<sub>16</sub>EO<sub>1</sub> affected each respective polymer system similarly. Additionally, regardless of whether CTAB or C<sub>16</sub>EO<sub>1</sub> was used, incorporation of QAS resulted in opposite effects on fiber diameter and morphology in PC compared to those in Nylon. Increasing QAS concentration in the polymer solutions was found to increase Nylon fiber diameters and decrease PC fiber diameters. The incorporation of CTAB into Nylon fibers resulted in incrementally increasing surface concentration of quaternary ammonium and anti-bacterial activity. Incorporation of C<sub>16</sub>EO<sub>1</sub> into Nylon, on the other hand, demonstrated maximum surface concentration and anti-bacterial activity in the 5 wt% loaded fibers. Clearly, different modes of additive dispersion are occurring. The most significant factor affecting

antibacterial activity of Nylon fibers against Gram-positive bacteria was surface concentration of quaternary ammonium additives. This work has demonstrated surface concentration of amphiphilic QAS additive in electrospun Nylon fibers. From this, future biocidal additive research for electrospun fibers should be focused on the correlating mechanism of action with biocidal efficiency in electrospun fibers.

## **5.5. Experimental Methods**

### **Materials**

All solvents were reagent grade and used without further purification. Purchased starting materials were used without further purification. High molecular weight Nylon 6,6 ( $M_n \sim 60,000$ ), poly(Bisphenol A carbonate) pellets ( $M_w \sim 64,000$ ), and cetyltrimethylammonium bromide (CTAB) were purchased from Sigma Aldrich (St. Louis, MO) and used as received.

### **Synthesis of quaternary ammonium biocides**

$C_{16}EO_1$ , a surface segregating QAS, was prepared following previously described procedures.<sup>49</sup> Briefly, 7.8 mmol phosphorous tribromide was added drop-wise to a solution of 15.6 mmol 2-methoxyethanol maintained at 0 °C. The solution was allowed to equilibrate to room temperature, and then heated to 90 °C when the solution turned yellow. After the solution was allowed to cool, 6 mL of 10%  $NaHCO_3$  was added. The solution was extracted with diethyl ether and dried with  $MgSO_4$ . This product was reacted with *N,N*-dimethylhexadecylamine under nitrogen in ethanol at 83 °C for 24 h.

The resulting C<sub>16</sub>EO<sub>1</sub> product was recrystallized to form an off-white powder. The structures of the resulting product (C<sub>16</sub>EO<sub>1</sub>) and CTAB are shown in Figure 5.7.

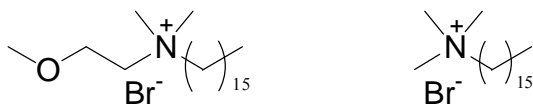


**Figure 5.7.** Chemical structures of C<sub>16</sub>EO<sub>1</sub> (left) and CTAB (right).

### Polymer preparation

Nylon solutions (15 wt%) were prepared by mixing separately prepared solutions of Nylon in formic acid (4 mL) and QAS in formic acid (1 mL) to result in 0, 1, 5, and 10 wt% QAS relative to Nylon. Preparation of comparable PC solutions (25 wt%) were made by mixing solutions of PC in methylene chloride (4 mL) with QAS in DMF (1 mL). A Brookfield DV-II Pro+ viscometer equipped with RV-2 spindle at 20 rpm was utilized for polymer solution viscosity. Polymer solution surface tensions were determined by drop shape analysis on a VCA Optima by AST Products, Inc.

### Electrospinning Apparatus

A custom electrospinning apparatus consisting of a Bertan Series 205B high voltage power supply from Bertan Associates, Inc. and a NE-300 New Era syringe pump from New Era Pump Systems, Inc. was employed to fabricate electrospun fibers. A 10 mL syringe was filled with polymer solution, equipped with a flat-tipped stainless steel 22-gauge needle (Jensen Global, Santa Barbara, CA) and loaded into the syringe pump.

The power supply was connected to the needle tip, set to 15 kV and the syringe pump flow rate was set to 15  $\mu\text{L}/\text{min}$ . Fibers were collected on a grounded target covered in aluminum foil set perpendicular to the syringe at a distance of 15 cm from the needle tip. Electrospinning was terminated after a minimum of 450  $\mu\text{L}$  of polymer solution was dispensed from the syringe.

### **SEM Analysis**

Prior to SEM analysis, the electrospun samples were coated with a 3 nm layer of gold using a Cressington 108 auto sputter coater equipped with a Cressington MTM20 thickness controller. A Carl Zeiss SMT Supra55 scanning electron microscope (SEM) was utilized to verify fiber formation and analyze morphology of electrospun polymers. Accelerating voltage was set between 3 and 5 kV. Fiber diameters were measured using Image J analysis software from which average fiber diameters were calculated ( $n \geq 100$ ).

### **XPS analysis**

XPS analysis was performed using a Kratos Axis-Ultra DLD XPS spectrometer (Kratos, Manchester, U.K.) at the National Institute of Standards and Technology (NIST; Gaithersburg, MD). A 300  $\mu\text{m}$  x 700  $\mu\text{m}$  spot size was analyzed. For each sample, a low resolution survey was performed with a pass energy of 160 eV and step size of 0.5 eV. High resolution region scans were performed for all samples, each with a pass energy of 20 eV and step size of 0.1 eV. Spectra were analyzed using CasaXPS software.

The concentration of QAS at the surface was determined from calculations based on the ammonium N1s signal (402 eV). The XPS ammonium signal was corrected to represent the QAS molecule by multiplying the percentage of the total XPS signal from quaternary ammonium N by the weight percent of N in the QAS molecule. The expected surface concentration was calculated by multiplying weight percent of N in the QAS molecule by the loading percent (0.01, 0.05, and 0.10). Values of respective loadings were compared to determine surface concentrating factor (observed/expected).

### **Antimicrobial evaluation**

*Staphylococcus aureus* (*S. aureus*, ATCC 25923) was utilized in bacterial challenges for the electrospun fibrous mats. Bacteria were grown at 37 °C. Log phase cells were harvested by centrifugation, counted on a hemocytometer using phase contrast microscopy, pelleted by centrifugation at 4000 xg for 10 min, and resuspended in phosphate buffered saline at a concentration of  $1 \times 10^9$  CFU/mL. To prevent desiccation of the bacteria during testing, a hydration chamber was prepared consisting of a sterile 76 x 76 mm gauze pad placed in the bottom of a sterile 150 x 15 mm Petri dish. The gauze pad was saturated with 5 mL of sterile water and the test samples placed on top. A 10  $\mu$ L aliquot containing  $1 \times 10^7$  bacteria was added to each test mat (approx. 188 mm<sup>2</sup> disc coated with 1 mg polymer fibers), and then placed in a hydration chamber at room temperature. After 2 h of incubation, bacteria were recovered by placing the mat in a tube containing 5 mL sterile Lethen media, followed by 30 sec of vortexing. Serial dilutions were carried out, and incubated for 18 h at 37 °C with agitation. Following



incubation, the cultures were examined for the presence of turbidity, indicating bacterial growth. Each mat was tested in triplicate. Log kill was determined by the following:  $\text{Log kill} = 7 - \text{highest dilution exhibiting bacterial growth}$ . All bacterial challenge procedures were conducted using standard aseptic techniques in a BSL-2 hood.

## 6. CONCLUSIONS

In summary, an extensive array of investigations were performed to yield greater fundamental understanding of the distribution behavior and mode of action of amphiphilic additives in polyurethane matrices. A series of amphiphilic polyoxometalate and fullerene species were synthesized, their polymeric distribution characterized, and mechanism of surface reactivity determined. It was confirmed that the quaternary ammonium nitrogen and the ethylene oxide moieties of QAS were coordinated to the POM core, thus resulting in a QAS-POM conjugate molecule that presents an alkyl tail hydrophobic exterior to the surrounding environment. The quantities of QAS that were coordinated to each POM molecule were found to be dependent on chemical composition of QAS. These insights into the coordination chemistry between QAS and POM are the most detailed to date. Significant evidence of the electrostatic coordination of the ammonium ion and the ethylene oxide tails to the POM core was directly presented. Due to the coordination and intermolecular coordination, QAS-POMs demonstrated unique dispersion behavior in polymers that was concluded to result from solvophobic induced surface segregation dependent on the properties of both QAS and the polymer matrix.

The amphiphilic modification of  $C_{60}$  improved solubility and dispersion in polymer films compared to neat  $C_{60}$ , which was identified to accumulate into crystalline aggregates. The polyurethane films containing amphiphilic  $C_{60}$  presented a

photocatalytic mode of action for the decomposition of CWA simulants residing at the air-surface interface. This represents a novel report of oxidation of neat chemical simulants residing on a polymer surfaces that contain  $C_{60}$  species as a decontaminant. Further, the elucidation of the mechanism of reaction represents a significant contribution to the scientific field.

A preliminary investigation of amphiphilic additives incorporated into electrospun polymers led to the conclusion that amphiphilic facilitated surface segregation does not occur during the electrospinning process. The primary factor that contributes to the lack of surface segregation is the rapid flash evaporation of solvent during electrospinning, which diminishes the ability of additive to diffuse to thermodynamic equilibrium to the polymer-air interface. Due to these findings, researchers developing functionalized nanofibers through electrospinning are focusing their resources on incorporation of additives other than amphiphilic molecules.

The approaches and methodologies that were employed to investigate the behavior of QAS-POM and  $EO_3-C_{60}$  additives serve as a framework for the future study of self-decontaminating nanocomposite systems. On-going research in self-decontaminating coatings is concentrated on accounting for the entire mass balance of decontamination reactions in order to thoroughly elucidate the mechanisms of reaction. Although it was found that QAS-POM exhibited hydrophobic character instead of the intended amphiphilic, the hydrophobic intermolecular interactions that dominate the particle dispersion of QAS encapsulated POMs in polyurethane matrices can be leveraged to incorporate beneficial properties into coatings, such as surface roughness

modulate gloss and water roll off angle. Further, the insights gained herein will guide future research of amphiphilic QAS encapsulated POMs through alternative synthetic routes.

Overall, this work represents a comprehensive and interdisciplinary scientific contribution that has resulted in the greater fundamental understanding of the distribution behavior and surface reactivity of novel reactive amphiphilic additives for self-decontaminating materials. A comprehensive analysis of additive behavior which spanned molecular characterization, polymer distribution, and surface reactivity was presented. The integrated multidisciplinary topics covered in this work encompassed the interdisciplinary range of synthetic chemistry, molecular spectroscopy, intermolecular interactions, polymer dynamics, surface chemistry, and heterogeneous catalysis.

## BIBLIOGRAPHY

- (1) Yang, Y. C.; Baker, J. A.; Ward, J. R. *Chem. Rev.* **1992**, *92*, 1729–1743.
- (2) Talmage, S. S.; Watson, A. P.; Hauschild, V.; Munro, N. B.; King, J. *Curr. Org. Chem.* **2007**, *11*, 285–298.
- (3) Munro, N. B.; Talmage, S. S.; Griffin, G. D.; Waters, L. C.; Watson, A. P.; King, J. F.; Hauschild, V. *Environ. Health Perspect.* **1999**, *107*, 933–974.
- (4) Tucker, J. *War of Nerves: Chemical Warfare from World War I to al-Qaeda*; First Edition.; Pantheon, 2006.
- (5) Kim, K.; Tsay, O. G.; Atwood, D. A.; Churchill, D. G. *Chem Rev* **2011**, *111*, 5345–5403.
- (6) *NATO Handbook on the Medical Aspects of NBC Defensive Operations AMedP-6(B)*; Department of the Army, the Navy, and the Air Force: Washington, DC, 1996.
- (7) Szinicz, L. *Toxicology* **2005**, *214*, 167–181.
- (8) Lundin, J. Development and Analysis of Self-Decontaminating Coatings. M.S. Thesis, George Mason University, 2011.
- (9) Defense, U. S. A. M. R. I. of M. *USAMRICD's Medical Management of Chemical Casualties Handbook*; 3rd ed.; International Medical Publishing, Inc., 2002.
- (10) Watson, A. P.; Griffin, G. D. *Environ. Health Perspect.* **1992**, *98*, 259–280.
- (11) Wormser, U. *Trends Pharmacol. Sci.* **1991**, *12*, 164–167.
- (12) Bismuth, C.; Borron, S. W.; Baud, F. J.; Barriot, P. *Toxicol. Lett.* **2004**, *149*, 11–18.
- (13) OPCW. *On the Implementation of the Convention on the Prohibition of the Development, Production, Stockpiling and Use of Chemical Weapons and on their Destruction in 2008*; Report of the OPCW; Organisation for the Prohibition of Chemical Weapons, 2009; p. 65.

- (14) Korkmaz, A.; Yaren, H.; Topal, T.; Oter, S. *Arch. Toxicol.* **2006**, *80*, 662–670.
- (15) Hosseini-khalili, A.; Haines, D. D.; Modirian, E.; Soroush, M.; Khateri, S.; Joshi, R.; Zendehtdel, K.; Ghanei, M.; Giardina, C. *Mutat. Res. Toxicol. Environ. Mutagen.* **2009**, *678*, 1–6.
- (16) Yamakido, M.; Ishioka, S.; Hiyama, K.; Maeda, A. *Environ. Health Perspect.* **1996**, *104*, 485–488.
- (17) Adachi, S.; Takemoto, K. *Jpn. J. Ind. Health* **1987**, *29*, 345–357.
- (18) USAMRICD. *Medical Management of Chemical Casualties Handbook*; Fourth Edition.; 2007.
- (19) Davis, K. G.; Aspera, G. *Ann. Emerg. Med.* **2001**, *37*, 653–656.
- (20) Russell, D.; Blaine, P. G.; Rice, P. *Emerg. Med. J.* **2006**, *23*, 421–424.
- (21) Mileson, B. E.; Chambers, J. E.; Chen, W. L.; Dettbarn, W.; Ehrich, M.; Eldefrawi, A. T.; Gaylor, D. W.; Hamernik, K.; Hodgson, E.; Karczmar, A. G.; Padilla, S.; Pope, C. N.; Richardson, R. J.; Saunders, D. R.; Sheets, L. P.; Sultatos, L. G.; Wallace, K. B. *Toxicol. Sci.* **1998**, *41*, 8–20.
- (22) Jokanovic, M. *Toxicol. Lett.* **2009**, *188*, 1–10.
- (23) Munro, N. B.; Ambrose, K. R.; Watson, A. P. *Environ. Health Perspect.* **1994**, *102*, 18–38.
- (24) Pope, C.; Karanth, S.; Liu, J. *Environ. Toxicol. Pharmacol.* **2005**, *19*, 433–446.
- (25) Tucker, J. B. *War of Nerves: chemical warfare from World War I to Al-Qaeda*; 1st ed.; Pantheon Books: New York, 2006.
- (26) Fitch, J. P.; Raber, E.; Imbro, D. R. *Science* **2003**, *302*, 1350–1354.
- (27) Romano, J. A.; Lukey, B. J.; Salem, H. *Chemical Warfare Agents: Chemistry, Pharmacology, Toxicology, and Therapeutics*; 2nd ed.; CRC Press, 2008.
- (28) Fielding, G. *Field Decontamination Studies With Chemical Warfare Decontaminating Solution DS2*; Naval Research Laboratory: Washington, DC, 1964; p. 29.
- (29) Modec, I. <http://deconsolutions.com/mdf200.html>.
- (30) Reynolds, C. M.; Ringelberg, D. B.; Perry, L. B.; Wagner, G. W. *Cold Reg. Sci. Technol.* **2008**, *52*, 244–253.

- (31) Wagner, G. W.; Procell, L. R.; Yang, Y. C.; Bunton, C. A. *Langmuir* **2001**, *17*, 4809–4811.
- (32) Wagner, G. W.; Yang, Y.-C. *Ind. Eng. Chem. Res.* **2002**, *41*, 1925–1928.
- (33) Wagner, G. W.; Procell, L. R.; Sorrick, D. C.; Lawson, G. E.; Wells, C. M.; Reynolds, C. M.; Ringelberg, D. B.; Foley, K. L.; Lumetta, G. J.; Blanchard, D. L. *Ind. Eng. Chem. Res.* **2010**, *49*, 3099–3105.
- (34) Wagner, G. W. . P., L.R.; Sorrick, D.C.; Hess, Z.A.; Gehring, D.G.; Henderson, V.D.; Brickhouse, M.D.; Rastogi, V.K; Turetsky, A.L.; Pfarr, J.W.; Dean-Wilson, A.M.; Kuhstoss, S.M.; Schilling, A.S. *Development of New Decon Green: A How-To Guide for the Rapid Decontamination of CARC Paint*; U.S. Army Research, Development and Engineering Command: Edgewood Chemical Biological Center, 2008; p. 51.
- (35) Wagner, G. W. . P., L.R.; Sorrick, D.C.; Hess, Z.A.; Gehring, D.G.; Henderson, V.D.; Brickhouse, M.D. *Decon Green*; Edgewood Chemical Biological Center: Aberdeen Proving Ground MD, 2004; p. 4.
- (36) Reynolds, C. M. . R., D.B; Perry, L.B. *Efficacy of DECON Green against VX Nerve and HD Mustard Simulants at Subfreezing Temperatures*; Engineering Research and Development Center: Hanover NH Cold Regions Research and Engineering Lab, 2006; p. 25.
- (37) Wagner, G. W. . B., P.W.; Procell, L.R.; Sorrick, D.C.; Henderson, V.D.; Turetsky, A.L.; Rastogi, V.K.; Yang, Y.C. *DECON GREEN Development and Chemical Biological Agent Efficacy Testing*; Edgewood Chemical Biological Center: Aberdeen Proving Ground MD, 2004; p. 20.
- (38) Lavoie, J.; Srinivasan, S.; Nagarajan, R. *J. Hazard. Mater.* **2011**, *194*, 85–91.
- (39) Król, P. *Prog. Mater. Sci.* **2007**, *52*, 915–1015.
- (40) Rodriguez, F.; Cohen, C.; Ober, C. K.; Archer, L. A. *Principles of Polymer Systems*; 5th ed.; CRC Press, 2003.
- (41) Winnik, M. A. *Curr. Opin. Colloid Interface Sci.* **1997**, *2*, 192–199.
- (42) Singh, H.; Jain, A. K. *J. Appl. Polym. Sci.* **2009**, *111*, 1115–1143.
- (43) Chattopadhyay, D. K.; Raju, K. V. S. N. *Prog. Polym. Sci.* **2007**, *32*, 352–418.
- (44) Campo, E. A. *Selection of Polymeric Materials: How to Select Design Properties from Different Standards*; 1st ed.; William Andrew, 2008.

- (45) Levine, F.; La Scala, J.; Kosik, W. *Prog. Org. Coat.* **2010**, *69*, 63–72.
- (46) Performance Specification Coating: Polyurethane, Aircraft and Support Equipment. MIL-PRF-85285E, 2012.
- (47) Shirtcliffe, N. J.; McHale, G.; I. Newton, M. *J. Polym. Sci. Part B Polym. Phys.* **2011**, *49*, 1203–1217.
- (48) Fulmer, P. A.; Wynne, J. H. *ACS Appl Mater Interfaces* **2011**, *3*, 2878–2884.
- (49) Harney, M. B.; Pant, R. R.; Fulmer, P. A.; Wynne, J. H. *ACS Appl Mater Interfaces* **2009**, *1*, 39–41.
- (50) Fulmer, P. A.; Lundin, J. G.; Wynne, J. H. *ACS Appl. Mater. Interfaces* **2010**, *2*, 1266–1270.
- (51) Kurt, P.; Wood, L.; Ohman, D. E.; Wynne, K. J. *Langmuir* **2007**, *23*, 4719–4723.
- (52) Cho, S. H.; White, S. R.; Braun, P. V. *Chem. Mater.* **2012**.
- (53) Muñoz-Bonilla, A.; Fernández-García, M. *Prog. Polym. Sci.* **2012**, *37*, 281–339.
- (54) Wagner, G. W.; Peterson, G. W.; Mahle, J. J. *Ind. Eng. Chem. Res.* **2012**, *51*, 3598–3603.
- (55) Cushen, M.; Kerry, J.; Morris, M.; Cruz-Romero, M.; Cummins, E. *Trends Food Sci. Technol.* **2012**, *24*, 30–46.
- (56) Kugel, A.; Stafslie, S.; Chisholm, B. J. *Prog. Org. Coat.* **2011**, *72*, 222–252.
- (57) Huh, M. W.; Kang, I.-K.; Lee, D. H.; Kim, W. S.; Lee, D. H.; Park, L. S.; Min, K. E.; Seo, K. H. *J. Appl. Polym. Sci.* **2001**, *81*, 2769–2778.
- (58) Oosterhof, J. J. H.; Buijssen, K. J. D. A.; Busscher, H. J.; Laan, B. F. A. M. van der; Mei, H. C. van der. *Appl. Environ. Microbiol.* **2006**, *72*, 3673–3677.
- (59) Hu, S.-G.; Jou, C.-H.; Yang, M.-C. *J. Appl. Polym. Sci.* **2002**, *86*, 2977–2983.
- (60) Shearer, A. E. H.; Paik, J. S.; Hoover, D. G.; Haynie, S. L.; Kelley, M. J. *Biotechnol. Bioeng.* **2000**, *67*, 141–146.
- (61) Yang, S.-H.; Lee, Y.-S. J.; Lin, F.-H.; Yang, J.-M.; Chen, K. *J. Biomed. Mater. Res. B Appl. Biomater.* **2007**, *83B*, 304–313.
- (62) Lin, J.; Murthy, S. K.; Olsen, B. D.; Gleason, K. K.; Klibanov, A. M. *Biotechnol. Lett.* **2003**, *25*, 1661–1665.



- (63) Barthlott, W.; Neinhuis, C. *Planta* **1997**, *202*, 1–8.
- (64) Xue, Z.; Liu, M.; Jiang, L. *J. Polym. Sci. Part B Polym. Phys.* **2012**, *50*, 1209–1224.
- (65) Borkar, I. V.; Dinu, C. Z.; Zhu, G.; Kane, R. S.; Dordick, J. S. *Biotechnol. Prog.* **2010**, *26*, 1622–1628.
- (66) McDaniel, C. S.; McDaniel, J.; Wales, M. E.; Wild, J. R. *Prog. Org. Coat.* **2006**, *55*, 182–188.
- (67) Suthiwangcharoen, N.; Nagarajan, R. *Biomacromolecules* **2014**, *15*, 1142–1152.
- (68) Pant, R. R.; Rasley, B. T.; Buckley, J. P.; Lloyd, C. T.; Cozzens, R. F.; Santangelo, P. G.; Wynne, J. H. *J. Appl. Polym. Sci.* **2007**, *104*, 2954–2964.
- (69) Pant, R. R.; Fulmer, P. A.; Harney, M. B.; Buckley, J. P.; Wynne, J. H. *J. Appl. Polym. Sci.* **2009**, *113*, 2397–2403.
- (70) Pant, R. R.; Buckley, J. L.; Fulmer, P. A.; Wynne, J. H.; McCluskey, D. M.; Phillips, J. P. *J. Appl. Polym. Sci.* **2008**, *110*, 3080–3086.
- (71) Wynne, J. H.; Pant, R. R.; Jones-Meehan, J. M.; Phillips, J. P. *J. Appl. Polym. Sci.* **2008**, *107*, 2089–2094.
- (72) Wynne, J. H.; Fulmer, P. A.; McCluskey, D. M.; Mackey, N. M.; Buchanan, J. P. *ACS Appl Mater Interfaces* **2011**, *3*, 2005–2011.
- (73) McCluskey, D. M.; Smith, T. N.; Madasu, P. K.; Coumbe, C. E.; Mackey, M. A.; Fulmer, P. A.; Wynne, J. H.; Stevenson, S.; Phillips, J. P. *ACS Appl. Mater. Interfaces* **2009**, *1*, 882–887.
- (74) Gephart, R. T.; Coneski, P. N.; Wynne, J. H. *Acs Appl. Mater. Interfaces* **2013**, *5*, 10191–10200.
- (75) Changtong, C.; Carney, D. W.; Luo, L.; Zoto, C. A.; Lombardi, J. L.; Connors, R. E. *J. Photochem. Photobiol. Chem.* **2013**, *260*, 9–13.
- (76) Salter, B.; Owens, J.; Hayn, R.; McDonald, R.; Shannon, E. *J. Mater. Sci.* **2009**, *44*, 2069–2078.
- (77) Blaser, H.-U.; Malan, C.; Pugin, B.; Spindler, F.; Steiner, H.; Studer, M. *Adv. Synth. Catal.* **2003**, *345*, 103–151.
- (78) Arbogast, J. W.; Darmany, A. P.; Foote, C. S.; Diederich, F. N.; Whetten, R. L.; Rubin, Y.; Alvarez, M. M.; Anz, S. J. *J. Phys. Chem.* **1991**, *95*, 11–12.

- (79) Nagano, T.; Arakane, K.; Ryu, A.; Masunaga, T.; Shinmoto, K.; Mashiko, S.; Hirobe, M. *Chem. Pharm. Bull. (Tokyo)* **1994**, *42*, 2291–2294.
- (80) Pichler, K.; Graham, S.; Gelsen, O. M.; Friend, R. H.; Romanow, W. J.; McCauley, J. P.; Coustel, N.; Fischer, J. E.; Smith, A. B. *J. Phys. Condens. Matter* **1991**, *3*, 9259–9270.
- (81) Wasielewski, M. R.; O’Neil, M. P.; Lykke, K. R.; Pellin, M. J.; Gruen, D. M. *J. Am. Chem. Soc.* **1991**, *113*, 2774–2776.
- (82) Dimitrijevic, N. M.; Kamat, P. V. *J. Phys. Chem.* **1992**, *96*, 4811–4814.
- (83) Bagrov, I. V.; Belousova, I. M.; Danilov, O. B.; Ermakov, A. V.; Grenishin, A. S.; Kiselev, V. M.; Kislyakov, I. M.; Murav’eva, T. D.; Sosnov, E. N.; Videnichev, D. A. *Fuller. Nanotub. Carbon Nanostructures* **2008**, *16*, 675–681.
- (84) Orfanopoulos, M.; Kambourakis, S. *Tetrahedron Lett.* **1995**, *36*, 435–438.
- (85) Yamakoshi, Y.; Umezawa, N.; Ryu, A.; Arakane, K.; Miyata, N.; Goda, Y.; Masumizu, T.; Nagano, T. *J. Am. Chem. Soc.* **2003**, *125*, 12803–12809.
- (86) Hotze, E. M.; Labille, J.; Alvarez, P.; Wiesner, M. R. *Environ. Sci. Technol.* **2008**, *42*, 4175–4180.
- (87) Haufler, R. E.; Wang, L.-S.; Chibante, L. P. F.; Jin, C.; Conceicao, J.; Chai, Y.; Smalley, R. E. *Chem. Phys. Lett.* **1991**, *179*, 449–454.
- (88) Fraelich, M. R.; Weisman, R. B. *J. Phys. Chem.* **1993**, *97*, 11145–11147.
- (89) Lee, J.; Fortner, J. D.; Hughes, J. B.; Kim, J.-H. *Environ. Sci. Technol.* **2007**, *41*, 2529–2535.
- (90) Lee, J.; Mackeyev, Y.; Cho, M.; Li, D.; Kim, J.-H.; Wilson, L. J.; Alvarez, P. J. J. *Environ. Sci. Technol.* **2009**, *43*, 6604–6610.
- (91) Deguchi, S.; Alargova, R. G.; Tsujii, K. *Langmuir* **2001**, *17*, 6013–6017.
- (92) Lyon, D. Y.; Adams, L. K.; Falkner, J. C.; Alvarez, P. J. J. *Environ. Sci. Technol.* **2006**, *40*, 4360–4366.
- (93) Long, D.-L.; Burkholder, E.; Cronin, L. *Chem Soc Rev* **2006**, *36*, 105–121.
- (94) Dawson, B. *Acta Crystallogr.* **1953**, *6*, 113–126.
- (95) Dolbecq, A.; Dumas, E.; Mayer, C. R.; Mialane, P. *Chem Rev* **2010**, *110*, 6009–6048.

- (96) Katsoulis, D. E. *Chem. Rev.* **1998**, *98*, 359–388.
- (97) Guo, Y.; Wang, Y.; Hu, C.; Wang, Y.; Wang, E.; Zhou, Y.; Feng, S. *Chem Mater* **2000**, *12*, 3501–3508.
- (98) Vazylyev, M.; Sloboda-Rozner, D.; Haimov, A.; Maayan, G.; Neumann, R. *Top. Catal.* **2005**, *34*, 93–99.
- (99) Hiskia, A.; Troupis, A.; Antonaraki, S.; Gkika, E.; Papaconstantinou, P. K. *Int. J. Environ. Anal. Chem.* **2006**, *86*, 233–242.
- (100) Lyon, D. K.; Miller, W. K.; Novet, T.; Domaille, P. J.; Evitt, E.; Johnson, D. C.; Finke, R. G. *J Am Chem Soc* **1991**, *113*, 7209–7221.
- (101) Pichon, C.; Dolbecq, A.; Mialane, P.; Marrot, J.; Riviere, E.; Goral, M.; Zynek, M.; McCormac, T.; Borshch, S. A.; Zueva, E.; Secheresse, F. *Chem.- Eur. J.* **2008**, *14*, 3189–3199.
- (102) Yin, P.; Li, D.; Liu, T. *Chem. Soc. Rev.* **2012**, *41*, 7368–7383.
- (103) Fulmer, P. A.; Wynne, J. H. *ACS Appl. Mater. Interfaces* **2012**, *4*, 738–743.
- (104) Reneker, D. H.; Yarin, A. L. *Polymer* **2008**, *49*, 2387–2425.
- (105) Chen, L.; Bromberg, L.; Lee, J. A.; Zhang, H.; Schreuder-Gibson, H.; Gibson, P.; Walker, J.; Hammond, P. T.; Hatton, T. A.; Rutledge, G. C. *Chem. Mater.* **2010**, *22*, 1429–1436.
- (106) Yoon, K.; Hsiao, B. S.; Chu, B. *J. Mater. Chem.* **2008**, *18*, 5326–5334.
- (107) Lundin, J.; Coneski, P.; Fulmer, P. A.; Wynne, J. H. *Prep.* **2013**.
- (108) Liu, S.; Tang, Z. *Nano Today* **2010**, *5*, 267–281.
- (109) Song, Y.-F.; Tsunashima, R. *Chem. Soc. Rev.* **2012**, *41*, 7384–7402.
- (110) Johnson, R. P.; Hill, C. L. *J. Appl. Toxicol.* **1999**, *19*, S71–S75.
- (111) Choi, J. H.; Kim, J. K.; Park, S.; Song, J. H.; Song, I. K. *Appl. Catal. Gen.* **2012**, *427–428*, 79–84.
- (112) Li, D.; Yin, P.; Liu, T. *Dalton Trans.* **2012**, *41*, 2853–2861.
- (113) Qi, W.; Wang, Y.; Li, W.; Wu, L. *Chem. – Eur. J.* **2010**, *16*, 1068–1078.

- (114) Ma, H.; Peng, J.; Han, Z.; Yu, X.; Dong, B. *J. Solid State Chem.* **2005**, *178*, 3735–3739.
- (115) Zheng, H.; Sun, Z.; Chen, X.; Zhao, Q.; Wang, X.; Jiang, Z. *Appl. Catal. Gen.* **2013**, *467*, 26–32.
- (116) Lundin, J. G.; Giles, S. L.; Cozzens, R. F.; Wynne, J. H. *Coatings* **2014**, *4*, 614–629.
- (117) Lundin, J. G.; Coneski, P. N.; Fulmer, P. A.; Wynne, J. H. *React. Funct. Polym.* **2014**, *77*, 39–46.
- (118) Nyman, M.; Ingersoll, D.; Singh, S.; Bonhomme, F.; Alam, T. M.; Brinker, C. J.; Rodriguez, M. A. *Chem. Mater.* **2005**, *17*, 2885–2895.
- (119) Zheng, S.-T.; Yang, G.-Y. *Chem. Soc. Rev.* **2012**, *41*, 7623.
- (120) Iwahara, J.; Schwieters, C. D.; Clore, G. M. *J. Am. Chem. Soc.* **2004**, *126*, 5879–5896.
- (121) North, C. L.; Franklin, J. C.; Bryant, R. G.; Cafiso, D. S. *Biophys. J.* **1994**, *67*, 1861–1866.
- (122) Garbuio, L.; Li, Y.; Antonello, S.; Gascón, J. A.; Lawler, R. G.; Lei, X.; Murata, Y.; Turro, N. J.; Maran, F. *Photochem. Photobiol.* **2014**, *90*, 439–447.
- (123) Solomon, I.; Bloembergen, N. *J. Chem. Phys.* **1956**, *25*, 261–266.
- (124) Battiste, J. L.; Wagner, G. *Biochemistry (Mosc.)* **2000**, *39*, 5355–5365.
- (125) Li, W.; Yi, S.; Wu, Y.; Wu, L. *J. Phys. Chem. B* **2006**, *110*, 16961–16966.
- (126) Jiang, Y.; Liu, S.; Zhang, J.; Wu, L. *Dalton Trans.* **2013**, *42*, 7643–7650.
- (127) Li, B.; Zhang, J.; Wang, S.; Li, W.; Wu, L. *Eur. J. Inorg. Chem.* **2013**, *2013*, 1869–1875.
- (128) Mbomekalle, I.-M.; Lu, Y. W.; Keita, B.; Nadjo, L. *Inorg. Chem. Commun.* **2004**, *7*, 86–90.
- (129) Ragesh, P.; Ganesh, V. A.; Nair, S. V.; Nair, A. S. *J. Mater. Chem. A* **2014**, *2*, 14773–14797.
- (130) Craig L., H. *J. Mol. Catal. Chem.* **2007**, *262*, 2–6.
- (131) Kozhevnikov, I. V. *Chem. Rev.* **1998**, *98*, 171–198.

- (132) Mansuy, D.; Bartoli, J. F.; Battioni, P.; Lyon, D. K.; Finke, R. G. *J. Am. Chem. Soc.* **1991**, *113*, 7222–7226.
- (133) Weiss, K. D. *Prog. Polym. Sci.* **1997**, *22*, 203–245.
- (134) Proust, A.; Matt, B.; Villanneau, R.; Guillemot, G.; Gouzerh, P.; Izzet, G. *Chem. Soc. Rev.* **2012**.
- (135) Lin, Y.; Böker, A.; He, J.; Sill, K.; Xiang, H.; Abetz, C.; Li, X.; Wang, J.; Emrick, T.; Long, S.; Wang, Q.; Balazs, A.; Russell, T. P. *Nature* **2005**, *434*, 55–59.
- (136) Kumar, S. K.; Jouault, N.; Benicewicz, B.; Neely, T. *Macromolecules* **2013**, *46*, 3199–3214.
- (137) Ganesan, V.; Jayaraman, A. *Soft Matter* **2013**, *10*, 13–38.
- (138) Mackay, M. E.; Tuteja, A.; Duxbury, P. M.; Hawker, C. J.; Horn, B. V.; Guan, Z.; Chen, G.; Krishnan, R. S. *Science* **2006**, *311*, 1740–1743.
- (139) Orlicki, J. A.; Kosik, W. E.; Demaree, J. D.; Bratcher, M. S.; Jensen, R. E.; McKnight, S. H. *Polymer* **2007**, *48*, 2818–2826.
- (140) Xiao, Y.; Han, Y.-K.; Xia, N.; Hu, M.-B.; Zheng, P.; Wang, W. *Chem. Weinh. Bergstr. Ger.* **2012**, *18*, 11325–11333.
- (141) Hoorfar, M.; W. Neumann, A. *Adv. Colloid Interface Sci.* **2006**, *121*, 25–49.
- (142) Young, T. *Philos. Trans. R. Soc. Lond.* **1805**, *95*, 65–87.
- (143) Zisman, W.A. In *Advances in Chemistry*; American Chemical Society, 1964; Vol. 43, pp. 1–51.
- (144) Owens DK; Wendt RC. *J. Appl. Polym. Sci.* **1969**, *13*, 1741–1747.
- (145) Van Oss, C. J.; Chaudhury, M. K.; Good, R. J. *Chem. Rev.* **1988**, *88*, 927–941.
- (146) Selvakumar, N.; Barshilia, H. C.; Rajam, K. S. *J. Appl. Phys.* **2010**, *108*, 013505.
- (147) Kügler, R.; Bouloussa, O.; Rondelez, F. *Microbiology* **2005**, *151*, 1341–1348.
- (148) Hooper, J. B.; Schweizer, K. S. *Macromolecules* **2006**, *39*, 5133–5142.
- (149) Bartelt-Hunt, S. L.; Knappe, D. R. U.; Barlaz, M. A. *Crit. Rev. Environ. Sci. Technol.* **2008**, *38*, 112–136.

- (150) Lee, J.; Yamakoshi, Y.; Hughes, J. B.; Kim, J.-H. *Environ. Sci. Technol.* **2008**, *42*, 3459–3464.
- (151) Michael Wilson, Ds., FRCPath. *Infect. Control Hosp. Epidemiol.* **2003**, *24*, 782–784.
- (152) Page, K.; Wilson, M.; Parkin, I. P. *J. Mater. Chem.* **2009**, *19*, 3819–3831.
- (153) Perni, S.; Piccirillo, C.; Pratten, J.; Prokopovich, P.; Chrzanowski, W.; Parkin, I. P.; Wilson, M. *Biomaterials* **2009**, *30*, 89–93.
- (154) Belousova, I. M.; Danilov, O. B.; Murav'eva, T. D.; Kiselyakov, I. M.; Ryl'kov, V. V.; Kris'ko, T. K.; Kiselev, O. I.; Zarubaev, V. V.; Sirotkin, A. K.; Piotrovskii, L. B. *J. Opt. Technol.* **2009**, *76*, 243–250.
- (155) Vandewal, K.; Albrecht, S.; Hoke, E. T.; Graham, K. R.; Widmer, J.; Douglas, J. D.; Schubert, M.; Mateker, W. R.; Bloking, J. T.; Burkhard, G. F.; Sellinger, A.; Fréchet, J. M. J.; Amassian, A.; Riede, M. K.; McGehee, M. D.; Neher, D.; Salleo, A. *Nat. Mater.* **2014**, *13*, 63–68.
- (156) Badamshina, E.; Estrin, Y.; Gafurova, M. *J. Mater. Chem. A* **2013**, *1*, 6509–6529.
- (157) Giacalone, F.; Martín, N. *Chem. Rev.* **2006**, *106*, 5136–5190.
- (158) Accorsi, G.; Armaroli, N. *J. Phys. Chem. C* **2010**, *114*, 1385–1403.
- (159) Badamshina, E.; Gafurova, M. *J. Mater. Chem.* **2012**, *22*, 9427–9438.
- (160) Teh, S.-L.; Linton, D.; Sumpter, B.; Dadmun, M. D. *Macromolecules* **2011**, *44*, 7737–7745.
- (161) Heiney, P.; Fischer, J.; Mcghie, A.; Romanow, W.; Denenstein, A.; Mccauley, J.; Smith, A.; Cox, D. *Phys. Rev. Lett.* **1991**, *66*, 2911–2914.
- (162) Sachidanandam, R.; Harris, A. *Phys. Rev. Lett.* **1991**, *67*, 1467–1467.
- (163) Bellanger, H.; Darmanin, T.; Taffin de Givenchy, E.; Guittard, F. *Chem. Rev.* **2014**.
- (164) Zhang, J. Z.; Geselbracht, M. J.; Ellis, A. B. *J. Am. Chem. Soc.* **1993**, *115*, 7789–7793.
- (165) Phillips, J. P.; Deng, X.; Todd, M. L.; Heaps, D. T.; Stevenson, S.; Zhou, H.; Hoyle, C. E. *J. Appl. Polym. Sci.* **2008**, *109*, 2895–2904.

- (166) Bagrov, I.; Belousova, I.; Danilov, O.; Kiselev, V.; Murav'eva, T.; Sosnov, E. *Opt. Spectrosc.* **2007**, *102*, 52–59.
- (167) Hawker, C. J.; Saville, P. M.; White, J. W. *J. Org. Chem.* **1994**, *59*, 3503–3505.
- (168) Anslow, W. P.; Karnofsky, D. A.; Jager, B. V.; Smith, H. W. *J. Pharmacol. Exp. Ther.* **1948**, *93*, 1–9.
- (169) Yang, Y. C.; Szafraniec, L. L.; Beaudry, W. T.; Ward, J. R. *J. Org. Chem.* **1988**, *53*, 3293–3297.
- (170) Wagner, G. W.; Bartram, P. W. *J. Mol. Catal. Chem.* **1996**, *111*, 175–180.
- (171) Wagner, G. W.; Bartram, P. W. *Langmuir* **1999**, *15*, 8113–8118.
- (172) Jaeger, D. A.; Roberts, T. L.; Zelenin, A. K. *Colloids Surf. Physicochem. Eng. Asp.* **2002**, *196*, 209–216.
- (173) Yang, Y. C.; Szafraniec, L. L.; Beaudry, W. T.; Davis, F. A. *J. Org. Chem.* **1990**, *55*, 3664–3666.
- (174) Wagner, G. W.; Koper, O. B.; Lucas, E.; Decker, S.; Klabunde, K. J. *J. Phys. Chem. B* **2000**, *104*, 5118–5123.
- (175) Boring, E.; Geletii, Y. V.; Hill, C. L. *J. Am. Chem. Soc.* **2001**, *123*, 1625–1635.
- (176) Martyanov, I. N.; Klabunde, K. J. *Environ. Sci. Technol.* **2003**, *37*, 3448–3453.
- (177) Wu, K. H.; Yu, P. Y.; Yang, C. C.; Wang, G. P.; Chao, C. M. *Polym. Degrad. Stab.* **2009**, *94*, 1411–1418.
- (178) Kleinhammes, A.; Wagner, G. W.; Kulkarni, H.; Jia, Y.; Zhang, Q.; Qin, L.-C.; Wu, Y. *Chem. Phys. Lett.* **2005**, *411*, 81–85.
- (179) Ziegler, W.; Engelhardt, G.; Wallnoefer, P. R.; Oehlmann, L.; Wagner, K. *J. Agric. Food Chem.* **1980**, *28*, 1102–1106.
- (180) *Boll Weevil Eradication Program Fact Sheet*; Animal and Plant Health Inspection Service, 2007.
- (181) Obendorf, S. K. *Aatcc Rev.* **2010**, *10*, 44–50.
- (182) Hasan, J.; Crawford, R. J.; Lvanova, E. P. *Trends Biotechnol.* **2013**, *31*, 31–40.
- (183) Greiner, A.; Wendorff, J. H. *Angew. Chem. Int. Ed.* **2007**, *46*, 5670–5703.

- (184) Deitzel, J. .; Kleinmeyer, J.; Harris, D.; Beck Tan, N. . *Polymer* **2001**, *42*, 261–272.
- (185) Theron, S. A.; Zussman, E.; Yarin, A. L. *Polymer* **2004**, *45*, 2017–2030.
- (186) Lin, K.; Chua, K.-N.; Christopherson, G. T.; Lim, S.; Mao, H.-Q. *Polymer* **2007**, *48*, 6384–6394.
- (187) Arumugam, G. K.; Khan, S.; Heiden, P. A. *Macromol. Mater. Eng.* **2009**, *294*, 45–53.
- (188) Seo, J. M.; Arumugam, G. K.; Khan, S.; Heiden, P. A. *Macromol. Mater. Eng.* **2009**, *294*, 35–44.
- (189) Coneski, P. N.; Nash, J. A.; Schoenfisch, M. H. *ACS Appl. Mater. Interfaces* **2011**, *3*, 426–432.
- (190) Chen, L.; Bromberg, L.; Hatton, T. A.; Rutledge, G. C. *Polymer* **2008**, *49*, 1266–1275.
- (191) Ojha, S. S.; Afshari, M.; Kotek, R.; Gorga, R. E. *J. Appl. Polym. Sci.* **2008**, *108*, 308–319.
- (192) Kim, S. J.; Nam, Y. S.; Rhee, D. M.; Park, H.-S.; Park, W. H. *Eur. Polym. J.* **2007**, *43*, 3146–3152.
- (193) Shawon, J.; Sung, C. *J. Mater. Sci.* **2004**, *39*, 4605–4613.
- (194) Tsou, S.-Y.; Lin, H.-S.; Wang, C. *Polymer* **2011**, *52*, 3127–3136.
- (195) Tan, K.; Obendorf, S. K. *J. Membr. Sci.* **2007**, *305*, 287–298.
- (196) Schiffman, J. D.; Elimelech, M. *ACS Appl. Mater. Interfaces* **2011**, *3*, 462–468.
- (197) Yao, C.; Li, X.; Neoh, K. G.; Shi, Z.; Kang, E. T. *J. Membr. Sci.* **2008**, *320*, 259–267.
- (198) Zhu, J.; Bahramian, Q.; Gibson, P.; Schreuder-Gibson, H.; Sun, G. *J. Mater. Chem.* **2012**, *22*, 8532–8540.
- (199) Qian, L.; Sun, G. *J. Appl. Polym. Sci.* **2003**, *89*, 2418–2425.
- (200) Coneski, P. N.; Fulmer, P. A.; Wynne, J. H. *Langmuir* **2012**, *28*, 7039–7048.
- (201) Coneski, P. N.; Fulmer, P. A.; Wynne, J. H. *RSC Adv.* **2012**, *2*, 12824.



- (202) Fridrikh, S. V.; Yu, J. H.; Brenner, M. P.; Rutledge, G. C. *Phys. Rev. Lett.* **2003**, *90*, 144502.
- (203) Thompson, C. J.; Chase, G. G.; Yarin, A. L.; Reneker, D. H. *Polymer* **2007**, *48*, 6913–6922.
- (204) Lin, T.; Wang, H.; Wang, H.; Wang, X. *Nanotechnology* **2004**, *15*, 1375.
- (205) Angammana, C. J.; Jayaram, S. H. *IEEE Trans. Ind. Appl.* **2011**, *47*, 1109–1117.
- (206) Koombhongse, S.; Liu, W.; Reneker, D. H. *J. Polym. Sci. Part B Polym. Phys.* **2001**, *39*, 2598–2606.
- (207) Saunders, P. R. *J. Polym. Sci. A* **1964**, *2*, 3755–3764.
- (208) Ryu, S.-Y.; Kwak, S.-Y. *J. Nanosci. Nanotechnol.* **2013**, *13*, 4193–4202.
- (209) Moghe, A. K.; Hufenus, R.; Hudson, S. M.; Gupta, B. S. *Polymer* **2009**, *50*, 3311–3318.
- (210) Mit-Uppatham, C.; Nithitanakul, M.; Supaphol, P. *Macromol. Chem. Phys.* **2004**, *205*, 2327–2338.
- (211) Reneker, D. H.; Yarin, A. L.; Fong, H.; Koombhongse, S. *J. Appl. Phys.* **2000**, *87*, 4531–4547.

## **BIOGRAPHY**

Jeffrey G. Lundin graduated from Unatego Central School, Otego, New York in 2003. He received his Bachelor of Science in Biochemistry and Molecular Biology from the University at Albany, State University of New York in 2007. He was employed at Quest Diagnostics in Chantilly, Virginia for one and half years, after which he enrolled in graduate studies at George Mason University in Fairfax, Virginia and concurrently began his research at the Naval Research Laboratory under the Pathways program in 2009. He earned his Master of Science in chemistry in 2011 for his thesis related to research performed at the NRL on self-decontaminating coatings.